Blast-wave-driven, multidimensional Rayleigh-Taylor instability experiments

by

Carolyn C. Kuranz

A dissertation submitted in partial fulfillment
of the requirements for the degree of
Doctor of Philosophy
(Applied Physics)
in The University of Michigan
2009

Doctoral Committee:

Professor R. Paul Drake, Chair
Professor Robert Krasny
Professor Yue Ying Lau
Professor Bradford Orr
Professor Gregory Tarle

To Roland L. Neumaier and John L. Kuranz

ACKNOWLEDGEMENTS

I would first like to thank my advisor, Paul Drake, for his continuing guidance in my career and life. I would like to acknowledge the support of my family especially my husband, Jonathan. Finally, I would like to thank Nels Hoffman for introducing me to this exciting field of study.

TABLE OF CONTENTS

LIST OF FIGURES

Figure

LIST OF TABLES

Table

LIST OF APPENDICES

Appendix

LIST OF ABBREVIATIONS

IUE International Ultraviolet Explorer

ICF Inertial Confinement Fusion

2D two-dimensional

3D three-dimensional

RT Rayleigh-Taylor

RM Richtmyer-Meshkov

HED high-energy-density

Re Reynolds number

Pe Peclet number

Z atomic number

CHBr brominated plastic

DPP Distributed Phase Plate

MCP microchannel plate

CRF Carbonized Resorsinol Formaldehyde

1D one-dimensional

EOS equation of state

PPM Piecewise Parabolic Method

DEF Direct Exposure Film

SPCA Static Pinhole Camera Array

FFT Fast Fourier Transform

IDL Interactive Data Language

TIM Ten Inch Manipulator

XRFC X-ray Framing Camera

LLE Laboratory for Laser Energetics

LLNL Lawrence Livermore National Laboratory

MPBL Magnetic Point Backlighter

BL backlighter

ABSTRACT

Blast-wave-driven, multidimensional Rayleigh-Taylor instability experiments

by

Carolyn C. Kuranz

Chair: R. Paul Drake

This thesis discusses experiments well-scaled to the blast-wave-driven instabilities that are believed to occur during the explosion phase of SN1987A. Blast waves occur following a sudden, finite release of energy, and consist of a shock front followed by a rarefaction wave. When a blast wave crosses an interface with a decrease in density, hydrodynamic instabilities will develop. These experiments include target materials scaled in density to the He-H layer in SN1987A. About 5 kJ of laser energy from the Omega Laser facility irradiates a 150 μm plastic disk that is followed by a low-density foam cylinder. A blast wave structure similar to those in supernovae is created in the plastic layer. Several types of initial conditions that seed the hydrodynamic instabilities are presented in this thesis. These include 2D, 3D, single-mode and multimode sinusoidal patterns. These conditions produce unstable growth dominated by the Rayleigh-Taylor instability in the nonlinear regime. We have detected the interface structure under these conditions, using dual, orthogonal radiography. The growth of the unstable layer is compared to incompressible mixing models. Recent advances in our x-ray backlighting techniques have greatly improved the resolution of our x-ray radiographic images. Under certain conditions, the improved images

show some mass extending beyond the Rayleigh-Taylor spike and penetrating further than previously observed or predicted by current simulations. 3D, hydrodynamic simulations do not show this effect. I will also discuss the amount of mass in these spike extensions, the associated uncertainties, and hypotheses regarding their origin.

CHAPTER I

Introduction

This thesis presents my contributions to work begun 12 years ago studying the hydrodynamics of supernovae [64, 30, 16, 29, 66, 19, 52, 17, 42]. The goal of these experiments is to study, in a controlled laboratory setting, the mixing that occurs at an unstable interface subjected to an acceleration history similar to that of the explosion phase of a core-collapse supernova, specifically SN1987A. My own contributions include leading several of these experiments, data analysis, comparing the data to models, performing simulations and publishing the results [37, 38, 42, 39, 41, 40]. In this chapter, the progenitor, or presupernova, star of SN1987A is described as well as the discovery and observations of the supernova. The formation of a blast wave and the potential development of the hydrodynamic instabilities in the star will be detailed. A brief description is given of how the conditions of supernova hydrodynamics experiments, and related experiments, are similar to astrophysical systems and how those conditions are achieved. This chapter concludes with a discussion of previous work that led to the present experiments and a brief description of the later chapters in this thesis.

1.1 SN1987A

1.1.1 The progenitor star

SN1987A was discovered by an astronomer at the Las Campanas Observatory on February 24.23 UT, 1987. After the discovery, the progenitor star of SN1987A was identified to be Sanduleak -69 202 in the outskirts of the Tarantula Nebula in the Large Magellanic Cloud. An image of SN1987A taken by the Hubble Space telescope is shown in Figure 1.1. SN1987A is visible near the center of the image and a magnified image of the supernova is inset in the upper right corner of Figure 1.1. The smaller image was taken in visible light with the Wide Field Planetary Camera in February 1994. The large image is a composite of several pictures taken with the same camera. These images were taken in September 1994, February 1996 and July 1997.

The progenitor star was a blue supergiant with a radius of $\sim 3 \times 10^{12}$ cm and was about 50 kpc or about 168,000 light-years from Earth. The star was of spectral type B3 and luminosity class I, with a luminosity of about 4.0×10^{38} ergs s^{-1}. The current luminosity is lower, about 1×10^{37} ergs s^{-1}, which indicates the star did explode. The surface temperature of the progenitor star was ∼16,000 K. The mass was estimated at 16 – 22 $M_{\odot}$. Observational astronomers were able to, for the first time, employ all modern observational astronomy techniques to observe this local supernova. These techniques include neutrino detection, and γ-ray, infrared, and ultraviolet spectroscopy. The presence of hydrogen lines in the observed spectra indicates that SN1987A was a Type II or core-collapse supernova [1, 11].

1.1.2 Core-collapse supernovae

A core-collapse supernova is the destruction of a massive star no longer able to support its own mass under the force of gravity. Massive stars, defined here as having

Figure 1.1: A composite image of SN1987A and the surrounding region taken by the Hubble Space Telescope and (inset) a magnified image of the supernova.

a mass greater than $8M_{\odot}$, are powered by the fusion of hydrogen to form helium. Eventually, these stars will deplete their hydrogen fuel producing an almost pure helium core within its inner 6 $M_{\odot}$. Hydrogen burning will continue in the thick shell surrounding the helium core. The star will undergo a core contraction, which raises the core temperature and density enough for He burning to begin. This process creates carbon, oxygen and neon. This process of element depletion, core contraction and shell ignition continues to synthesize many new elements up to Fe. Iron has the maximum nuclear binding energy per nucleon of 9 MeV nucleon^{-1}. Therefore, no net energy can be released by nuclear fusion. The mass of the Fe core increases as the surrounding layers burn elements up to Fe. This causes the star to have a layered density structure, shown in Figure 1.2, with the densest materials at the center of the star. When the iron core reaches about 1.4 $M_{\odot}$, gravity overcomes the electron degeneracy pressure supporting the core. The huge core collapses in seconds.

Once the collapse begins, it continues until the central density of the star has risen

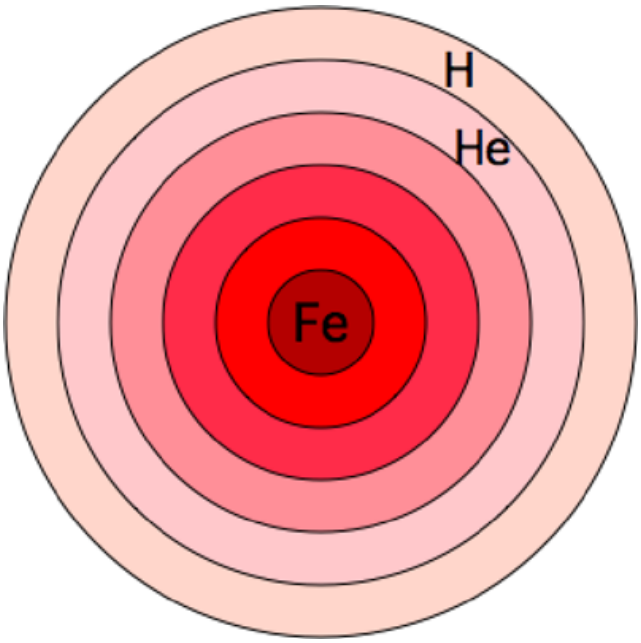

Figure 1.2: A drawing of a presupernova star showing the layered density structure with the newly synthesized heavy elements concentrated at the core. Moving outward from the core, elements decrease in density until the outermost, and least dense, hydrogen envelope is reached.

by a factor of 10^6. This is equivalent to something the size of Earth, which has a diameter of ∼12,800 km, collapsing to 50 km in 1 second. During the collapse, the material in the outer portion of the iron core reaches velocities of about 70,000 km s^{-1}. The outermost layers of the star, the neon, carbon and helium shells and the hydrogen envelope, do not participate in the collapse. This is because gravitational forces are weaker in the outer region of the star and because information about the collapse travels as sound waves moving at the speed of sound [73, 72].

The collapse is only stopped when the nuclear force, which is normally attractive, becomes repulsive. This occurs when the central density of the star increases to be several times that of the atomic nucleus. The change of sign in the nuclear force resists further collapse. The large nuclear pressure causes the inner part of the core to stop and spring back. The rebounding part of the core is about 0.7 $M_\odot$ or about half of the collapsing iron core. Outside of this area, matter is falling toward the

core supersonically. This material collides with the rebounding core and a shock wave forms. As the shock propagates outward from the core, it encounters infalling matter, which causes it to stall. The shock is then restarted, possibly by energy deposited by neutrinos emitted from the core, though the mechanism for the restart is still debated. Eventually, the shock continues moving outward with enough energy to drive through the outer layers of the star, thus, destroying the star.

The explosion that creates a shock wave in a supernova has a short lifetime compared with the amount of time it takes for the shock to traverse the layers of the supernova. This causes a rarefaction wave, a decrease in density and pressure due to outward flow, to overtake the shock and produce a blast wave. In a supernova, the blast wave encounters multiple interfaces where the density decreases more abruptly. This is due to the layered density structure discussed earlier and seen in Figure 1.2. The blast wave encounters a drop in density at the interface between the C-O layer and the He layer and again at the He-H interface. When the blast wave encounters one of these interfaces, the post-shock density ratio between the layers is greater than can be sustained by a single shock. A forward shock is launched into the subsequent layer and a reverse shock is also formed. This is further discussed in Chapter II.

1.1.3 Observation of SN1987A

Observations of SN1987A were performed by making brightness measurements at ultraviolet, optical and infrared wavelengths. Optical and infrared observations were made with ground-based telescopes by groups at Cerro Tololo Inter-American Observatory in Chile and South African Astronomical Observatory. The measurements in the ultraviolet were made with the International Ultraviolet Explorer (IUE) satellite. The resulting light curve is seen in Figure 1.3 which is adapted from Arnett (1989) [1]. This plot shows the luminosity in ergs s^{-1} versus time in days. There are minor discrepancies between the two curves due to different methods for integrating over

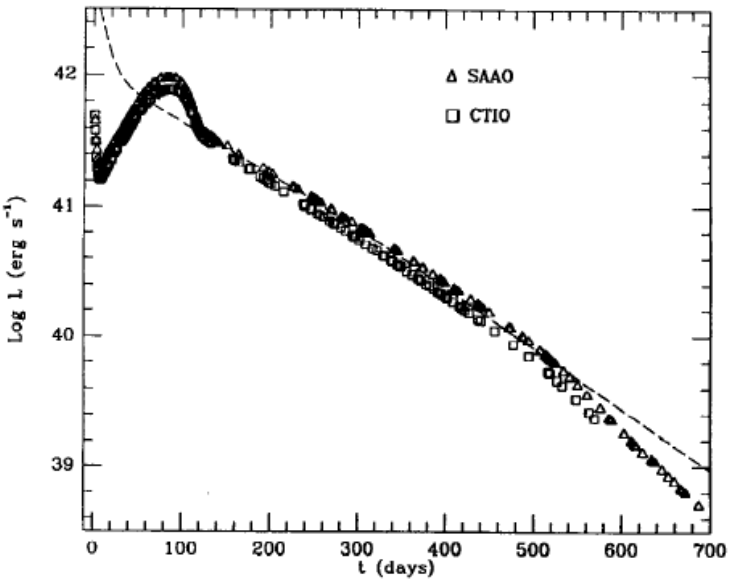

Figure 1.3: Light curve data from SN1987A collected from the Cerro Tololo Inter-American Observatory (CTIO) and the South African Astronomical Observatory (SAAO). The luminosity of SN1987A vs. days since outburst is shown. Image adapted from Arnett (1989) [1].

wavelengths and assumptions about interstellar extinction.

The outward results of the shock, which starts at the core of the star, breaking out of the hydrogen envelope is referred to as the UV Flash. This is because the temperature is so high, $2 - 5 \times 10^5$ K, that most of the radiation is in the ultraviolet. Since the IUE was only employed to collect data after the initial discovery of the supernova, the initial UV burst was not recorded. Instead, the earliest IUE observations show a decline in the UV flux, by a factor of about 1000, in the first three days after detection of the supernova. This is most likely due to the cooling that occurs in the days after shock breakout. Models of blue supergiant explosions showed good agreement with the early light curve data.

After day 40, it became apparent that another energy source was needed to fit the light curve data. After day 120, it was realized that the energy source was ^{56}Co. The observation of this radioactive isotope was much sooner than predicted by spherically symmetric models in which the heaviest elements are in the core. In

order to reproduce the light curve of SN1987A, shown Figure 1.3, models distributed some heavy elements, previously thought to be in the core, halfway to the surface of the star. This suggests that heavy elements that were created in the core of the star were mixed into the envelope of gas and not concentrated at the center of the star. It is possible that this was caused by large-scale hydrodynamic mixing. This has led to many simulations and experiments to study the effect of blast-wave-driven instabilities on the transport of heavy elements in SN1987A [11], including the work described in this thesis.

1.1.4 Blast-wave-driven instabilities

1.1.4.1 Blast waves

Blast waves often occur following a rapid, finite release of energy, and consist of a shock front followed by a rarefaction wave. Many explosions lead to the development of a blast wave. These explosions can occur in the air, underwater, underground, on Earth's surface or in the cosmos. Typical examples of a blast wave occurrence is after a nuclear explosion or a core-collapse supernova explosion. Another example of when a blast wave is formed, include the collision of a comet with a planet or planetary atmosphere [49]. Also, the interaction of the solar wind with the energy released from a solar flare creates blast waves in the solar wind [15].

A blast wave creates a pressure gradient in the direction of its propagation. If the structure of a system has a density gradient in an opposing direction to the pressure gradient then the Rayleigh-Taylor (RT) [60, 70] instability will occur. This will happen when a blast wave crosses an interface or transition where the density decreases. This is the case in a supernova explosion when a blast wave is created and moves outward across transitions of more-rapidly decreasing density. A schematic of this situation and the resulting gradients is shown in Figure 1.4. The interface between any two layers in the supernova is not infinitely smooth and fluctuations will

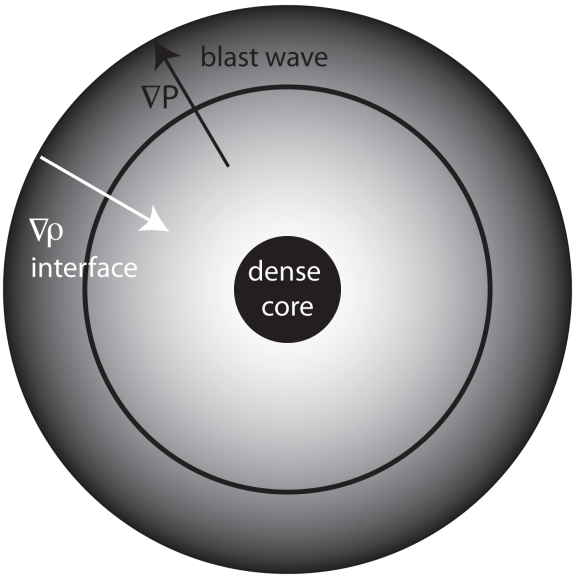

Figure 1.4: A schematic of a blast wave in a supernova. The blast wave crosses a density drop at an interface creating a density gradient in the direction opposite the pressure gradient. This situation induces the Rayleigh-Taylor instability.

seed instability growth.

1.1.4.2 Rayleigh-Taylor instability

The Rayleigh-Taylor instability is also a common process, occurring whenever denser fluid is accelerated against less dense fluid, whether in a gravitational field or otherwise. The Rayleigh-Taylor instability is believed to occur in core-collapse supernova explosions and in young supernova remnants as the stellar ejecta are decelerated by the shocked circumstellar medium [11]. Rayleigh-Taylor growth is also evident in the Crab Nebula, at the boundary of the pulsar-wind nebula, where hot gas from the supernova explosion is accelerated into the surrounding interstellar medium creating a finger-like structure [28]. The instability also has a profound effect in the climate, by driving ocean circulation [10], and in Inertial Confinement Fusion (ICF) experiments [48]. ICF experiments use low-density, laser heated plasma to accelerate a dense fuel layer. Such a system is inherently Rayleigh-Taylor unstable; target imperfections or

non-uniform laser irradiation seed the instability. This causes mixing of the different regions of the target, which in turn limits the fusion gain. Also, because of the mixing brought on by the Rayleigh-Taylor instability, the further understanding of this phenomenon may lead to a better understanding of turbulent mixing [77]. The experiments described in this thesis focus on the Rayleigh-Taylor instability at the blast-wave-driven He-H interface in a core-collapse supernova, with a specific focus on SN1987A.

In many cases, when the Rayleigh-Taylor instability is present, other instabilities, such as the Richtmyer-Meshkov (RM) instability [65, 50], also exist. This instability occurs when an interface with a density drop is impulsively accelerated. A shock wave can provide this type of acceleration. The Richtmyer-Meshkov instability occurs in the supernova after the blast wave moves outward through the star, crossing interfaces where the density decreases. This causes fluctuations on the interface to grow, much like the Rayleigh-Taylor instability. Once the shock passes, the acceleration decreases, causing the growth of the Richtmyer-Meshkov instability to also decrease. This instability is most likely not dominant in core-collapse supernova mixing because the impulsive acceleration by the shock crossing the interface is very short. However, RM certainly has great effect on the initial conditions for Rayleigh-Taylor growth. However, the Richtmyer-Meshkov instability is significant or perhaps dominant in Type I supernova due to large-amplitude initial conditions [51].

1.1.5 Simulations of SN1987A

Several simulations have been performed to model different aspects of SN1987A, specifically the unexpected observations of heavy elements, such as ^{56}Co and ^{56}Ni. As previously mentioned, to reproduce the light curve of the supernova, models had to distribute these heavy elements halfway to the surface of the star. This indicates that there may be some large-scale hydrodynamic mixing affecting the structure of

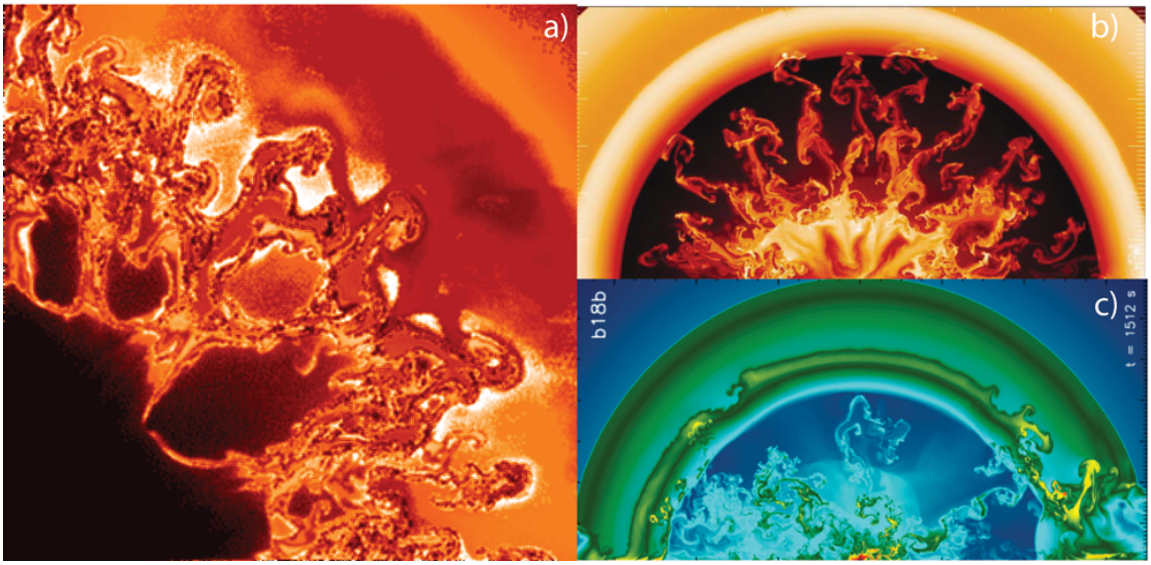

Figure 1.5: 2D simulations of SN1987A. a) Muller (1991) [54] showed low heavy element velocities while b) Kifonidis (2003) [33] showed high initial heavy element velocities that decreased by a factor of 2 when the material reached the reverse shock in the He shell. Only c) Kifonidis (2006) [34] shows good quantitative agreement with observations of SN1987A.

the star as it explodes. The simulations discussed here focus on the hydrodynamic instabilities during the explosion phase of the supernova.

The results from a two-dimensional (2D) Prometheus simulation performed by Muller (1991) [54, 22] is shown in Figure 1.5a. This density plot is shown at 3.6 hours after the core collapse. This simulation deposited 1.0×10^{51} ergs in a few of the inner zones of the star and the energy was equally divided between thermal and kinetic energy. It also included random perturbations on the interface between the C-O and He as well as between the He and H layers. Spikes of dense material move outward from the core, while bubbles of lower density material move inward, toward the core. The velocity of the dense material in the simulation was only about half the observed velocity of heavy elements observed in the actual supernova.

An additional 2D simulation is shown in Figure 1.5b. This simulation was performed by Kifonidis (2003) [33] and the image in Figure 1.5b is a density plot at 0.4

hr. This simulation studied the role of neutrino-driven convection in the explosion. Instead of adding a huge amount of energy to the center of the star to initiate the explosion, this simulation used neutrino heating behind the stalled supernova shock to restart and drive the shock through the star. Perturbations at the Si-O interface are seeded by flow structures resulting from neutrino-driven convection. In this simulation, the velocity of heavy elements, such as ^{56}Ni, was initially high enough to explain the observed values, but dropped by a factor of 2 when the material reached the reverse shock in the He shell.

A more recent 2D simulation, also performed by Kifonidis (2006) [34] and shown in Figure 1.5c, showed very high heavy element velocities. The authors found that if a low-mode hydrodynamic instability develops very near the time the shock is restarted, then the resulting explosion produces data in good agreement with the observations of SN1987A. In this case, the hydrodynamics are dominated by these low-order unstable modes. The unstable modes provide perturbations that seed the Rayleigh-Taylor instability at the Si-O and O-He interfaces of the progenitor star. These low-order modes also deform the shock, which then deposits vorticity and induces a strong Richtmyer-Meshkov instability at the He-H interface. These simulations showed much higher, 40% higher in some cases, heavy element velocities compared to the previous Kifonidis (2003) simulations. The simulation results also showed good quantitative agreement with the observational data from SN1987A.

A star is an extremely complex structure and a three-dimensional (3D) simulation with perturbations on all layers of the star and able to resolve all spatial scales down to the Komogorov scale on which turbulence dissipates would be needed to fully understand the role of hydrodynamic instabilities during the explosion of the supernova. At the current time, a simulation of this magnitude is not feasible. Therefore, it is worthwhile to access conditions similar to those found in supernova in a controlled laboratory setting. Intense laser facilities have been able to achieve these conditions

in the field of study referred to as high-energy-density (HED) physics.

1.2 High-Energy-Density Physics and Facilities

HED Physics is the study of systems with pressures over 1 million atmospheres or 1 Mbar. This paper will use units of bars for pressure, where 1 bar is equal to 100,000 Pascals. At such high pressure, materials also have extremely high temperatures, often at or above 10 keV or 100 million Kelvin. Materials subject to these conditions are ionized and do not behave like an ensemble of neutral particles. In some cases, these materials also have very high densities. In fact, the material may be too dense for traditional plasma theory to apply. These conditions can be created by intense lasers and are similar to conditions found in astrophysics.

Many laser facilities exist worldwide for the purpose of creating HED environments. These facilities range from the 10-beam Nova laser to its successor the 192 -beam National Ignition Facility. The experiments described in this thesis use the Omega Laser [7, 6], which is part of the Laboratory for Laser Energetics at the University of Rochester. A drawing of the Omega laser facility is shown in Figure 1.6. The facility is 100 meters in length and 10 meters tall. There are 60 neodynium:glass laser beams, operating at a wavelength of 351 nm. An initial beam is formed and amplified in the center of the laser bay. It is split and amplified further and eventually feeds into 60 amplifier chains that feed down the sides of the laser bay to the spherical target chamber. Together, all 60 laser beams can deliver 30 kJ of energy to an experimental target. HED facilities, such as the Omega laser, allow access to the conditions in astrophysics in a controlled setting.

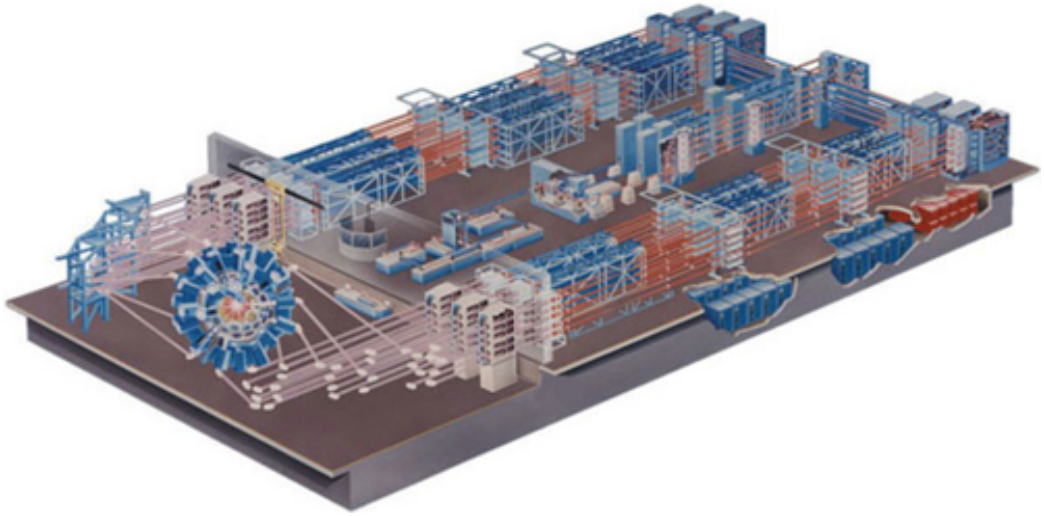

Figure 1.6: An airbrush of the Omega laser facility, which is 100 meters long and 10 meters high. The 60 laser beams are formed in the laser bay on the right and feed into the target chamber on the left.

1.3 Laboratory Astrophysics

Laboratory astrophysics experiments can bridge the gap between theoretical models and observations. These experiments use HED facilities to deposit kJs of energy into mm-scale volumes. This creates ionized, high-pressure systems and energy densities similar to those that occur in astrophysics. Access to these conditions allow for a wide range of laboratory astrophysics experiments [63]. The experiments in this thesis focus on the hydrodynamics of a supernova during the explosion phase, however, there are many other interesting areas of astrophysics that can be accessed using HED facilities.

Supernova remnants, such as Cassiopeia-A remnant, are particularly interesting due to the observable interaction of stellar ejecta with the surrounding circumstellar medium. It is likely that the stellar ejecta or circumstellar medium possess some amount of clumpiness. These clumps will introduce vorticity into the fluid that surrounds them and can affect the development of instabilities. Two experiments [36, 35, 25] have studied shock interaction with single clumps of material. One ex-

periment was performed on the Nova laser and the other on the Omega laser. Both experiments created a planar blast wave and then observed its interaction with a dense sphere of material.

Radiative effects in shock waves can also be studied in the laboratory. These effects are present in supernova remnants and many astrophysical shocks. Experiments have been executed that study driven radiative shocks [32, 61, 62] and experiments have been performed to study radiative blast waves and the effects of thin-shell instabilities [71, 24, 20, 59]. Experiments were carried out at the Janus laser facility [20] and at Z-Beamlet facility [59]. In both cases the laser is focused onto a nylon pin. The pin is in a chamber filled with Xe gas under pressures of between 5 and 10 Torr. This creates a spherical blast wave that is radiatively cooling. Under these conditions, the effects of thin shell instabilities can be studied.

Astrophysical jets are quite common in the universe and can also be simulated in the laboratory. Experiments performed at the Omega laser study hydrodynamic, high Mach number jets [21]. The target contains a Ti disk that abuts a Ti washer. The disk is driven by the laser and then the washer forms and collimates the jet. The jet is driven into a low-density foam. The evolution of the jet, its interaction with the surrounding medium and the shock wave is observed. This work is most closely related to active galactic nucleus jets and planetary nebula outflows.

In order to draw meaningful conclusions about the various astrophysical objects that can be studied, it is valuable to have an experiment that is well-scaled to the object in question. It is most straightforward if both systems behave as an ideal compressible hydrodynamic fluid that can be described by the Euler equations.

1.3.1 Equations of Motion

The materials in these experiments can be described by the non-dimesionalized equations of motion from Radiation Gas Dynamics by Shih-I Pai [58]. First, the

continuity equation is given by,

$$\frac{\partial \rho}{\partial t} + \nabla \cdot (\rho u) = 0, \tag{1.1}$$

where, ρ is density and u is velocity. The momentum equation is as follows

$$\rho \left(\frac{\partial u}{\partial t} + u \cdot \nabla u \right) = -\nabla p + \frac{1}{Re} \left(\nabla \cdot \tau_s \right) + \frac{3R_p}{\gamma M^2} \left(\nabla \cdot \tau_R \right), \tag{1.2}$$

where the Reynolds number (Re) is the ratio of inertial force to viscous force. The parameter p is the pressure, τ_s is the viscous stress tensor, τ_R is the radiation stress tensor, and M, the Mach number, is the ratio of the flow speed to the sound speed in the material. The radiation pressure number, R_p, is the ratio of radiation pressure to gas pressure. Finally there is the energy equation,

$$\frac{\partial p}{\partial t} + u \cdot \nabla p = -\gamma p \nabla \cdot u + \frac{1}{Re} \left(u \cdot \tau_s \right) + \frac{3R_p}{\gamma M^2} \nabla \cdot (u \cdot \tau_R) + \frac{1}{Pe(\gamma - 1)M^2} \left(\nabla^2 T + \nabla \cdot q_R \right), \tag{1.3}$$

where γ is the ratio of specific heat at constant pressure to specific heat at constant volume and q_R is the radiative heat transfer flux. The Peclet number (Pe) represents the ratio of heat convection to heat conduction. When viscous effects are small, the Reynolds number is large, and the second terms of the right sides of both the momentum equation and the energy equation are small. If thermal effects are small, then Pe is large, and last term on the right hand side of the energy equation is small. Finally, when radiative effects are small, the radiation pressure number is small, and the third terms on the right hand side of both the momentum equation and the energy

equation are small. The continuity, momentum, and energy equations become

$$\frac{\partial \rho}{\partial t} + \nabla \cdot (\rho u) = 0, \tag{1.4a}$$

$$\rho \left(\frac{\partial u}{\partial t} + u \cdot \nabla u \right) = -\nabla p, \tag{1.4b}$$

$$\frac{\partial p}{\partial t} + u \cdot \nabla p = -\gamma p \nabla \cdot u. \tag{1.4c}$$

The above equations are simply the Euler equations for a polytropic gas. The parameters that represent the viscous, thermal and radiative effects for this particular experiment and the supernova as well as a further discussion of scaling this experiment to SN1987A will be discussed in Chapter II.

1.4 A Brief History of Supernova Hydrodynamics Experiments

The first supernova hydrodynamics experiments were performed by Kane (1997) [31] on the Nova laser. The experimental target was an 85 μm layer of Cu followed by a 500 μm layer of CH_2. The initial conditions consisted of a 2D, single-mode sinusoid machined onto the surface of the Cu. The pattern had a wavelength of 200 μm and an amplitude of 20 μm. The Nova laser generated a 10 – 15 MBar shock in the Cu, which decayed into a blast wave prior to reaching the CH_2 layer. These experiments were scaled so that observed hydrodynamics resembled that of the He-H interface of a core-collapse supernova. A radiograph from this experiment, which was adapted from Kane (1997), can be seen in Figure 1.7. The spikes from the Rayleigh-Taylor instability are clearly visible in this image. The diagnostic technique used in this experiment created images of lower resolution than in later experiments. While there appears to be small-scale structure present in Figure 1.7, based on the resolution, the structure is most likely due to noise.

Figure 1.7: An experimental radiograph adapted from Kane (1997) [31] showing Rayleigh-Taylor growth of Cu spikes into CH_2. The initial perturbation had a wavelength of 200 μm. This radiograph was imaged at 33.2 ns.

Subsequent supernova hydrodynamics experiments were later performed on the Omega laser [66, 19, 18, 42, 39]. With the availability of increased driving laser energy, this experiment was able to produce a 50 MBar shock in the initial material. The increased laser energy and advances in target fabrication allowed initial Omega experiments to explore the effects of coupled interfaces on hydrodynamic mixing. This experimental target had a 90 μm Cu layer followed by 150 μm thick plastic layer and a third layer of low-density Carbonized Resorsinol Formaldehyde (CRF). The Cu layer had a 2D, single-mode initial perturbation similar to the Kane (1997) experiments and the plastic layer contained a diagnostic tracer material. An experimental radiograph, imaged at 65 ns, from this experiment, adapted from Robey (2001), is shown in Figure 1.8. After the shock crosses the initial, perturbed interface, it becomes rippled. The rippled shock creates structure in the second, plastic interface. The long spikes of Cu material trail behind the spikes of plastic material.

Another supernova hydrodynamics experiment on Omega explored a spherically divergent geometry [19]. The experimental target was a hemispherical capsule which is more similar in shape to the supernova than previous planar experiments. This was another two-layer target with a Ge-doped plastic followed by low-density foam. The plastic shell had a seed perturbation with a 70 μm wavelength and a 5 μm amplitude.

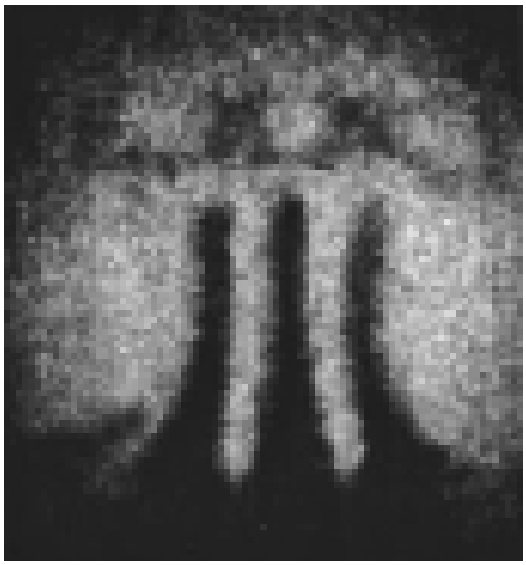

Figure 1.8: An experimental radiograph adapted from Robey (2001) [66] showing Rayleigh-Taylor growth from multiple interfaces. The long spikes are the Cu material, while the shorter spikes in front of the Cu are the plastic material. This radiograph was imaged at 65 ns.

An experimental radiograph, imaged at 13 ns, is shown in Figure 1.9a which has been adapted from Drake (2002) [19]. The curved shock, observed to decelerate like a Taylor-Sedov [76] blast wave, can be seen. Figure 1.9b is the higher magnification of Figure 1.9a and shows the Rayleigh-Taylor growth at the interface. The unstable interface appears to be breaking up in Figure 1.9b. To prevent this the plastic layer would have to be more massive, which would result in needing a higher on-target irradiance. This is not currently feasible on the Omega laser.

Using the Omega laser to shock plastic material at 50 Mbar, producing higher-velocity shocks than one could in Cu, offered the potential to obtain greater decelerations and larger unstable growth. The development of low atomic number (Z), low-density foams and improved backlighting techniques made this feasible. In response, further 2D experiments explored the effects of initial conditions of multiple modes on Rayleigh-Taylor growth. In these experiments, a planar blast wave was created in a plastic layer and then decelerated by a low-density foam layer. The laser conditions were similar to those of previous 2D experiments on Omega. Further

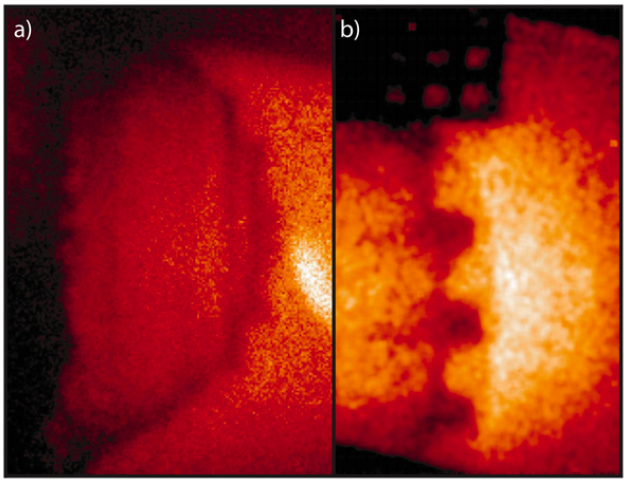

Figure 1.9: a) A radiographic image at t = 13 ns and a higher magnification image of the unstable interface shown in b). This image is adapted from Drake (2002).

details and radiographic images are shown in Chapter II and described in Kuranz (2009) [42]. My role in this work included analyzing the resulting data, comparing it to simple incompressible RT models, and performing simulations of the experiment using the 2D FLASH [23] code.

Improvements in machining allowed the progression to more complex, specifically 3D, initial conditions. The first experiments with 3D seed perturbations were reported by Drake (2004) [18]. These experiments made it clear that extensive characterization of the target was needed prior to the experiment. This is further discussed in Chapter III, Chapter IV, and Appendix D. I was centrally involved in the subsequent 3D experiments, I designed and executed the experiments at Omega. I analyzed the data, which included absolute calibration, comparison to incompressible RT models, and estimation of mass from radiographic images, and I also performed both 1D and 2D simulations of the experiments. The results of these experiments are discussed in Chapters III and IV. They benefited from improved machining capabilities and extensive characterization was performed on the targets and target components. These experiments also used a diagnostic technique that led to better quality radiographic

images than the previous 3D experiments from Drake (2004). This diagnostic technique is discussed in Appendix A.

1.5 Summary of Chapters

This introduction has provided background on SN1987A, including the progenitor star, a description of a core-collapse supernovae, and unexpected light curve data that became the motivation for these experiments. A brief summary of results from simulations of SN1987A was also provided. A background of HED physics and a description the Omega laser facility, the particular HED facility where these experiments were performed, was also given. Some examples of other laboratory astrophysics experiments and previous supernova hydrodynamics experiments were discussed. The equations of motion that describe the plasma created in this experiment and in the supernova were also provided.

Chapter II encompasses the manuscript "2D Blast-wave-driven Rayleigh-Taylor instability: experiment and simulation" [42] which has been published in the *Astrophysical Journal*. This paper discusses the initial experiments in this series, which have a 2D, sinusoidal pattern machined onto an embedded, decelerating interface. The single-mode pattern has a 50 μm wavelength and a 2.5 μm amplitude. In some cases the patterns contain multiple modes in order to investigate the interaction of modes. These experiments were performed at the Omega laser facility, where $\sim$ 5 kJ of laser energy is used to create a planar blast wave in a mm-sized target. This induces the Richtmyer-Meshkov instability followed then dominated by the Rayleigh-Taylor instability. The data are compared to incompressible models of the Rayleigh-Taylor instability. 2D simulations of the experiments were performed using the FLASH code.

Chapter III contains parts of the manuscript, "3D blast-wave-driven Rayleigh-Taylor instability and the effects of long-wavelength modes," [39] which was published in *Physics of Plasmas*. The experiments described in this chapter are very

similar to the experiments in Chapter II except that the initial conditions are more complex. The machined perturbation is a 3D structure and, in some cases, contains long-wavelength modes. The basic pattern had a 2.5 μm amplitude and orthogonal sine waves have wavelengths of 71 μm. The long-wavelength modes are added to the basic pattern in one direction and have a wavelength of either 212 μm or 424 μm. These perturbations were chosen based on an earlier experiment by Drake (2004) [18], also discussed in Chapter III, in which material was transported further than expected. It was discovered that the targets used in the earlier experiment had an unintended structure. The long-wavelength modes were added to potentially explore the consequences of this unintended structure. This data set was compared to incompressible Rayleigh-Taylor models and 3D FLASH simulations of the experiment were also performed.

Chapter IV includes the manuscript entitled, "Spike morphology in blast-wave-driven instability experiments," [40] which has been submitted for publication to *Physics of Plasmas*. This chapter further discusses the phenomena seen in Chapter III and the spike morphology observed in the experiments. The analysis of this data includes estimating the amount of mass that is being transported, in this case, to the shock front. Possible causes for this phenomenon are also discussed.

Chapter V concludes this thesis, summarizes all of its contents and presents ideas for future experiments. This thesis includes several appendices. Appendix A contains the manuscript "Dual, orthogonal, backlit pinhole radiography in OMEGA experiments" [37] published in the *Review of Scientific Instruments* and it describes the diagnostic technique used in the experiments described in Chapters III and IV. This appendix also includes an analysis of the background noise of the experiment. Appendices B and C describe data analysis techniques used in analyzing the data throughout the thesis. Appendix B is a manuscript entitled, "Assessing mix-layer amplitude in 3D decelerating interface experiments" [38] which was published in *Astrophysics and*

Space Science. Appendix C was accepted for publication by *Astrophysics and Space Science* and is titled, "Image Processing of Radiographs in 3D Rayleigh-Taylor Decelerating Interface Experiments" [41]. Appendix D describes, in detail, the specified plastic component used in these experiments. This appendix originally appeared as an appendix to the paper "Spike extensions in Rayleigh-Taylor, decelerating interface experiments," [40], which is included in Chapter IV. Appendix E contains information describing the specific experimental setup used at the Omega laser facility. Finally, Appendix F contains radiographic data from several 3D experiments and a short description of the experimental conditions under which the experiment was performed.

CHAPTER II

2D blast-wave-driven Rayleigh-Taylor instability

2.1 Introduction

This chapter shows results from experiments observing the development of the Rayleigh-Taylor [60, 70] instability with 2D initial conditions at an embedded, decelerating intefrface. Experiments are performed at the Omega Laser and use ~ 5 kJ of energy to create a planar blast wave in a dense, plastic layer that is followed by a lower density foam layer. The single mode interface has a wavelength of 50 μm and amplitude of 2.5 μm. Some targets are supplemented with additional modes. The interface is shocked then decelerated by the foam layer. This initially produces Richtmyer-Meshkov [65, 50] instability followed and then dominated by Rayleigh-Taylor growth that quickly evolves into the nonlinear regime. The experimental conditions are scaled to be hydrodynamically similar to SN1987A in order to study the instabilities that are believed to occur at the He-H interface during the blast-wave-driven explosion phase of the star. Simulations of the experiment were performed using the FLASH [23] hydrodynamics code.

2.1.1 Experimental scaling

As mentioned briefly in Chapter I the astrophysical system of interest can be scaled to an experiment performed with a high-powered laser [69]. This is possible

only when these two systems, the experiment and the relevant part of the SN, satisfy similarity conditions based on the Euler equations so their hydrodynamics will evolve in a similar way. Both systems remain invariant under a transformation of the Euler equations. The Euler equations can be used to describe both SN1987A and a well-scaled laboratory experiment if several conditions are met, which was discussed in Chapter I. First, both systems must be highly collisional. In both the experiment and the supernova the collisional mean free path is much smaller than the characteristic scale height of the system, so both systems are indeed highly collisional. Second, heat conduction must be negligible. Both systems have high Peclet numbers, which is the ratio of heat convection to heat conduction, so we can neglect heat conduction for both systems. For the SN, $Pe \sim 10^{12}$ and for the laboratory experiment $Pe \sim 10^3$. Also, the radiation flux must be small. For the SN, the photon Peclet number (Pe_γ), which is inversely proportional to the thermal diffusivity for photons, must be considered. Pe_γ is $\sim 10^5$ for the supernova, however, Pe_γ is difficult to estimate for the experiment. Therefore, the blackbody cooling time must be used to estimate the effects of radiation flux. For the experiment, the blackbody cooling time is much longer than the characteristic hydrodynamic time, therefore, the radiation flux is negligible for the experiment. Also, viscosity must be negligible. In both systems the Reynolds number, which is the ratio of the inertial force to viscous force, is large. For the experiment, the Reynolds number is $\sim 10^5$ and for the supernova, $Re \sim 2$ x 10^{10}. While the Re, Pe, and Pe_γ numbers for the two systems are different they are both sufficiently large so that the corresponding effect is minimal. Furthermore, gravitational and magnetic forces must be negligible. In a supernova explosion, the acceleration due to the explosion is far greater than acceleration due to gravity. Also, the magnetic pressure is small compared to the plasma pressure during the explosion, however, this is further discussed in Chapter IV. With all of these conditions met, we can conclude that for a finite amount of time the hydrodynamic evolution of these

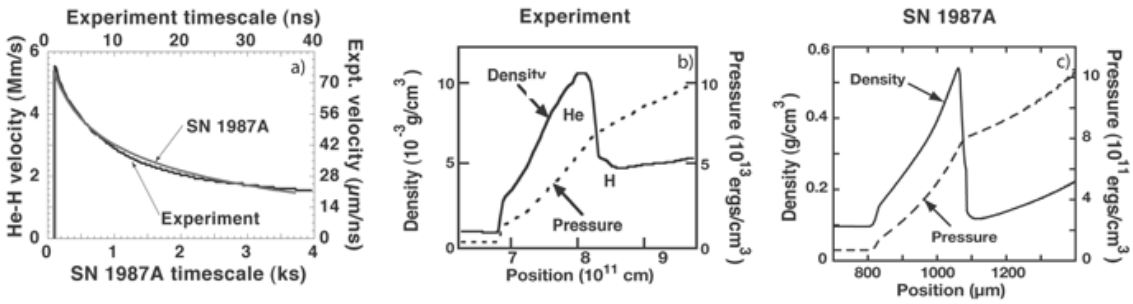

Figure 2.1: Comparison of a) interfacial velocity profiles for the laboratory experiment and the model star, and the pressure and density profiles in b) the laboratory experiment and c) the model star. Although the two systems are shown on different scales they have similar profiles. These plots were adapted from Kane (1999) [30] and Drake (2002) [19].

two systems will be similar.

When designing our experiment it is also important that the boundary conditions in space and time are also scaled to those in the supernova. Figure 2.1a shows one-dimensional (1D) simulations performed with the Prometheus [22] code of the He-H interface velocity in SN1987A vs. time, where the interface velocity is in Mm s^{-1} and the SN timescale is in ks. Figure 2.1a also shows the experimental interface velocity vs. time, which was simulated using the Hyades [45] code, where the experimental interface velocity is in μm ns^{-1}. These images were adapted from Kane (1999) [30] and Drake (2002) [19]. This plot has different time and spatial scales for the experiment and the model SN, but the motion of the interface has the same shape in both cases. This is also true for the profiles of pressure and density near the interface as seen in Figure 2.1b and 2.1c. One can see that the structures of pressure and density are very similar between the experiment and the model star, although they are not strictly identical. These similarities in spatial and temporal structure imply that the evolution of the two systems will be similar, and certainly should exhibit the same instability mechanisms for some period of time.

However, it should be noted that there are some limitations in the correspondence

between the experiment and the SN. The two materials in our experiment are an approximation of the density change in the outer layers of the supernova. In contrast to the experiment, which initially has layers of uniform density, the density of an individual layer in a star is not uniform within a layer. However, there is a much more rapid density change at the interface between two layers in the supernova. Once the blast wave crosses the interface the shape of the density profile for the experiment and SN1987A are similar as discussed above. Also, the target itself is only representative of a small portion of the supernova since it is planar and not spherical. This leads to the experiment only being well scaled for a finite amount of time. Once the disturbances from the edges of the target reach the center of the target the experiment is no longer scaled to the supernova. Even with these limitations, during the length of the experiment, up to 30 ns, the hydrodynamic instabilities that occur in the experiment are similar to those that are believed to have occurred in SN1987A.

2.2 Experimental Description

2.2.1 Experimental Target

These experiments were conducted using millimeter-scale targets designed to create a similar, scaled interfacial acceleration history to the blast-wave-driven He-H interface during the explosion phase in SN1987A. This target can be seen in Figure 2.2. The target body consists of a Be washer and shock tube. The washer has an inner and outer diameter of 950 μm and 2.5 mm, respectively. This washer is used to protect the diagnostics and outer target from the laser beams. In some cases, a gold washer coated with a thin layer of plastic was used instead of the Be washer. The Be shock tube holds the target package and has a 1.1 mm outer diameter and 150 μm thick Be walls. Inside the tube is a disk, 800 μm in diameter and 150 μm thick, of polyimide (a type of plastic), which has a chemical composition of $C_{22}H_{10}O_5N_2$ and

a density of 1.41 g cm^{-3}. Behind the plastic disk is 2 – 4 mm of CRF foam with a density of 100 mg cm^{-3}. After the passage of the blast wave, the density jump between the plastic disk and the foam provides a density jump similar to that of the hydrogen and helium interface in SN1987A as was discussed in the previous section and shown in Figure 2.1. A gold grid is placed on the outside of the shock tube for calibration of position and magnification of the resulting radiographic images. Figure 2.2a shows a cross-section of the target described above and Figure 2.2b is an image of target. This target had a plastic-coated gold washer and is mounted on a glass stalk. The two fibers protruding from the target are used for alignment of the target in the Omega chamber. The large foil attached to the target is a Ti backlighter and will be further discussed later in this chapter. These targets were fabricated at Lawrence Livermore National Laboratory.

On the rear surface of the polyimide disk a 75 μm thick, 200 μm wide slot was milled out of the plastic. A tracer strip of brominated plastic (CHBr), which has a chemical composition of $C_{500}H_{457}Br_{43}$ and a density of 1.42 g cm^{-3}, was glued into this slot. The tracer strip was used because the bromine component in the CHBr more readily absorbs the 4.7 keV backlighter x-rays than the surrounding plastic material. X-ray radiography was the primary diagnostic of this experiment so the bromine provides contrast in the radiographic images. CHBr and polyimide are predominately low Z and have similar densities, therefore, the two materials will have a similar hydrodynamic response to the extreme pressure created by the laser beams incident upon the target. Also, since the tracer strip is in the center of the target it allows the diagnostic to "look through" the polyimide surrounding the strip and Be shock tube since they are both nearly transparent to the x-rays used to diagnose the experiment. This allows the radiograph to diagnose primarily a slice through the center of the target, unaffected by edge effects along any given line of sight. Also, one experiment was performed without a shock tube to learn how the interaction with

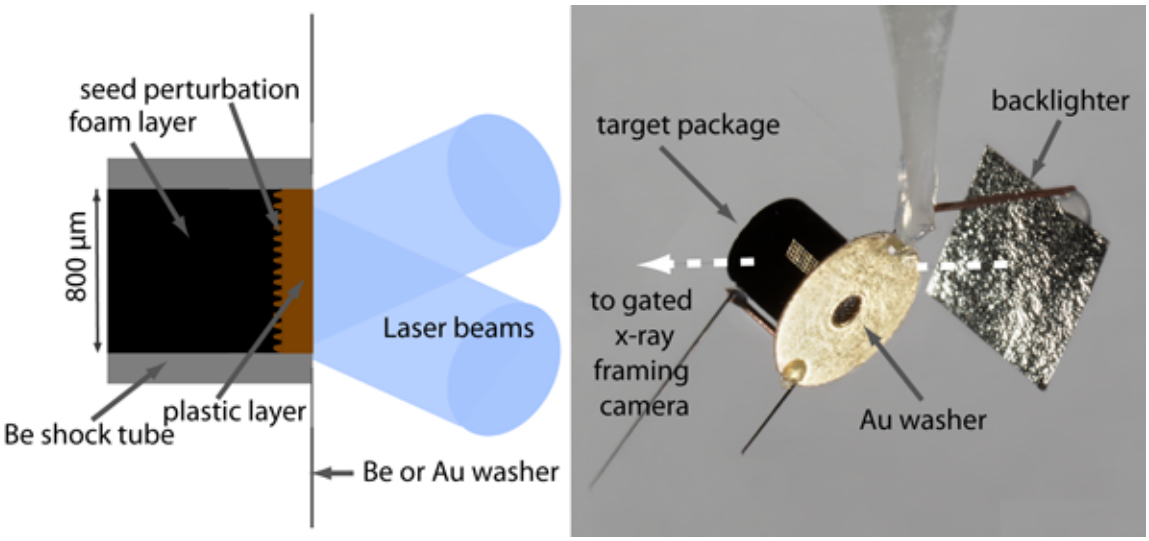

Figure 2.2: The experimental target. a) Shown in cross-section with a washer and shock tube. Inside the shock tube is a high-density plastic layer and a lower density foam layer. The plastic layer has a seed perturbation machined at the interface between the two materials. The laser beams irradiate the plastic component of the target. A photograph of the target is shown b). This target has a plastic-coated Au washer. This image also shows the glass stalk on which the target is mounted and gold fiducial grid. The backlighter foil is positioned 4 mm from the target opposite the diagnostic, a gated x-ray framing camera.

the tube walls affects the results.

Several different types of 2D sinusoidal patterns have been machined onto the rear surface of the plastic disk. These patterns serve as a seed perturbation for the Rayleigh-Taylor instability. The purpose of these patterns is to determine whether or not more complex seed perturbations lead to the displacement of more material. The basic machined pattern is a single-mode sine wave, $a_0 * cos(k_1 x)$ where $a_0 = 2.5\mu$m and $k_1 = 2\pi/(50\mu\text{m})$. The majority of experiments performed with a single-mode perturbation were done with the aforementioned specifications, however, some of the experiments had target interfaces with a longer-wavelength single-mode pattern, where $a_0 = 2.5\mu$m and $k_1 = 2\pi/(100\mu\text{m})$. For clarity, the former perturbation will be referred to as single-mode and the latter will be referred to as long-wavelength single-mode. The more complex patterns have multiple sine waves. The 2-mode pattern is defined by

$$1.5\cos\left(\frac{2\pi x}{60\mu\text{m}}\right) + 1.25\cos\left(\frac{2\pi x}{40\mu\text{m}}\right) \tag{2.1}$$

Also, there is an 8-mode perturbation defined by

$$\sum_{i=1}^{8} a_i \cos\left(\frac{2\pi x}{\lambda_i}\right) \tag{2.2}$$

where $\lambda_i = (180\mu\text{m})/i$. The amplitude components, a_i, range from 0.4 μm to 0.7 μm and are shown in Table 2.1, with the total amplitude for the multimode perturbation being about 2.5 μm, similar to the 2-mode and single-mode patterns. Cross-sections of these three perturbations can be seen in Figure 2.3. The experimental perturbations were chosen based on the length scale of the system as well as the ability to easily diagnose the growing perturbation.

Some of the plastic components were machined with a flat surface. Experiments using such targets can determine the position of the one-dimensional, or "mean, fluid

i	λ_i	a_i
1	180	0.602669
2	90	0.502309
3	60	0.526604
4	45	-0.683793
5	36	0.564115
6	30	-0.625269
7	25.7143	-.474363
8	22.5	-.546737

Table 2.1: A description of the 8-mode perturbation is shown in this table. The subscript, i, indicates a specific mode, λ_i and a_i, indicate the wavelength and amplitude of that mode, respectively. Note that $\lambda_i = (180\mu\text{m})/i$ and the total amplitude of the pattern is ~ 2.5 μm.

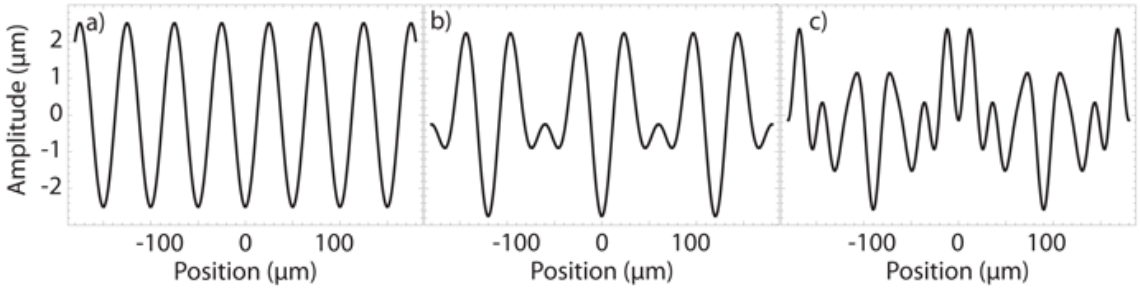

Figure 2.3: Cross-sections of the (a) single-mode (1-mode), (b) 2-mode and (c) 8-mode seed perturbations. The patterns are machined onto the plastic component of the target in one direction as a ripple. The overall amplitudes of all the patterns are about 2.5 μm.

interface. In contrast, one cannot directly determine the actual mean interface in experiments with sinusoidal surfaces, as one cannot determine the relative amplitude of the spikes and the bubbles. The best one can then do is to estimate the mean interface position from the midpoint between the bubbles and spikes. All of the plastic components, the planar and patterned surfaces, have some amount of small grooves due to the tools used in the machining process. This surface roughness is akin to having additional short-wavelength, small-amplitude modes on the surface. These modes, while small, will still cause some Rayleigh-Taylor growth, however, on the sinusoidal patterns these small modes will be damped and the larger modes will dominate.

2.2.2 Experimental Conditions

Ten Omega [7, 6] laser beams with 1-ns flat-topped pulse shapes irradiate the dense plastic disk of the target. The laser beams have a wavelength of 0.35 μm. Each beam passes through a Distributed Phase Plate (DPP) that produces a spot size of 820 μm FWHM that is smooth overall with fine speckles on a 5 μm scale. The total energy of the beams is $\sim$ 5 kJ and the average irradiance is $\sim 9.5 \times 10^{14}$ W cm^{-2}, producing an ablation pressure of $\sim$ 50 Mbars in the plastic layer of the target. This large pressure difference in the plastic layer creates a strong shock wave.

This shock wave traverses about halfway through the 150 μm dense plastic layer in the 1 ns while the laser is activated. After the laser pulse ends, the plasma that has been created is allowed to freely expand away from the irradiated surface. This causes a rarefaction wave, a decrease in density and pressure due to outward flow, to overtake the shock wave. Then the abrupt acceleration of the shock is followed by the extended deceleration in the rarefaction, creating the desired planar blast wave structure moving toward the interface between the plastic and foam. At about 2.2 ns the blast wave crosses this interface, launching a forward shock into the foam. The

density ratio between the plastic and the foam is greater than can be sustained by a single shock, causing a rarefaction to move backwards. This rarefaction causes the plasma behind the interface to accelerate and begin to accumulate at the interface. The accumulation of shocked foam ahead of the interface causes it to decelerate relative to the plasma flowing toward the interface from the denser matter. As the ram pressure of the inflowing plasma, in the plane of the interface, increases above the thermal pressure of the shocked foam a reverse shock forms.

The creation of this blast wave structure was simulated using the Hyades code, a 1D, Lagrangian, code with a multigroup flux-limited diffusion radiative transport model. Although the radiation transport model is not as accurate as the full treatment of the radiative transfer equation and while 2D effects play an important role in our experiments, 1D Hyades remains a useful tool for experimental scoping and analysis. In its Lagrangian description, the computational mesh that describes the target moves with the material so that each element of mass in the mesh is conserved over time. Hyades uses equations that describe a three-temperature, single-fluid. The pressure in the continuity and momentum equations represent the summed contributions from electrons, ions, and radiation. There is an energy equation for ions, for electrons, and for each radiation energy group. Electron heat transport is approximated by flux-limited diffusion. The multigroup radiation approximation allows the user to assign energy ranges to many different photon groups, for each of which the opacity is calculated using an average atom model.

Simulation codes similar to Hyades are known to overestimate the ablation pressure when run in 1D with an actual laser irradiance in the range of the present experiments [62]. This is due at least in part to the absence of lateral heat transport in one dimension. In order to correct for this unrealistically large ablation pressure the laser irradiance is reduced in simulations. To quantify this reduction, Hyades runs were performed at different irradiances and the shock and mean interface positions

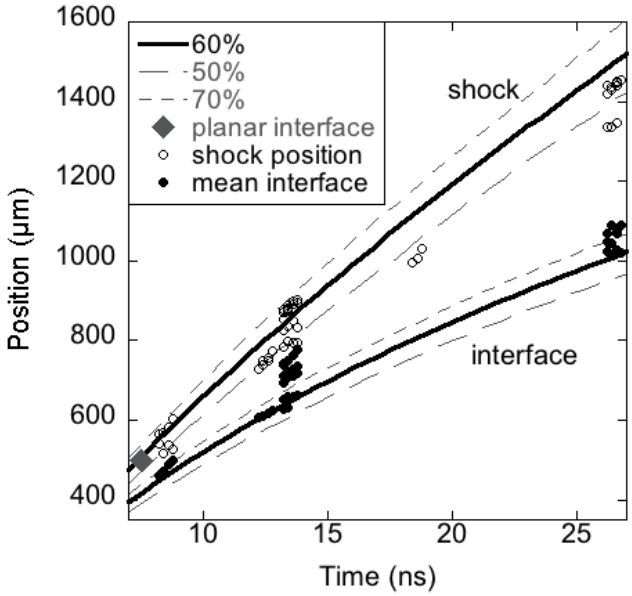

Figure 2.4: Plots of shock and interface positions vs. time for the experiment and Hyades simulation at several different laser intensities. The laser intensities are 50%, 60%, and 70% of the nominal laser energy. The shock and interface positions are shown as lines, with the shock positions being greater than the mean interface positions. The experimental shock position is shown with open circles and the experimental mean interface position, the average of the spike-tip and bubble-tip positions, is indicated with black circles. The gray triangle indicates the position of the interface in a target machined with a flat interface i.e. no perturbation.

were found. These positions were compared to the experimental shock and mean interface positions. These results are shown in Figure 2.4. It shows that Hyades, run with a laser irradiance of 6.0×10^{14} W cm^{-2}, or about 60% of the actual value, best represents the experimental data. The positions of the shock and mean interface are also shown for 50% and 70% of the nominal laser irradiance. One can see that variations of about $\pm$ 10% in the reduced laser irradiance do not reproduce the data nearly as well.

Even though using an irradiance of 6.0×10^{14} W cm^{-2} matches the general trend in the data, one can see that there is a large dispersion of experimental data points. For example, at t = 13.4 ns the shock position varies by ~ 150 μm and the interface position by ~ 100 μm. These differences are comparable to the lengths of the spikes

and bubbles in the experiment. These shot-to-shot variations are most likely due to small differences (e.g. laser energy, target alignment, target fabrication, target metrology) in the experiment, which lead to errors in the inferred absolute position of features. Of these variations, the laser energy for each shot is well known. For the data shown in this chapter the laser energy generally varied by about ± 7%. However, for three of the shots, the irradiance was 30% less than the nominal laser irradiance due to a reduction of beams. These variations cause a change in the shock and interface position of $\sim$ 6% according to Hyades simulation results at the time this particular experiment was observed.

A simulation of how the desired blast-wave structure is created can be seen in Figure 2.5. Figure 2.5a is a plot of density vs. position, Figure 2.5b is a plot of pressure vs. position, and Figure 2.5c is a plot of velocity vs. position. Each line on the plots represents a different time. These plots are at t = 0 ns, 1 ns, 2 ns, 4 ns. The gray, dashed line in the density plot shows the initial condition (t = 0 ns) of the dense plastic layer followed by the lower density foam. The laser beams irradiate the plastic and in this case would come from the left side of the plot. At t = 1 ns the pressure is $\sim$ 5 $\times 10^{13}$ dynes cm^{-2} or $\sim$ 50 Mbars, which has caused a shock wave, visible at $\sim$ 65 μm moving at $\sim$ 52 km s^{-1}. At 1 ns the laser beam pulse has ended and by 2 ns a blast wave has developed with the leading edge at $\sim$ 130 μm from the front surface of the target. The blast wave crosses the interface at $\sim$ 2.2 ns and the forward shock is then launched into the foam. At 4 ns the shock is moving at $\sim$ 58 km s^{-1} and located at $\sim$ 270 μm while the interface behind it is moving at $\sim$ 54 km s^{-1} and is located at $\sim$ 240 μm.

The experiment is observed at times much later than when the shock crosses the interface. Figure 2.6 shows results of Hyades simulations of the experiment at times of 8, 14, 20, and 26 ns. At 8 ns the shock can be seen at $\sim$ 575 μm, the interface is at $\sim$ 450 μm. At this time, the shock and interface have slowed down considerably

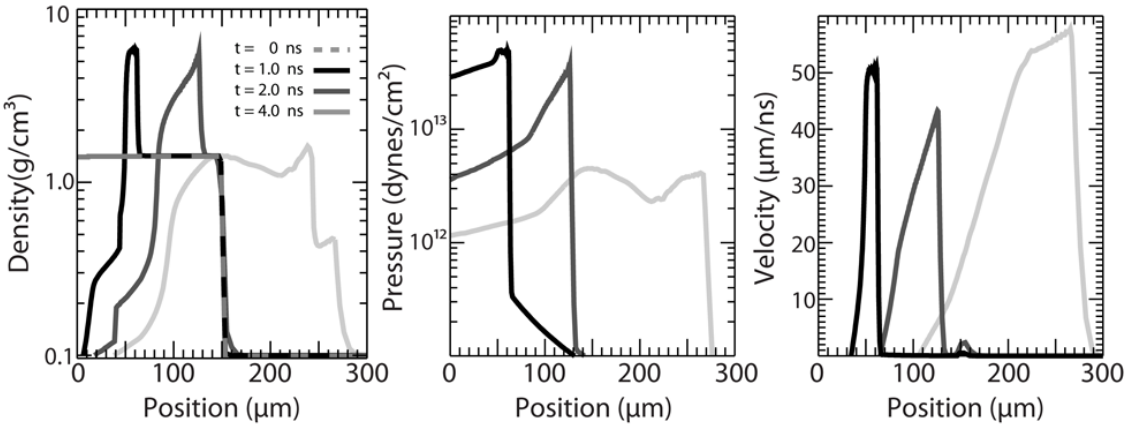

Figure 2.5: Plots from Hyades simulations showing (a) density, (b) pressure and (c) velocity vs. time. Each line on the plot indicates a different time during the experiment. The times shown are t = 0 ns, 1 ns, 2 ns, and 4 ns. The density plot best illustrates the formation of a blast wave. The initial condition of a dense layer followed by a lower density layer is shown at t = 0 ns. The laser beams irradiate the plastic material and a shock wave forms by 1 ns. The laser pulse ends allowing the material to decompress and a rarefaction forms. This rarefaction wave overtakes the shock wave forming a blast wave. The blast wave crosses the interface at $\sim$ 2.2 ns.

to 50 km s^{-1} and 42 km s^{-1}, respectively, and they continue to decelerate. By 26 ns, the shock and interface have moved to have 1500 μm and 1000 μm, respectively. The acceleration of the interface due to the planar blast wave is similar in SN1987A and our experiment as discussed earlier. The interface is unstable to the Richtmyer-Mehskov [65, 50] instability due to the strong shock crossing the interface and Rayleigh-Taylor instability due to the deceleration phase behind the shock front. Similar dynamics occur within a core-collapse supernova in which the dense, core layers are shocked then decelerated by the less dense, outer layers. In the experiment, the Richtmeyer-Meshkov instability dominates in the first few nanoseconds, but the rate of amplitude increase quickly becomes small compared to the growth rate of the Rayleigh-Taylor instability [67]. This experiment is observed when the Rayleigh-Taylor growth is dominant.

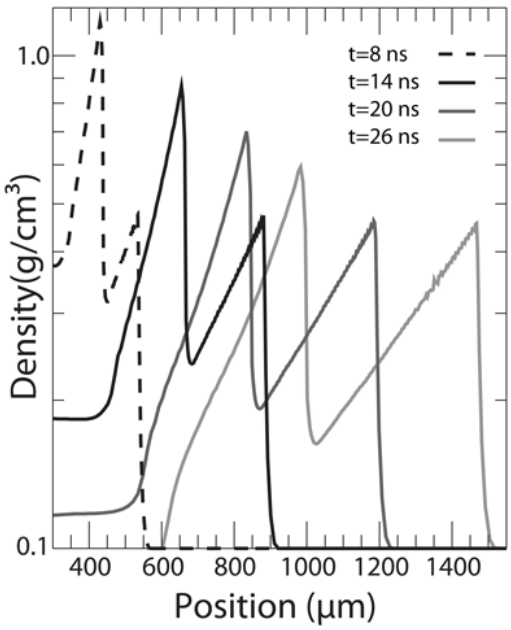

Figure 2.6: Hyades simulation of density vs. position for late times: t = 8 ns, t = 14 ns, t = 20 ns and t = 26 ns.

2.2.3 Diagnostics

The main diagnostic for this experiment in this chapter is x-ray radiography using a gated x-ray framing camera [8]. As can be seen in Figure 2.2, an area backlighter, a 4 x 4 mm, 5 μm thick Ti foil is attached to the target via a 4 mm long wire. The backlighter is placed on the side of the target that is opposite the diagnostic. The material of the foil is chosen by matching the energy of the He-alpha emission of the foil to $\sim$ 10% transmission of radiation through the target estimated using a cold opacity library. In this experiment, Ti was used for a He-alpha energy of 4.75 keV. Six to eight Omega beams with 670 μm to 750 μm spot size irradiate the front and back of this foil creating x-ray photons, at some time delayed 8 to 26 ns from the leading edge of the drive beams. These photons pass through the target and are imaged by a 4 x 4 array of pinholes and a gated x-ray framing camera.

At the front of the framing camera is a microchannel plate (MCP) that generates electrons from the incoming x-ray photons. The electrons are accelerated and multi-

plied by a gating pulse. Behind the MCP is a phosphor plate that is at 5 kV while the back of the MCP is at ground. The positive potential accelerates the electrons so that they emit light when they strike the phosphor plate. These visible photons then go to a CCD camera or film.

The result is a set of 16 images on 4 strips. The time delay between the rows is adjustable and was typically set to 200 ps. The images along a given strip, separated in time by 70 ps, are analyzed to give a single shock and interface position at an appropriately averaged time. When the diagnostic is well aligned and works well, one obtains several measurements of positions on a given shot. This can be seen in Figure 2.4 where there are several points clustered in one area. The features measured on these images for this chapter are the shock position, spike-tip position and bubble-tip position. Recall that Figure 2.4 shows the mean interface position, which is taken to be halfway between the spike tip and bubble tip. The positions of these features are found by taking a profile across the feature. The pixel intensity in the image will vary across the specific feature. The position is determined to be halfway between the start and end of the variation in intensity. This leads to an error in the measurement of nominally 10 μm for each feature. The data analysis method and error associated with these measurements is further discussed in Chapter III, Appendix B and Appendix C. In Figure 2.4 one can see that the position of the mean interface and shock have a fluctuation of greater than 10 μm or, combining the error of the spike-tip and bubble-tip position, 14 μm in the case of the mean interface. This is due to the shot-to-shot variations discussed previously, which affects the absolute calibration of the radiographic images. This leads to a variation approaching $\pm$ 10 % in the calibrated data.

2.3 Experimental Results

2.3.1 Experimental Radiographs

X-ray radiographs of experiments performed using targets with a single-mode interface can be seen in Figure 2.7. These are images of an experiment with a single-mode interface with a 50 μm wavelength. The results of targets having a longer-wavelength (100 μm) single-mode pattern are not shown, but are very similar to the images in Figure 2.7. It is worth noting some features in this and later images. The target coordinate x = 0 μm is at the front surface of the dense plastic material where the laser beams irradiate the target and the target coordinate y = 0 μm is at the axis of the target. Figure 2.7c has a triangular region in the upper right corner of the image where the detector was not active. In these images the shock, which is moving to the right, can be seen, as the rightmost transition. The interface has become convoluted, so that one sees dark features extending to the right and light features extending to the left. The dark fingers are spikes of dense material moving to the right. In between the spikes are bubbles of lower density material moving to the left relative to the interface. The spikes and bubbles are due to the Rayleigh-Taylor and Richtmeyer-Meshkov instabilities. In Figure 2.7a the shock is visible ahead of the interface at $\sim$ 550 μm. The reverse shock, at the left edge of the dark vertical feature, is at 400 μm. Further to the left one can see the left edge of the CHBr.

Figures 2.7a, 2.7b, and 2.7c were taken at t = 8 ns, t = 12 ns, and t = 26 ns after the drive beams irradiated the target, respectively. In these radiographs, note the increasing distance between interface and the shock as well as the decrease in definition of the interface and the reverse shock at later times. Also, note that the spikes appear longer at later times; this is due to both the unstable growth and the gradual expansion of the system as the pressure decreases. Figure 2.7b clearly shows some roll-up on the edges of the target due to Kelvin-Helmholtz effects from the

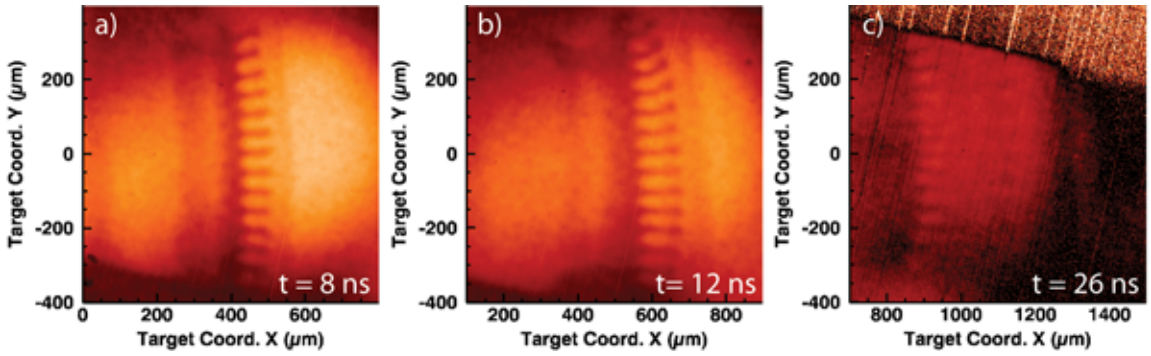

Figure 2.7: X-ray radiographic images of experiments performed with targets that had a single-mode pattern machined on the plastic component. In each image the interface and shock wave are moving to the right. The images were taken at the following times: (a) 8 ns, (b) 12 ns, and (c) 26 ns.

interaction between the plasma and the tube walls. In all of these images the tips of the spikes appear to be thicker than the rest of the spike structure, which is also due to Kelvin-Helmholtz-like effects.

Experimental images of targets with a 2-mode perturbation can be seen in Figures 2.8a, 2.8b, and 2.8c. These radiographs were taken at 13, 20, and 26 ns after the start of the initial laser pulse. Along the top of the image a gold calibration grid can be seen. In Figure 2.7a, the modal structure of the perturbation can be clearly seen. This definition of the structure decreases with time until it is no longer readily visible at 26 ns. Radiographs of the 8-mode interface are shown in Figure 2.9a and 2.9b at 13 and 26 ns, respectively. Again, the modal structure is quite distinct early in time. The structure is less definite at t = 26 ns, but it is still visible. Figure 2.9c shows a radiographic image of a target with a planar interface taken at 8 ns. The interface is visible at $\sim$ 500 μm and is moving to the right, but the forward shock and reverse shock cannot be seen in this image.

The radiographic images shown in this chapter have been calibrated using the gold grid. The spacing between grid wires is 63 μm, which is used to find the magnification of the image. For these images, the nominal magnification is 8, but the

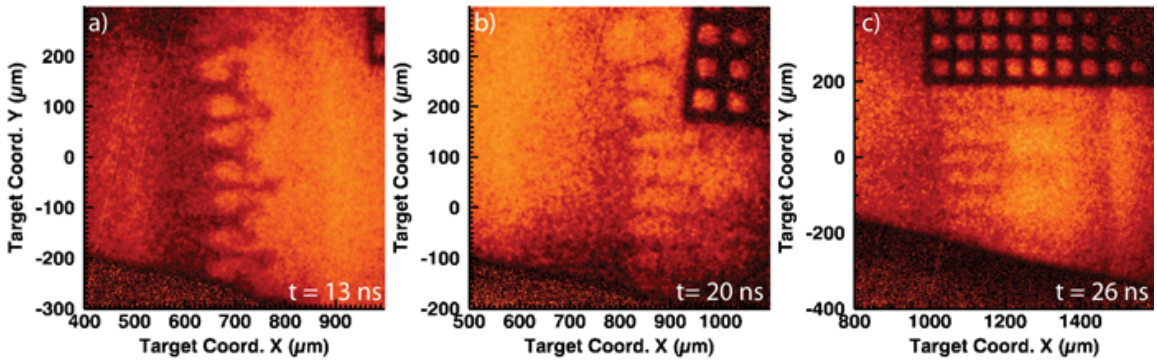

Figure 2.8: X-ray radiographic images of experiments performed with targets that had a 2-mode pattern machined on the plastic component. The images were taken at the following times: (a) 13 ns, (b) 20 ns, and (c) 26 ns. The complex structure is very different from the single-mode pattern and is due to the initial conditions.

actual value varies between 7.84 and 8.97. The magnification varies due to errors in target alignment, location of the area backlighter, and location of the x-ray framing camera. The location of the grid is measured with the respect to the driven surface of the target prior to the experiment. Using the grid location and magnification, the absolute positions of the shock, spike tip, bubble tip and other features are found.

The mean interface in experiments performed with a machined sinusoidal pattern is defined here as the average of the spike-tip and bubble-tip positions. The analysis was performed this way because the unperturbed interface position is not known. An experiment was performed using a plastic component that was machined to a flat surface in order to compare with the mean interface of an experiment executed with a machined perturbation. The results shown in Figure 2.4 show that the planar interface, indicated by the gray diamond at t = 8 ns, falls on the curve of the mean interface position versus time, and shows the mean interface from all the experiments with machined patterns. These are certainly consistent within the experimental variability.

The spike-tip and bubble-tip position vs. time for different types of perturbations can be seen in Figure 2.10. This shows how far the spikes have penetrated into the

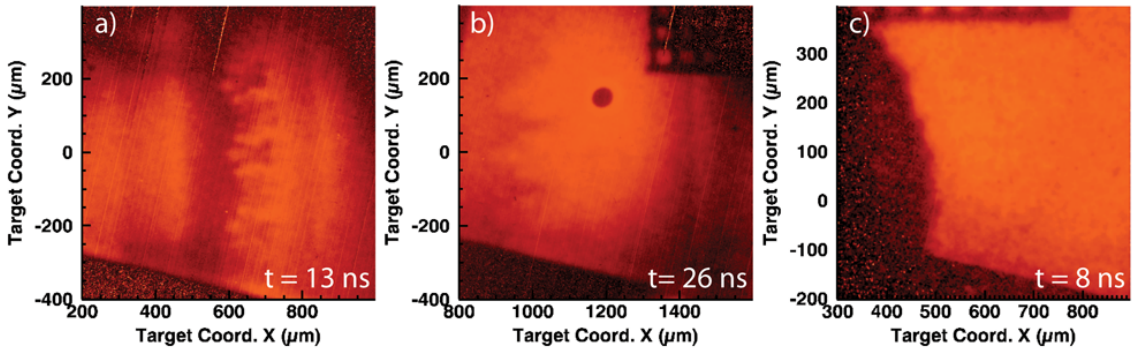

Figure 2.9: X-ray radiographic images of experiments performed with targets that had a 8-mode pattern machined on the plastic component. These images were taken at (a) 13 ns and (b) 26 ns. The image in c) shows an x-ray radiograph of a target with a planar interface taken at 8 ns. The interface is visible at $\sim$ 500 μm and is moving to the right. The forward shock is not visible in this image.

foam material with respect to time, and that the total spike penetration is generally increasing with time. The error bars in this image are roughly the size of the symbol and therefore, are not shown. For the multimode experiments, where some spikes penetrate farther than others, the position of the spike tip shown is referring to the farthest protruding spike. Likewise, the bubbles are moving in the opposite direction, while the entire interface is moving due to the background fluid motion. This plot also shows the mean interface from a 1D Hyades simulation indicated by the black line. The spikes and bubbles generally fall on either side of the simulated interface, as expected. However, this figure shows a rather large spread in data and in some cases shows a spike (bubble) in front of (behind) the mean interface giving nonsensical negative amplitude for the feature. In order to accommodate the large spread in data while still being able to draw a meaningful conclusion, this thesis will refer to the mix-layer amplitude, half the distance between the spike tip and bubble tip, as a surrogate for individual spike and bubble amplitudes.

Figure 2.11 shows the amplitude of the mix layer vs. time. The mix-layer amplitude is also increasing with time. These data points generally fall on a straight

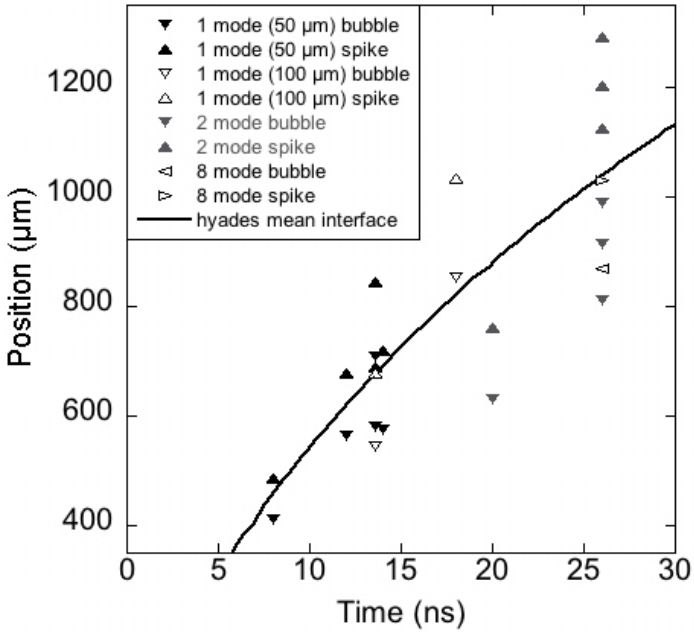

Figure 2.10: Plot of spike-tip and bubble-tip positions vs. time. Targets with different seed perturbations are differentiated by different triangles. The mean interface from a Hyades simulation is also plotted and indicated by line shown. The error bars for this data are smaller than the symbol size and therefore, not shown.

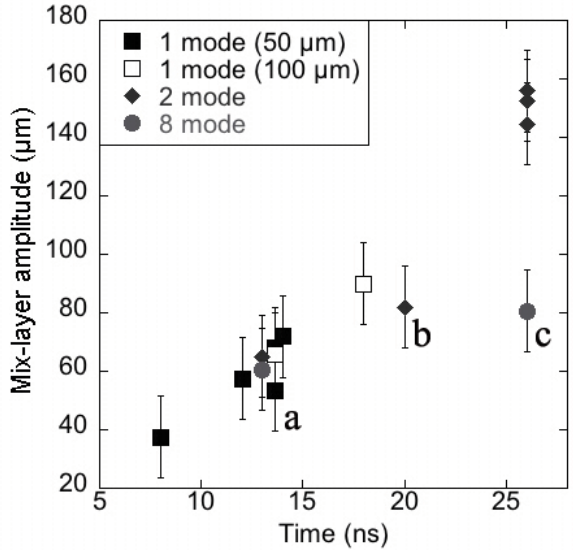

Figure 2.11: Plot of mix-layer amplitude for the varying seed perturbations used for these experiments. The mix-layer amplitude is defined at the spike-tip position subtracted from the bubble-tip position and divided by 2.

line and based on this data one cannot resolve a difference due to the type of perturbation used during the experiment. There are three outliers in this plot, which will be discussed. The point labeled A was an experiment performed without a Be tube. One can hypothesize that the system was able to freely expand laterally and that this led to less forward growth of the interface. The point labeled B was a 2-mode experiment and the result is seen in Figure 2.8b. The analysis of other 2-mode experiments found the position of the most protruding spike, however, in Figure 2.8b the only spikes visible are the shorter spikes. This would account for the smaller mixing layer amplitude. Point C is an 8-mode experiment seen in Figure 2.9b. Due to the poor contrast in this image it is unlikely that the end of the spike can be seen and therefore it has smaller amplitude. These three outlying points are deleted from later plots.

2.3.2 2D Simulations

Simulations of these same experiments were previously performed using the simulation code CALE [2] and were reported by Miles (2004) [52]. The simulations presented in this chapter were performed using the FLASH [23] code. FLASH is used to model general compressible flow problems common to complex astrophysical systems, including x-ray bursts, classical novae, and Type Ia supernovae. This multidimensional code solves the Euler equations using the Piecewise Parabolic Method (PPM) [12]. FLASH allows for adaptive mesh refinement, using a block-structured adaptive grid and placing resolution elements only in areas where refinement is needed most. These simulations were performed using 2D Cartesian geometry. A gamma law equation of state (EOS) model was used with gamma defined as 1.4 for both the plastic and foam, (appropriate to the partially ionized media used here [15]).

The FLASH code does not include the means to accurately model what happens while a laser is irradiating a material. Therefore, the output from a 1D Hyades

simulation is used as input for a FLASH simulation to set the initial conditions of the simulation as a laser irradiance. The initial setup is the same as for the Hyades simulations described previously except that the perturbations used in the experiment have been included. These simulations did not include the Be tube that is used in the experiment. However, the boundary where the tube would be, parallel to the target's symmetry axis, is set to be reflective. The boundaries perpendicular to the target's symmetry axis are out-flowing.

The simulations were set to refine in areas where there was a large change in pressure and concentration of polyimide between neighboring zones. This allows for refinement near the interface and the shock. The domain of this simulation was the size of the inner diameter of the Be tube in the experiment. The resolution for the single-mode and 2-mode simulations was about 0.78 μm, corresponding to 50 resolution elements per wavelength for the smallest wavelength. The simulation for the 8-mode pattern was performed at higher resolution, 0.39 μm but at similar resolution elements per smallest wavelength. Resolution studies on similar systems have shown that this resolution is sufficient and that results with a higher resolution simulation will only differ in the small-scale structure [9, 52].

Figure 2.12 shows results from FLASH simulations for three different types of initial conditions. These images plot the density of the simulation where the darkest region indicates the densest feature. Figure 2.12a shows a FLASH simulation at t = 12 ns with a single-mode initial perturbation. This can be compared to an experimental radiograph at the same time in Figure 2.7b. Simulations were also done with a long-wavelength single-mode pattern, but are not shown, as they are very similar to the simulations shown in Figure 2.12a. Figure 2.12b show a FLASH simulation with a 2-mode initial perturbation at t = 13 ns. An experimental radiograph with the same initial condition and time is shown in Figure 2.8a. Figure 2.12c shows a simulation of a target with an 8-mode initial perturbation at t = 13 ns. The analogous experimental

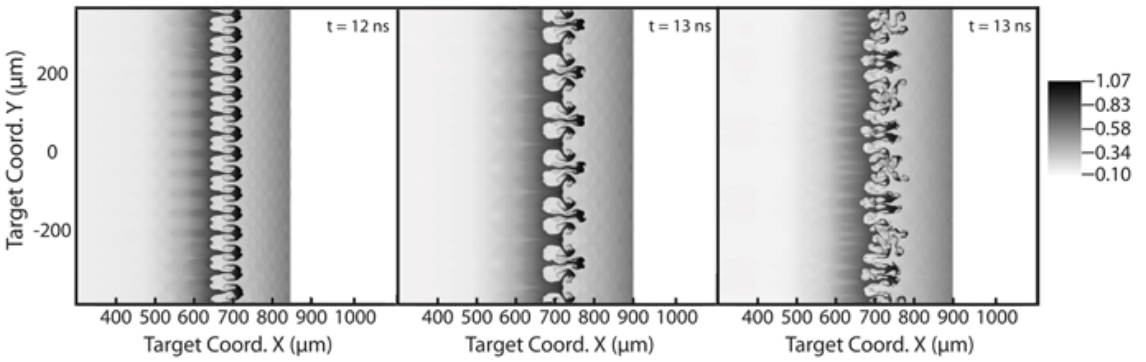

Figure 2.12: 2D density plots from FLASH simulations of a) a 1-mode experiment at t = 12 ns, b) a 2-mode experiment at t = 13 ns and c) an 8-mode experiment at t = 13 ns.

radiograph is shown in Figure 2.9a.

Overall, the mix-layer amplitude resulting from the simulations shows good qualitative agreement with the mix-layer amplitude from the experiments. Due to the higher resolution of the simulation, more detail can be seen than in the experimental radiographs. Also, the shocks in Figure 2.12 are very flat, while the shock and interface appear to be slightly curved in the experimental radiographs. These simulations do not contain a Be tube as the experiment does, therefore, the edges of the simulation domain are not slowed down by interaction with the tube. Also, the edges of the domain do not expand laterally as Be tube does during the experiment. This will cause the shock to appear overly planar in the simulation and move faster than the shock wave in the experiment. Finally, the initial laser condition was set by a 1D Hyades simulation with flat laser irradiance. In the experiment, the laser irradiance profile has a curved shape due to the overlapping of several beams. This causes the ablation pressure to be largest in the center of the target causing the shock and interface velocity to be slightly larger at that point. This will position the center of the shock and interface slightly ahead of their respective edges making them appear curved.

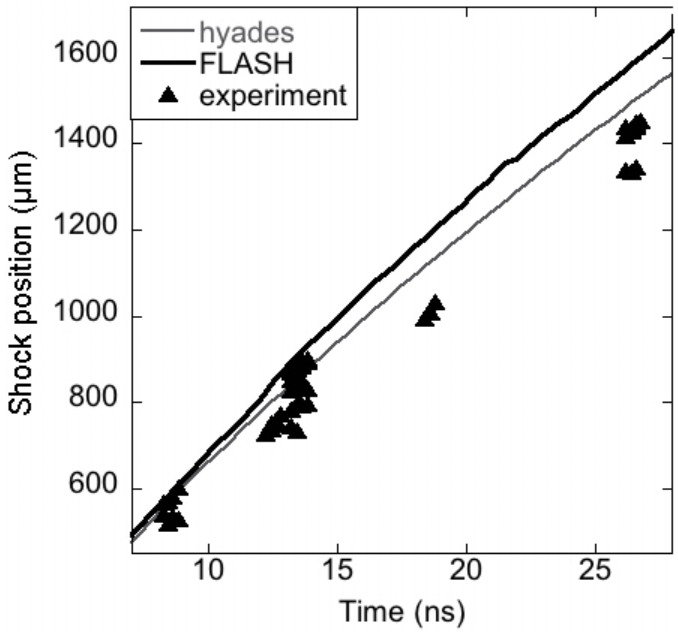

Figure 2.13: Comparison of shock positions from 2D FLASH simulations, 1D Hyades simulations and experiment.

These simulations were analyzed using a method that was similar to the method used to analyze the experimental data. Instead of relying only on the pixel intensity of the radiograph, the polyimide mass fraction and density of a selected region were used. The data are divided into 5 μm bins and the polyimide mass fraction and density are given for each bin. The position of the spike tip or bubble tip is found by averaging over several bins when there is a decrease in polyimide mass fraction or density. There is an error of $\pm$ 10 μm for a spike-tip or bubble-tip position and combining these gives an error of $\pm$ 14 μm for the mix-layer amplitude. Figure 2.13 shows the position of the shock from a FLASH simulation, Hyades simulation, and experiments. At late times, the FLASH simulation over predicts the position of the shock. This is most likely due to using a constant gamma of 1.4 for the EOS and the fact that the domain does not allow for lateral expansion as mentioned previously. Miles (2004) showed that adjusting the gamma of the foam had an effect on the shock position, but little effect on the interface position [52].

It is also valuable to compare the amplitude of the mix layer, defined as half the

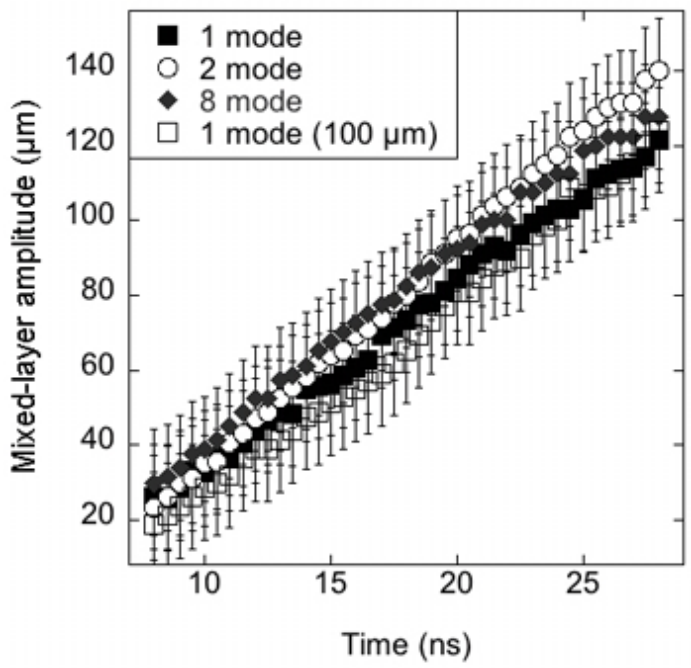

Figure 2.14: Mix-layer amplitude from FLASH results for each perturbation type.

difference of the bubble-tip position and spike-tip position, for simulations performed with different initial conditions. A plot of mix-layer amplitude is shown in Figure 2.14 for the simulation of different initial conditions. All of the simulations show the mix layer increasing with time as is seen in the experiment. There are small differences in the mix-layer amplitude between the individual types of perturbations. Initially, the amplitudes are all within 10 μm of each other, but by 28 ns the experiments performed with a 1-mode perturbation and a 2-mode perturbation differ by ~ 20 μm. It should be noted that the error for these measurements is $\pm$ 14 μm so the mix-layer amplitude for different types of initial conditions show similar growth within error. This was also the case in the experiment.

Figure 2.15 shows the mix-layer amplitude for the simulation and the mix-layer amplitude for the corresponding initial condition from the experiment. Figure 2.15a shows the single-mode mix-layer amplitude for the experiment and FLASH simulation for both types of single-mode patterns. Figure 2.15b shows the results for the 2-mode experiment, and Figure 2.15c show the results for the 8-mode. In general, the FLASH

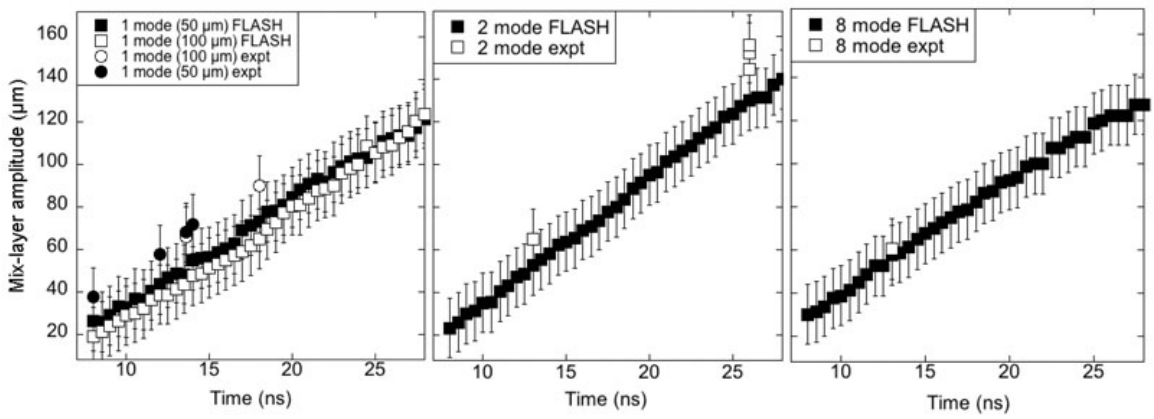

Figure 2.15: Comparison of FLASH mix-layer amplitude with the a) 1-mode experiment, b) 2-mode experiment, and c) 8-mode experiment.

simulations show slightly less growth than the experiment, but the simulations and experiments agree within reasonable error.

2.3.3 Buoyancy-Drag model

The growth of the mix layer seen in decelerating interface experiments is not entirely due to instabilities. Another significant contributor to mix-layer growth is material expansion. If one hopes to compare the results to simple incompressible models, then it is an important part of data analysis to correct for the expansion of the mix layer. The following explains how we evaluated the expansion amplitude on the basis of the data and of Hyades simulations. The total width or amplitude of the mix layer, h, as shown in Figure 2.11, is a combination of the expansion amplitude, h_{exp}, and the instability amplitude, h_{inst} shown by

$$h = h_{inst} + h_{exp} \tag{2.3}$$

Ideally, h from equation 2.3 would be the spike or bubble amplitude, which is the difference between the spike-tip or bubble-tip position and the mean interface position from the 1D simulations. However, finding the feature amplitude this way is rather

difficult as discussed earlier and instead reference will be made to an overall mix-layer amplitude, half the distance between the spike tip and bubble tip.

The expansion amplitude, h_{exp} from Equation 2.3, is the integral of the velocity of expansion of the mix layer due to the overall expansion of the fluid. This cannot be directly measured from the experiment so a combination of data and 1D simulation results are used. The instantaneous expansion velocity of the spike and bubble is obtained by taking the difference in velocities from the Hyades simulation at the experimental spike-tip or bubble-tip positions. These velocities contain no information about the instability since they are obtained from a 1D simulation. The integral of the instantaneous net expansion velocity results in the net expansion amplitude of the entire mix layer. For the analysis described above the net expansion is divided by 2 to obtain the expansion amplitude, h_{exp}. This analysis was performed separately for the experiments executed using targets with 1-mode and 2-mode type patterns because experiments using these two types of patterns resulted in the most data. Figure 2.16 shows the mix-layer amplitude, h, the expansion amplitude, h_{exp} and the effective incompressible instability amplitude, h_{inst}. The figure indicates that roughly half of the mix-layer growth is due to the instability and half is due to expansion.

Once the material expansion is subtracted from the data an incompressible model for Rayleigh-Taylor mixing, such as the buoyancy drag model, can be compared to the data. From Oron (2001) [57] and Dimonte (2000) [13] a 2D instability front can be described by

$$(\rho_1 + 2\rho_2)\,\frac{du}{dt} = (\rho_1 - \rho_2)\,g(t) - \frac{6\pi}{L}\rho_2 u^2 \tag{2.4}$$

where u is velocity in μm ns^{-1}, g is acceleration in μm ns^{-2}, ρ_1 and ρ_2 are the post-shock densities of the fluids on either side of the interface. The acceleration of the interface was found from a simulation to be $g = -7.5(t/t_0)^{-1.2}$ and the ratio of the densities is $\frac{\rho_1}{\rho_2} = 4.26$. L is the dynamical length scale of the mixing zone.

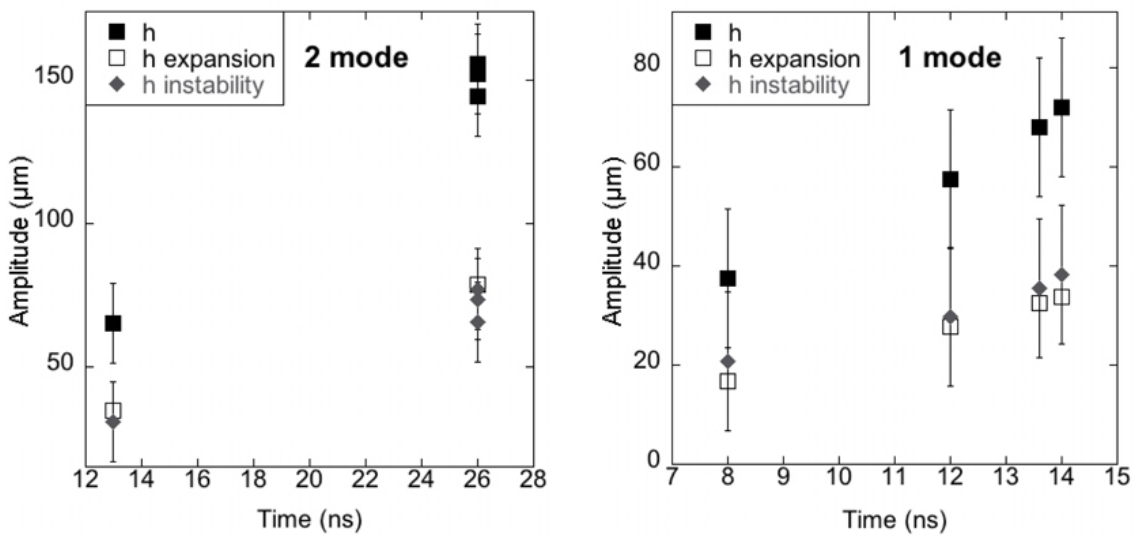

Figure 2.16: Plot of h, half the distance between the spike tip and bubble tip, h_{exp}, the amplitude due to expansion and h_{inst}, the amplitude due to the instability for a) 2-mode experiments and b) 1-mode experiments.

Dimonte (2000) points out that physically L in Equation 3.1 represents the ratio of volume to cross-sectional area of a single bubble or spike, since volume determines the net buoyant force while area determine the drag force. For self-similar multimode turbulence, L , is often related to the wavelength of the dominant bubble. In the present case, it makes more sense to approximate a single spike or bubble as a cylinder (or in the 2D perturbation case, a rectangular prism) so that L becomes the height of the cylinder. Thus, in our case L is the mix-layer amplitude. It does not depend on the distance between bubbles or spikes. The amplitude changes over time and the expansion corrected data, h_{inst}, was linearly fit to find how the mix-layer amplitude changes with time. This gave a value of $2.72t$ where 2.72 is the velocity of amplitude growth in μm ns^{-1} and t is time in ns, which was used as the length scale in Equation 3.1. Since the length scale is based only on the available experimental data this analysis is only valid for the time when the experiment was observed, in this case, up to 26 ns. One can see that the dynamical length scale has no dependence on the wavelength of the perturbation only on the amplitude. As all of the patterns have

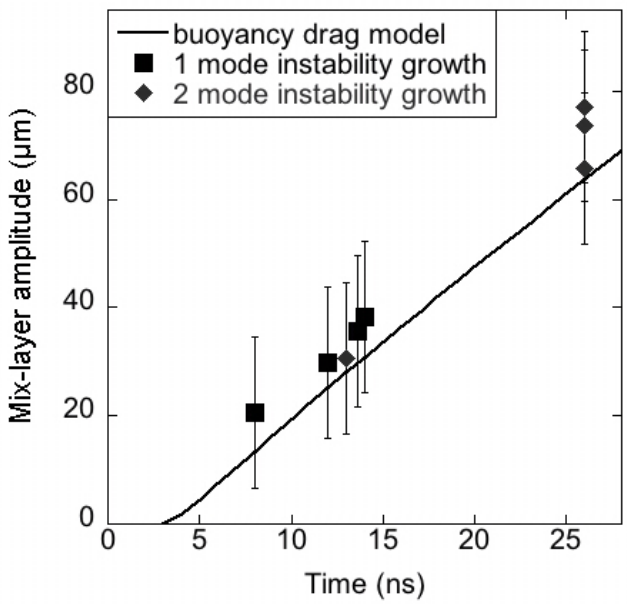

Figure 2.17: Plot of the amplitude vs. time for the single-mode and 2-mode experiments compared to the buoyancy-drag model.

the same amplitude this model predicts that they should all show the same mix-layer amplitude growth. Both the experiments and simulations have shown that the mix-layer amplitude is similar for all cases.

Integrating Equation 2.4 with respect to time and using results from the Hyades simulations for the initial condition one can solve for the amplitude of the mix layer. The theoretical value of the mix-layer amplitude vs. time is shown Figure 2.17 along with the inferred h_{inst} for the single and 2-mode type perturbation. The model and experiment are in overall good agreement with the model predicting slightly less growth, but agreeing within the error bars.

2.4 Conclusion

This chapter has shown experiments and simulations relevant to the hydrodynamic processes occurring in supernovae. Experiments, dominated by the Rayleigh-Taylor instability, show good agreement with simple, incompressible models. 2D FLASH

simulations over predict the shock position, most likely due to the EOS and lateral expansion; yet have similar results for the growth of the mix-layer as compared to the experiment. Further work is being done with FLASH to adjust the gamma of the foam and polyimide to more accurately predict the shock position. Supernova relevant experiments have progressed to experiments with 3D initial conditions, which is discussed in the next chapter.

CHAPTER III

3D blast-wave-driven Rayleigh-Taylor instability and the effects of long-wavelength modes

3.1 Introduction

This chapter describes experiments exploring the 3D Rayleigh-Taylor [60, 70] instability at a blast-wave-driven interface. This experiment, similar to the experiment described in Chapter II, is well-scaled to the He-H interface during the explosion phase of SN1987A [69]. In the experiments, $\sim$ 5 kJ of energy from the Omega [7, 6] laser was used to create a planar blast wave in a plastic disk which is accelerated into a lower-density foam. These circumstances induce the Richtmyer-Meshkov [65, 50] instability and, after the shock passes the interface, the system quickly becomes dominated by the Rayleigh-Taylor instability [67]. The plastic disk has an intentional pattern machined at the plastic/foam interface. This perturbation is 3D with a basic structure of two orthogonal sine waves with a wavelengths of 71 μm and amplitude of 2.5 μm. Additional long-wavelength modes with a wavelength of either 212 μm or 424 μm are added onto the single-mode pattern. The addition of the long-wavelength modes was motivated by the results of previous experiments [18] where material penetrated unexpectedly to the shock front, perhaps due to vorticity deposited at the interface when the shock front transited an unintended structure. The current ex-

periments and simulations were performed to explore the effects of this unintended structure, however, we were unable to reproduce the previous results [18].

As briefly described in Chapter I, supernova hydrodynamics experiments have moved towards experiments with more complex initial conditions, namely 3D initial conditions involving a designed perturbation of the interface by sinusoidal modulations of the same wavelength in two orthogonal directions. The paper describing these experiments, by Drake (2004) [18] (referred to as Paper I throughout the rest of the present chapter), reported the observation of anomalous penetration by the spikes from the blast-wave-driven Rayleigh-Taylor instability to the shock front. After these experiments were executed, an unintended structure, which will be described later in this chapter, was found in the experimental targets. The effect of this feature was to introduce a substantial long-wavelength component into the initial conditions for the instability. At the time, it was thought that perhaps this structure in the target caused the unexpected spike penetration. This result motivated the experiments and simulations described in the present paper, which systematically explore the effects of long-wavelength structure on the blast-wave driven instability.

3.2 Target Structure and Experimental Conditions

3.2.1 Target Structure

The key components of the targets are shown in Figure 3.1a and a completed target, which was assembled at University of Michigan, is shown in Figure 3.1b. This target is very similar to the target described in Chapter II, but there are subtle differences. There is a disk of plastic material followed by a layer of low-density foam. The plastic component and the foam are enclosed in a tube made of polyimide with nominally 25μm thick walls. The CRF foam has a density of nominally 50 mg cm^{-3} and is several mm long. This is different from the targets for the 2D experiments

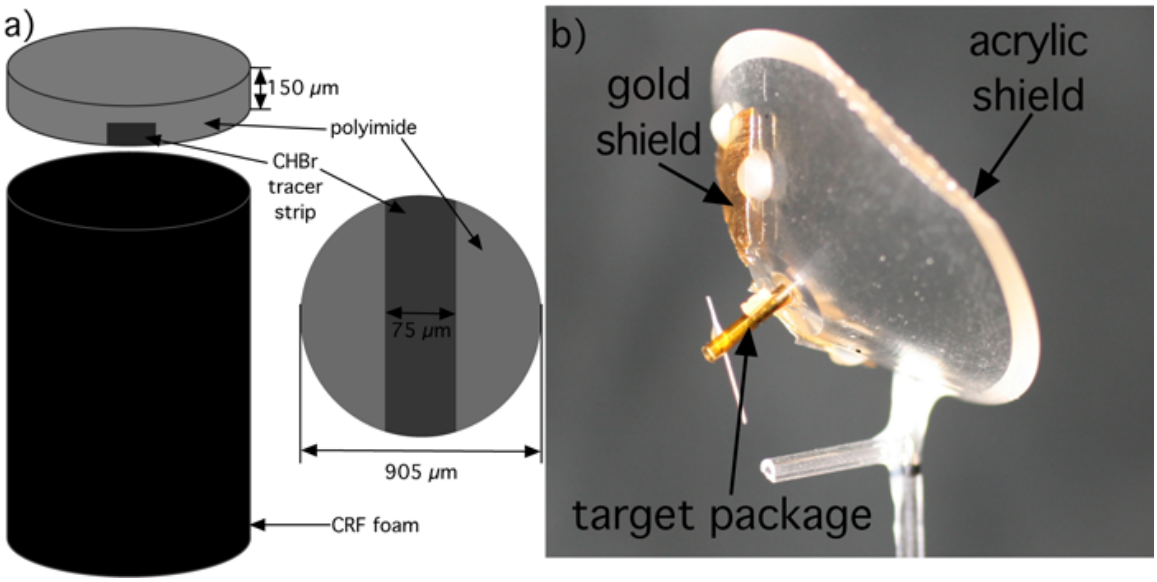

Figure 3.1: a) The main experimental target components. A polyimide disk is followed by a CRF foam. A slot is milled out of the polyimide and a bromine-doped plastic strip is glued into the slot. These pieces are enclosed in a polyimide shock tube. b) A completed target, fabricated at University of Michigan. The main components from a) are indicated by target package. The pictured target has an acrylic shield with gold wedges attached to it. In some cases, targets have an all gold shield.

described in Chapter II, which used similar foam with a density of 100 mg cm^{-3}. The plastic disk is composed mostly of polyimide, which has a chemical structure of $C_{22}H_{10}O_5N_2$ and a density of 1.41 g cm^{-3} (later determined to be 1.43 g $cm^{-}3$). It has a nominal diameter and thickness (individually measured) of 905 μm and 150 μm, respectively.

Similar to the 2D experiments, the plastic disk contained a diagnostic tracer strip made of CHBr. On the CHBr side of the plastic disk, a perturbation is machined to seed the instabilities. This perturbation was 3D and was similar to the one used in the experiments reported in Paper I. It was a single-mode pattern that was composed of two sine waves in orthogonal directions with an amplitude of 2.5 μm and wavelengths in each direction of 71 μm. An illustration of this 3D, single-mode pattern is seen in Figure 3.2a. After the experiments of Paper I were performed, it was discovered

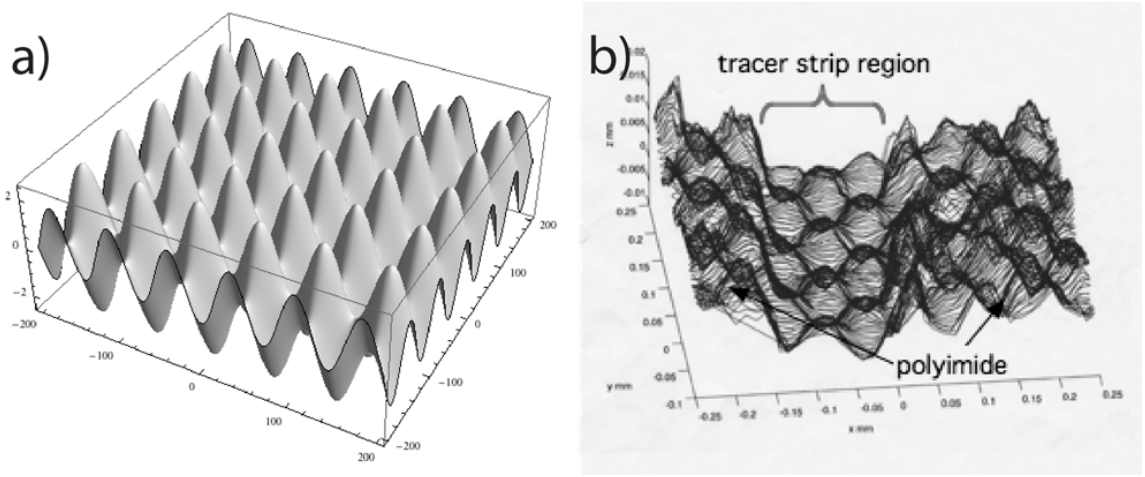

Figure 3.2: a) An illustration of a portion of the 3D, single-mode "egg crate" pattern defined as two orthogonal sine waves each having a wavelength of 71 μm and an amplitude of 2.5 μm. b) After a set of experiments, the CHBr material was found to be $\sim$ 5 μm lower than the surrounding material. This image shows the elevation, as measured by interferometry, of the surface of the plastic disk.

that the tracer strip was lower than the surrounding polyimide material. This is the unintended structure that was mentioned earlier. This depression was due to the machining process used to create the 3D pattern on the plastic piece. The tool cut more deeply into the CHBr material than the surrounding polyimide, causing the tracer strip to be $\sim$ 5 μm lower. This is indicated in Figure 3.2b, which shows the mean elevation for a portion of the plastic component. The center region in Figure 3.2b is the tracer strip; it is surrounded by polyimide. The tracer strip is clearly recessed compared to the than the neighboring material. Recall that the initial amplitude is 2.5 μm, thus, 5 μm is a large value on this scale.

It was thought that this tracer strip depression might have been the cause of the spike penetration to the shock front in the experiment described in Paper I. In a crude approximation, the depression could be thought of as an additional long-wavelength mode. This motivated the present experiments for which the initial conditions included an additional long-wavelength mode that was added to the 3D, single-mode

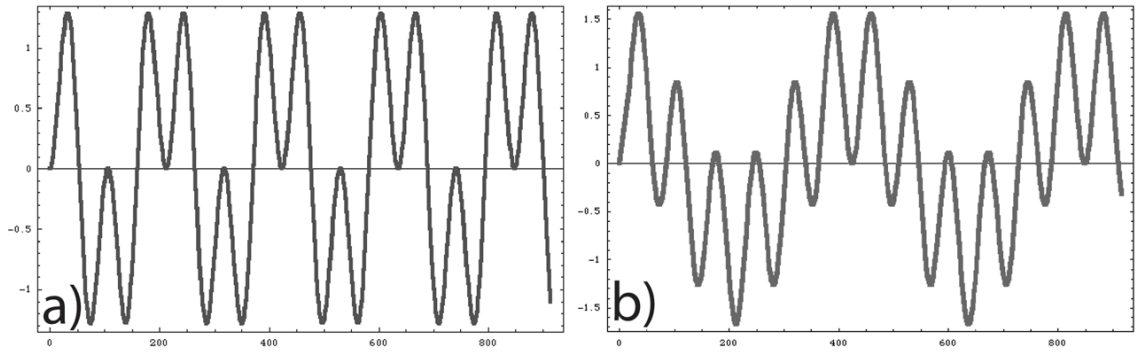

Figure 3.3: Plots of the additional sinusoidal mode that is added to the 3D, single-mode pattern in one direction. A plot of a mode with a) a 212 μm wavelength and b) a 424 μm wavelength. The overall amplitude of the 3D, 2-mode pattern is 2.5 μm, which is the same amplitude as the 3D, single-mode pattern.

pattern. Two multimode patterns were used in these experiments. In one direction a wavelength of either 212 μm or 424 μm was machined on top of the single-mode perturbation. Figure 3.3 shows each of the additional modes used in the present 3D, 2-mode experiment. For the current experiment the plastic component was fabricated and machined at General Atomics. After the discovery of the depressed tracer strip, General Atomics developed improved machining techniques to reduce the depression, which was approximately 0.1 μm for the present experiments.

It also became evident that characterization of the plastic disk was necessary prior to the experiment. Target specifications and tolerances are determined and each disk is characterized using an optical microscope, a white light interferometer, and a confocal scanning microscope for a variety of measurements. Some of the measurements made were disk diameter, disk thickness, CHBr width, CHBr thickness, surface depression, glue thickness, wavelength, and amplitude. For a plastic component to be used in the experiment these measurements must meet the predetermined specifications and tolerances. More information about the specifications and characterizations of the plastic disk is included in Appendix D.

3.2.2 Experimental conditions

The laser conditions of the 3D experiment are the same as those for the experiments detailed in Chapter II. However, the 3D experiments used a CRF foam with a density of 50 mg cm^{-3}, while the 2D experiments used a foam with a density of 100 mg cm^{-3}. This shock will move slightly faster in the lower density foam. The results from a Hyades [45] simulation are shown in Figure 3.4. The output of the simulation was taken at the same times as in Figure 2.5, which shows Hyades results from simulations performed with a foam density of 50 mg cm^{-3}. Again the shock has decayed to a blast wave by 2 ns and the shock and interface can be seen at 270 μm and 300 μm, respectively, at 4 ns. The main diagnostic for this experiments is ungated dual, orthogonal x-ray radiography, which is fully detailed in Appendix A.

In order to protect the ungated film from emission by the hot, glowing plasma created during the initial laser pulse, a large gold or acrylic conical shield is attached to the target. The shield is $\sim$ 20 mm at the largest opening and is tapered to $\sim$ 4 mm at the base of the shield. In the case when an acrylic shield was used, an additional gold wedge was also used on the outside of the shield on the side nearest the diagnostic. The acrylic shield with gold wedges can be seen in Figure 3.1. The plastic and foam components are enclosed in the polyimide shock tube labeled target package. In addition to the shield, a 50 μm thick gold washer coated in a thin layer of plastic was placed at the base the shield. This washer, which had a 2.5 mm outer diameter and a 1 mm inner diameter, was also used to protect the ungated diagnostic from plasma that could "leak" out between the shock tube and the gold or acrylic shield.

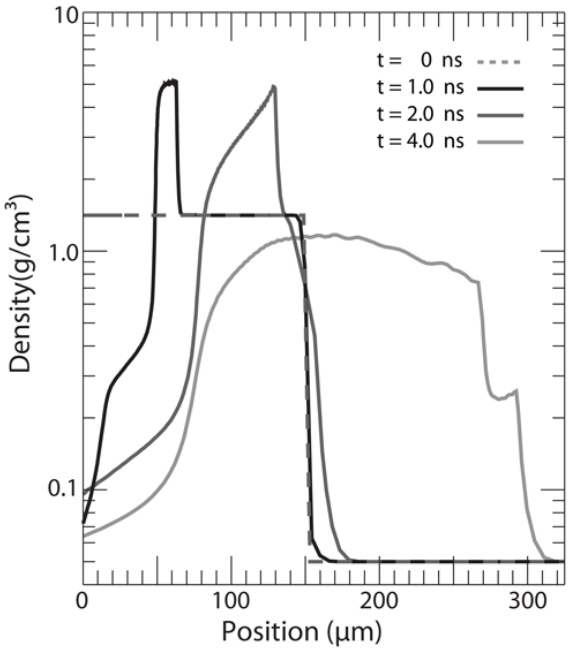

Figure 3.4: Density vs. position plot from a 1D Hyades simulation for the 3D experiment, which is similar to 2D experiment except that the foam has a lower density. The simulation results are shown at t = 0 ns, t = 1 ns, t = 2 ns, t = 4 ns.

3.3 Results

3.3.1 Experimental Results

Figure 3.5 shows data adapted from Paper I and is typical data from that experiment. In these images darker pixels indicate areas of higher density, in this case, the CHBr material. The bright area on the left of the image is low-density material flowing toward the reverse shock. Moving to the right in the image there is an alternating pattern of light and dark from the top to the bottom of the image. This is the interface that shows the mixing of the CHBr (dark) and foam (light) materials. The initial perturbation for this experiment was a 3D, single-mode pattern (see Figure 3.2a); it was imaged 17 ns after the initial laser pulse. Beyond the interface is the shock wave, which is moving to the right. There is a dark dot on the image that is a flaw on the detector and dark areas on the lower left and upper right regions of the

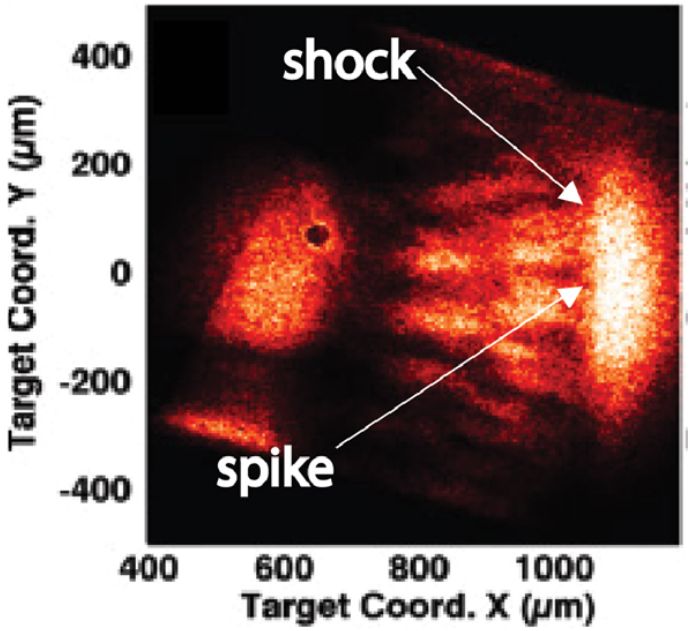

Figure 3.5: Data adapted from the Paper I [18]. The shock front and and the tip of a spike are labeled. The spikes clearly reach the shock.

image are regions of no signal on the detector. This image was not obtained with an ungated diagnostic as was mentioned above. It was created using an x-ray pinhole framing camera as is described in Paper I and in Chapter II. An important feature in these data is that the spikes have reached the shock front. This is the type of anomalous growth, mentioned previously, that motivated the present experiments.

Figure 3.6 shows radiographs from the present experiments, performed with 3D, 2-mode initial conditions. Figure 3.6a had an additional wavelength of 212 μm and Figures 3.6b and 3.6c have an additional wavelength of 424 μm. Figure 3.6a was taken at 17 ns after the drive pulse was initiated, while 3.6b and 3.6c were taken at 13 ns and 17 ns, respectively. The dark area on the left of the image in Figure 3.6a is the conical gold shield used to protect the diagnostic. There is a thin, curved, dark line on the lower left corner of the image. This is a wire attached to the shield of the target. There are also several dark spots on this image that is due to an accumulation of debris on the protective shield of the diagnostic. The edges of the polyimide tube walls can also be seen along the top and bottom of each image. There is a gold grid

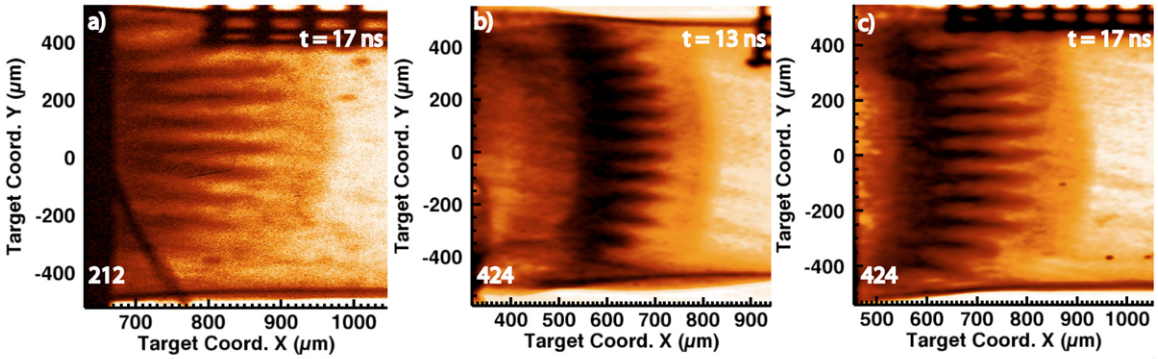

Figure 3.6: Data from more recent experiments with 3D, 2-mode initial conditions at a) t = 17 ns, b) t = 13 ns, and c) t = 17 ns. Results from experiments where the additional mode had a wavelength of a) 212 μm , b) 424 μm and c) 424 μm.

in the upper right of the images, which is used to measure the magnification and spatially calibrate the image for analysis. Again the spikes and bubbles are seen at the interface and beyond that to the right is the shock. In Figure 3.6b the edge of the reverse shock can be seen on the far left, followed by the interface and shock moving to the right. In the unshocked foam region in Figures 3.6a and 3.6b there are striations that are due to the filter used in experiment.

The grid in these images is measured prior to the experiment and is used to calibrate the position in the radiographic image. The initial position of x = 0 μm, y = 0 μm is the center of the plastic disk where the initial laser beams are also centered. Once an image is calibrated the positions of important features are found. The location of any feature, where feature refers to the spike-tip, bubble-tip or shock position, is found by taking a horizontal profile of varying width across the feature. An example of a horizontal profile across a single spike is shown in Figure 3.7a, which shows the pixel intensity vs. position and the corresponding radiograph is shown in Figure 3.7b. The black rectangle in Figure 3.7b indicates the size and position of the profile for the spike. The width of the profile depends on the size of the feature, in these images the width of the profile is 30 μm. In Figure 3.7a the pixel intensity

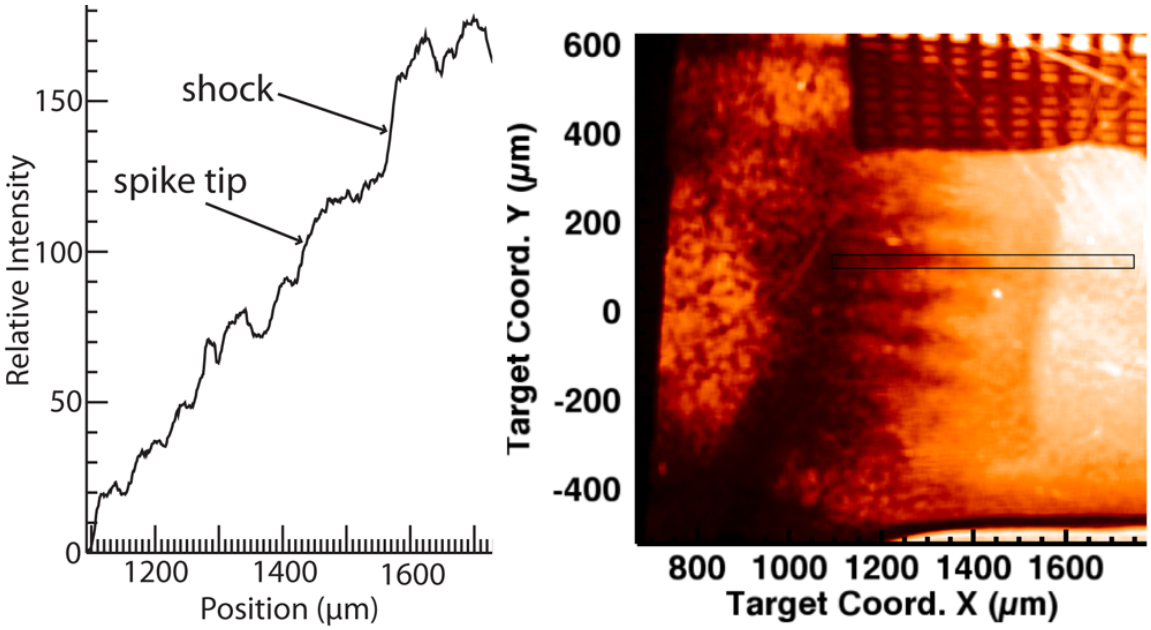

Figure 3.7: a) A 1D plot of pixel intensity vs. position for a spike averaged across the width of the respective rectangle seen in the b) radiograph.

varies across the position of the spike tip from 1427 μm to 1469 μm. The position of the spike tip is taken to be halfway between these two points. The bubble tip and shock position are found in similar ways. Ideally there would be a sharp change in intensity at the feature position, but this is spread out by a combination of finite source size, any tilt in the target, and perhaps variation in the areal density of CHBr. The gradient in the intensity is incorporated into the uncertainty of the measurement.

When calculating relative positions, such as the distance from the spike tip to the bubble tip or the spike tip to the shock front, the uncertainty mentioned above is the largest uncertainty in the measurement. The data from these experiments have better resolution and lower noise than the experiments of Paper I. There were also improvements in the quality of the data during the current set of experiments, from improvements such as switching to Agfa D7 film and decreasing the pinhole aperture. Due to these improvements later experiments had a relative error of $\pm$ 10 μm and earlier experiments had a relative error of $\pm$ 15 μm.

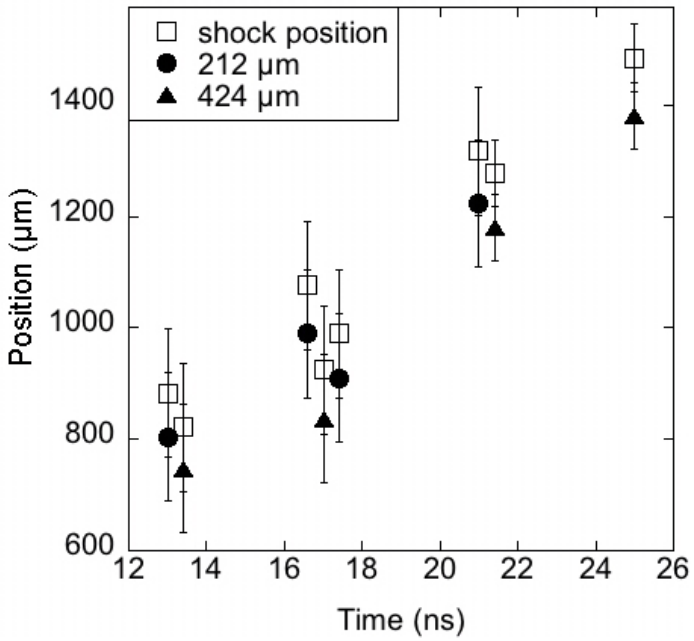

Figure 3.8: Spike-tip and shock positions vs. time for 3D, 2-mode initial conditions. Groups of points have been slightly offset in time.

Absolutely calibrated locations, such as those shown on the axes of Figures 3.5, 3.6 and 3.7b, have other sources of error that stem from the measurement and alignment of the target. First, the process to calibrate the data will be discussed. The location of the target grid is measured with respect to the center of the plastic disk (this is the point of laser irradiation and indicated as (0, 0)). The error associated with these measurements is $\pm$ 20 μm. During the experiment the target is aligned in the Omega chamber. There are two types of alignment, translational and rotational. The error associated with the former is about $\pm$ 20 μm. The error in rotational alignment varied over different experimental days as techniques for alignment have also improved. For earlier experimental days the error was as high as $\pm$ 60 μm and it was later reduced to $\pm$ 10 μm. The combined error in absolute positions is $\pm$ 115 μm for earlier experiments and $\pm$ 60 μm for later experiments.

The data from the most recent experiments have been analyzed using the methods described above and the results are shown as plots in Figures 3.8 and 3.9. Figure

3.8 shows the spike and shock position vs. time for both types of 3D, multimode experiments. Multiple data experiments were performed at 13, 17, and 21 ns. These clusters of data points have been offset in time to make the plot clearer. The spike-tip position is less than the shock position. The spikes do not reach the shock in these experiments, although the positions overlap within error, in contrast to the result in Paper I. This is also evident in the radiographs of this data, Figures 3.6a, 3.6b, 3.6c. Further evidence is seen in Figure 3.9a, which is a plot of the distance between the spike tip and the shock front vs. time. If the spikes had reached the shock front this value would be zero and clearly it is not. From these experiments it does not appear that a long-wavelength mode causes enhanced spike penetration seen in the previous experiments. Recall that the current experiments differed from the previous experiments. The previous experiment had a 3D, single-mode machined perturbation with a recessed tracer strip. The current experiment has a 3D, 2-mode machined perturbation, where the additional mode is a long-wavelength mode. This long-wavelength mode was intended to intentionaly reproduce the conditions of the previous experiment.

It is also of value to consider the mix-layer amplitude for the experimental data. The mix-layer amplitude is defined as half of the distance between the spike tip and the bubble tip. The mix-layer amplitude vs. time for experiments performed with both types of 2-mode initial conditions are shown in Figure 3.9b. Unfortunately, there is a limited amount of data for the 2-mode experiments performed with a supplemental 212 μm wavelength mode. However, notice that for both types of experiments the value of the mix-layer amplitude roughly fall on a straight line.

3.3.2 Simulation and Simulation Results

The results just described are puzzling in two ways. First, the previous interpretation of Paper I, that the result of the interaction of the blast wave with the

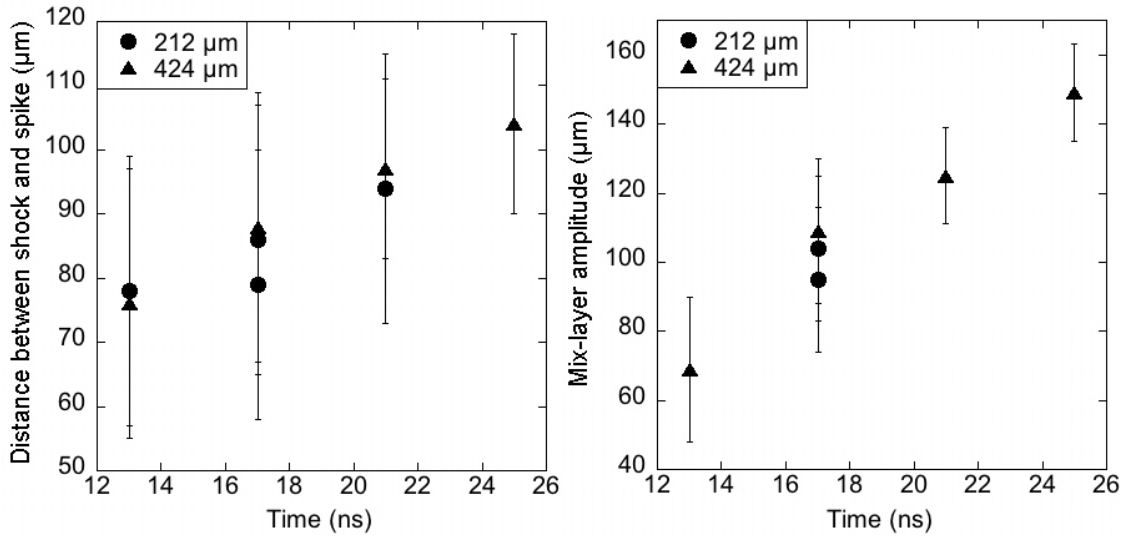

Figure 3.9: a) Distance between the spike tip and shock front vs. time for 3D, 2-mode initial conditions. b) Mix-layer amplitude, half the distance between a spike tip and bubble tip, vs. time for 3D, 2-mode initial conditions.

tracer strip was to deposit vorticity that pushed the spikes further forward, should apply as well to the interaction of the blast wave with the long-wavelength modes in the present experiments. Indeed, the spectral structure corresponding to the 212 μm mode in the present case is similar to that corresponding to the depressed tracer strip in the previous case. Second, this same reasoning would lead one to expect to observe a difference between the two cases here, with the longer-wavelength mode thrust further forward. To explore the underlying dynamics and to seek possible causes for the increased spike penetration in the experiments of Paper I, 3D simulations with the code FLASH were performed. These simulations specifically studied variations in the depression of the tracer strip.

A brief description of the FLASH code is given in Chapter II. These simulations were done in 3D Cartesian coordinates; the domain was a rectangular prism with dimensions of approximately 455 μm by 455 μm by 1635 μm. The resolution of the simulation was 1.42 μm per zone or 50 zones per wavelength. The initial seed perturbation was the 3D, single-mode pattern that was used in the experiments of

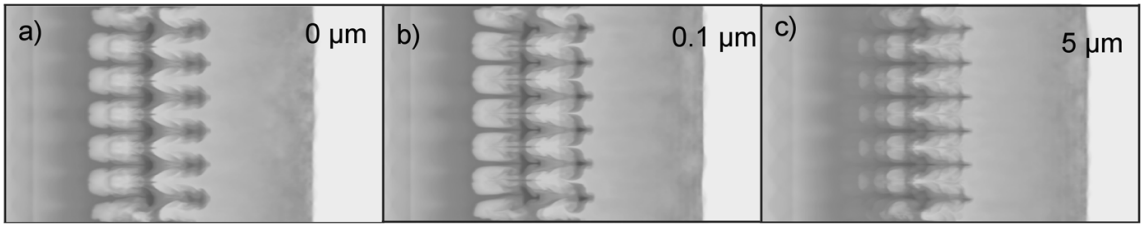

Figure 3.10: 3D FLASH simulations at t = 17 ns for various depressions of the tracer strip. a) no depression b) 0.1 μm depression and c) 5 μm depression.

Paper I and that provided the basic structure of the present experiments, along with varying degrees of depression of the tracer strip. The initial structure of the blast wave was provided by output from a 1D simulation of the laser-driven shock by the code Hyades.

The simulation results at t = 17 ns are shown in Figures 3.10 and 3.11. The color in these images is scaled so that the darkest areas are the densest, and are based on linear density. These images are an average over the center 230 μm of the domain. This corresponds to the location of the tracer strip and these averages best represent what would be seen in experimental radiographs like those discussed above. Three simulations were performed with varying depressions in the tracer strip. The nominal case is shown in Figure 3.10a and has no depression. Figure 3.10b, shows a simulation performed with the tracer strip depressed 0.1 μm with respect to the surrounding plastic. This simulation is representative of the amount of depression in more recent experiments, such as those of Figure 3.6. Figure 3.10c shows a simulation performed with tracer strip depressed 5 μm, which corresponds to the experiments of Paper I.

The nominal case, Figure 3.10a, and the 0.1 μm depression case, Figure 3.10b show few differences. The spikes, bubbles and shock are in roughly the same locations and the spikes and bubbles have relatively similar shapes. Simulations performed with a 5 μm depression, Figure 3.10c, show greater differences from the other cases. Again, the

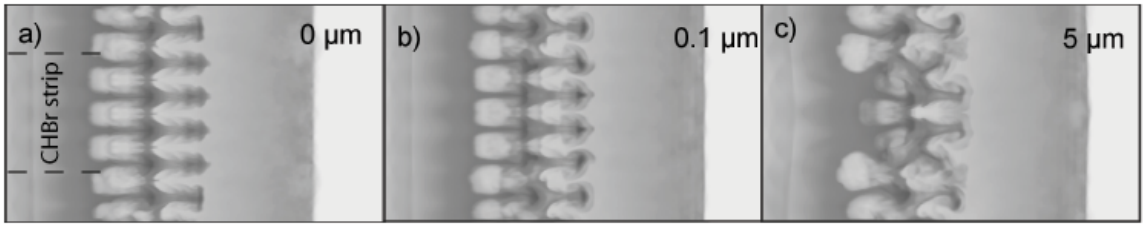

Figure 3.11: 3D FLASH simulations at a 90° view from the simulation in Figure 3.10.

locations of the spike, bubbles and shock are in the same relative positions, however, there are some qualitative differences in this simulation, specifically in the bubbles. The base of the bubbles appear to be more filled in than in the other cases. Overall, the results of these simulations are very similar. Also, it is important to note that while there are some small differences between these simulations, not one of these cases show the spikes moving much further than the others, let alone to the location of the shock front.

Figure 3.11 shows results of the same three simulations from an orthogonal point of view, so that the tracer strip occupies approximately three spikes in the center of the domain. Note that all of the experimental radiographs shown previously are not viewed from this angle. The relative position of the CHBr strip is shown in Figure 3.11a. As was true in the other view of the simulations, the nominal case and 0.1 μm case are very similar. The 5 μm case is very different from the other cases. The spikes are in similar locations compared to the other two cases, but the bubbles are very different. The center bubble tips are much farther ahead (to the right) of the neighboring bubbles tips. When comparing this figure to Figure 3.10c, which shows the view 90° from this one, it becomes apparent why the bubbles appear filled in in that figure. It is clear, from Figure 3.11c, that the 5 μm depression does affect the structure of the mix layer. Material at the tracer strip location is indeed thrown forward. But the spikes have already moved far enough to remain relatively unaffected as of the time of the measurements. Indeed, they might never be affected

because the acceleration decreases with time in these blast-wave-driven experiments, in contrast to the constant-acceleration case that has informed much past conceptual thinking about these problems. From these simulations it does not appear that the depression of the tracer strip is responsible for the increased spike penetration seen in the experiments of Paper I and it is not surprising that the present experiments gave the results they did.

3.4 Discussion

It is evident that in the case of experiments executed with 3D, 2-mode initial condition the spikes do not reach the shock front as was observed in Paper I. Nevertheless, it is important to understand the observed amount of instability growth. The buoyancy-drag model is an incompressible model for Rayleigh-Taylor mixing that describes the evolution of the mixing layer with respect to time as discussed in Chapter II. This description is similar to an equation of motion for each bubble or spike with an inertial term and a friction term. From Oron (2001) [57] and Dimonte (2000) [13] a 3D description of the growth of a given feature is as follows

$$(\rho_1 + C_a\rho_2)\,\frac{du}{dt} = (\rho_2 - \rho_1)\,g(t) - \frac{C_d}{L(t)}\rho_2 u^2 \tag{3.1}$$

where ρ_1 and ρ_2 refer to the high and low-density material, respectively, u is the instability velocity in μm ns^{-1}, and $g(t)$ is the acceleration of the interface in μm ns^{-2}. In Equation 3.1, C_a is the added mass coefficient and for the 3D buoyancy-drag model it is 1, while C_d, the drag coefficient, is equal to 2π in this case. $L(t)$ is the length scale of an individual feature and, as discussed in Dimonte (2000) and in Chapter II, it is equal to the ratio of the volume to the cross-sectional area. The volume determines the net buoyant force while the area determines the drag force. In this case, it is the mix-layer amplitude of the instability. Recall, that the mix-

layer amplitude for these experiments showed very similar growth for the two types of 2-mode experiments seen in Figure 3.9b. Also, both patterns had the same initial amplitude. The amplitude of the mix layer is increasing with respect to time and from the experimental data it is $3.39t$ where 3.39 is the velocity of the amplitude growth in μm ns^{-1} and the time, t, is in ns. In Equation 3.1, the ratio of ρ_1 to ρ_2 is 5.67 and g(t) = -6.4(t/3)$^{-1.1}$, which is found from a simulation. This equation can be integrated for the amplitude of the mixing layer.

In order to compare the data to this model, an expansion correction factor must be subtracted from the data. This is due to the fact that the buoyancy-drag model is incompressible and the experiment is compressible. A full description of correcting the data for the expansion that occurs in the experiment is contained in Chapter II. In both Chapter II and the present chapter the expansion accounts for roughly half of the mix-layer growth. Once the data has been corrected for decompression it can be compared to the 3D buoyancy-drag model, as shown in Figure 3.12. This figure shows the 3D Rayleigh-Taylor instability growth for the present experiments. Again, the two different types of initial conditions show similar growth. These results are compared to the results of the buoyancy-drag model represented by the black line. The data agree with the model within the error of the measurement.

3.5 Conclusions and Future Directions

In summary, the experiments and simulations described in this chapter were motivated by unexpected spike penetration observed in previous experiments. This penetration of the spikes all the way to the shock front was thought to be caused by the depressed tracer strip. The depression of the tracer strip was discovered after the experiments when the CHBr material was measured to be about 5 μm lower than the surrounding material. It was thought the depression behaved as an additional long-wavelength mode added to the intentional pattern. This motivated experiments

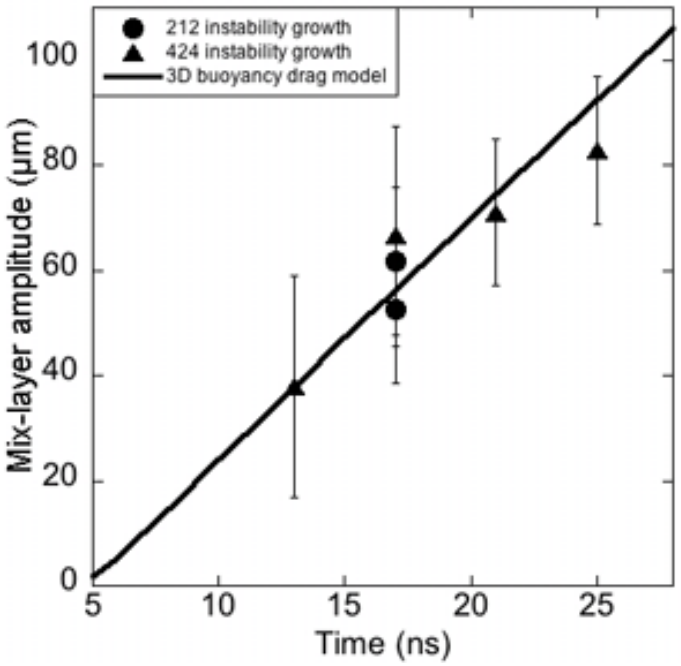

Figure 3.12: The 3D buoyancy-drag model compared to the instability growth from experiments having 3D, 2-mode initial conditions.

to explore this possibility.

The present experiments had 3D initial conditions similar to those of the previous experiments, but with the tracer strip depression replaced by long-wavelength modes in the pattern. There were two types of experiments, one where the additional mode was 212 μm and another where the additional mode was 424 μm. Both of these initial conditions had amplitudes of 2.5 μm. The results of these experiments indicated there to be no difference in the growth of the mix layer. Upon analysis of the 3D buoyancy-drag model this result is of no surprise since the ratio of volume to cross-sectional area for the features in these types of the experiments are proportional to the amplitude of the individual features in the mixing layer. In these experiments the initial amplitude of such features is the same and their subsequent growth is very similar. Neither of these experiments showed the spikes moving to the shock front. Therefore, the tracer strip behaving as a long-wavelength mode is not a cause for the unexpected growth seen in earlier experiments.

Three-dimensional simulations were also performed to investigate the consequences of a depressed tracer strip. The results showed that different amounts of depression produce some qualitative differences in the bubble structure; however, the overall position of the spikes was not affected by the depression of the tracer strip material. Also, none of the simulations showed the spikes reaching the shock front as was observed in the prior experiments. This phenomenon is further discussed in Chapter IV.

CHAPTER IV

Spike extensions in Rayleigh-Taylor instability experiments

4.1 Introduction

The laboratory experiments described in the present paper observe the blast-wave-driven Rayleigh-Taylor instability with 3D initial conditions. About 5 kJ of energy from the Omega laser creates conditions similar to those of the He-H interface during the explosion phase of a supernova. The experimental target is a 150-μm thick plastic disk followed by a low-density foam. The plastic piece has an embedded, 3D perturbation. The basic structure of the pattern is two orthogonal sine waves where each sine wave has an amplitude of 2.5 μm and a wavelength of 71 μm. In some experiments, an additional wavelength is added to explore the interaction of modes. In experiments with 3D initial conditions the spike morphology differs from what has been observed in other Rayleigh-Taylor [60, 70] experiments and simulations. Under certain conditions, experimental radiographs show some mass extending from the interface to the shock front. Current simulations show neither the spike morphology nor the spike penetration observed in the experiments. The amount of mass reaching the shock front is analyzed and potential causes for the spikes reaching the shock and the spike morphology are discussed. Our leading hypothesis is that these phenom-

ena may be caused by magnetic pressure, generated by an aziuthmal magnetic field produced by the plasma dynamics.

Such a magnetic field can be generated by the orthogonal components of the electron temperature and electron density gradients in the system. Our quantitative evaluation, for the specific case of interest, is that about 10 – 23% of the material in the spikes has been pulled ahead, with some material extending all the way to the forward shock. This previously unexamined process has the potential to transport small amounts of material over much greater distances than one would expect from previously observed mechanisms. We also discuss several other hypotheses regarding the origin of the unexpected spike morphology and penetration.

The first experiments using 3D structure (orthogonal sinusoidal modulations) at the unstable interface were reported by Drake (2004) [18] and typical data from the experiment is shown in Figure 3.5 on page 60. The data showed spikes due to the Rayleigh-Taylor instability protruding to the shock front, as was also observed in the experiments reported here. This depth of penetration was unexpected. It was initially thought to be due to the deposition of vorticity by the shock front as it crossed the tracer strip, which was depressed by 5 μm relative to the surrounding material. This hypothesis was tested with further 3D experiments that explored the effects of additional long-wavelength modes [39] in targets manufactured to more stringent specifications and more thoroughly characterized (see Appendix D). These experiments and related 3D simulations showed that the increased spike penetration was not caused by long-wavelength modes. Improvements in target precision, alignment precision, and diagnostic technique [37] led us to examine again the case of orthogonal sinusoidal modulations at the interface in the work reported here. The increased brightness and contrast of the images allow a much closer examination of the spike structure. The experimental conditions in this chapter are the same as those described in Chapter III. The target is also the same and is shown in Figure 3.1 on

page 55. The 3D, single-mode initial conditions are shown in Figure 3.2a on page 56. Some experiments were performed with supplemental modes, seen in Figure 3.3a and Figure 3.3b on page 57.

4.2 Radiographic images and the effects of initial conditions

Figure 4.1 shows a radiographic image from an experiment performed with a 3D, single-mode perturbation as the initial condition. The target was imaged at 21 ns after the initial laser pulse began. It is important to note several features in this image. The dark area on the left side of the image is the gold wedge that is attached to the acrylic shield. Also, there is a gold fiducial grid attached to the polyimide tube and visible in the upper right corner of the image. The shock front, which is moving to the right, is seen toward the right edge of the image. The darker regions near the center of the image are produced by x-ray absorption in the CHBr; their right boundaries show the now convoluted interface whose lateral extent defines the mixing layer. The spikes due to the instabilities are the dark fingers and consist of the dense plastic material. In between the spikes are the bubbles of foam. One interesting aspect of this image is the uniform thickness of the spikes. In Rayleigh-Taylor experiments, one would expect the tip of the spikes to become enlarged, forming "mushroom cap" also known as Kelvin-Helmholtz roll-ups. Another aspect of this image is the presence of elongated spikes that appear to reach the shock front. Neither of these results were expected, nor are they present in simulations of this experiment.

Note that one has a clear view of the central, curved section of the shock in the foam. The details of the shock are much more evident in these experiments than they were in previous data, due to the improved techniques described above. In particular, one can sometimes detect a Mach stem near the wall. However, there are also cases when, rather than a Mach stem, one sees a shock leaving the wall and interacting with the main shock, as is the case at the bottom wall in Figure 4.1 (and as would be

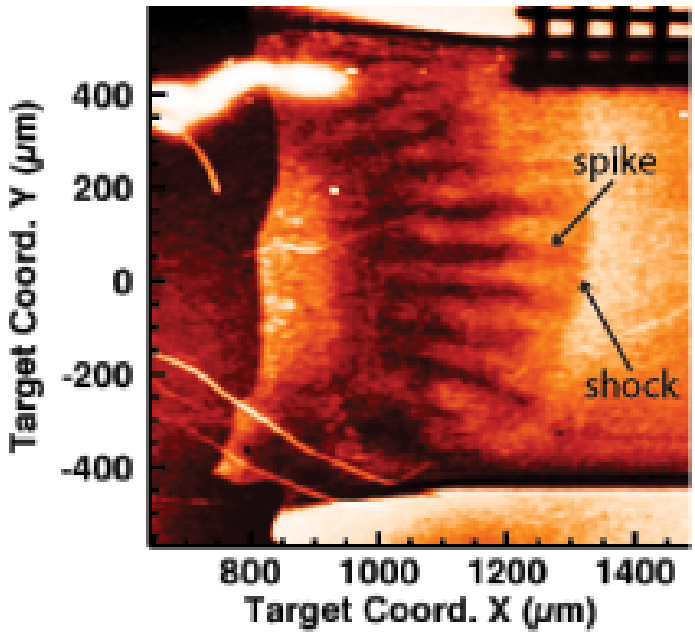

Figure 4.1: An x-ray radiographic image of an experiment that used a 3D, single-mode perturbation as the initial condition. This radiograph was imaged 21 ns after the initial laser pulse began. Labels indicate the position of the shock and a spike extending to the shock front.

more evident with different image enhancement). These "wall shocks" are discussed by Doss (submitted) [14]. While the Mach stems or wall shocks will interact with and affect the edges of the shock and interface, the center of the shock and ends of the spikes are clearly seen in Figure 4.1.

Evidence of material extending to the shock is further indicated by one-dimensional (1D) profiles from various locations in the image. Figure 4.2a is part of the radiographic image from Figure 4.1 and has labels indicating the location of the 1D profiles shown in Figures 4.2b and 4.2c. Figure 4.2b is a 1D, horizontal profile and the line marked A in Figure 4.2a represents its position. This profile, and subsequent 1D profiles, show pixel intensity vs. relative distance in μm. Pixel intensity is related to the areal mass density; this relation will be discussed later in this paper and in Appendix B. In Figure 4.2b, the positions of the shock and spike are labeled. Note that the area to the left of the shock shows an increase in intensity indicating that

mass is present up to the shock front. This region corresponds to elongated spike that reaches the shock in Figure 4.1 and will be referred to as a spike extension. Note in Figure 4.2b that the area referred to as the spike extension is small in length, 32 μm in this case, compared to the rest of the mix layer.

Evidence of spike extensions from a single-mode experiment reaching the shock is also seen in Figure 4.2c. These are 1D, vertical profiles at different locations indicated by the regions labeled B and C, respectively, in Figure 4.2a. The line labeled B is a profile at roughly the middle of the mixing layer. The peaks in the intensity indicate a bubble and the valleys indicate a spike. The line labeled C is a profile taken 20 μm from the shock position. It was taken at this location because this is the variation in the shock position due to the resolution in the image as well as the curvature of the shock front. Again, there are variations in the intensity and the positions of lowest intensity in line C correspond to the positions of lowest intensity in line B. Except for the centermost spike and the corresponding extension, the spike extensions are slightly to the right or to the left of the center of each spike. This is due to the curvature of the interface that can be noted in Figure 4.1 and in Figure 4.2a. The vertical, 1D profiles are only perpendicular to the center spike and the spikes on either side curve slightly in opposite directions. This alignment or near alignment of the lowest intensities in these two profiles indicates that there is mass that is aligned only with the spikes within 20 μm of the shock. Also, note that in line C the peak-to-valley amplitude of the variation in intensity is smaller than in line B. This is because there is less density at the tips of the spikes. This is also observed in the radiographic image and in the 1D, horizontal profile shown in Figure 4.2b, where the pixel intensity increases across the spike and therefore its areal mass density decreases. While only one example of spike extensions is shown in detail here, these extensions have been observed in several, similar experiments and in every case for which the performance of the experiment and the instrumentation would permit it.

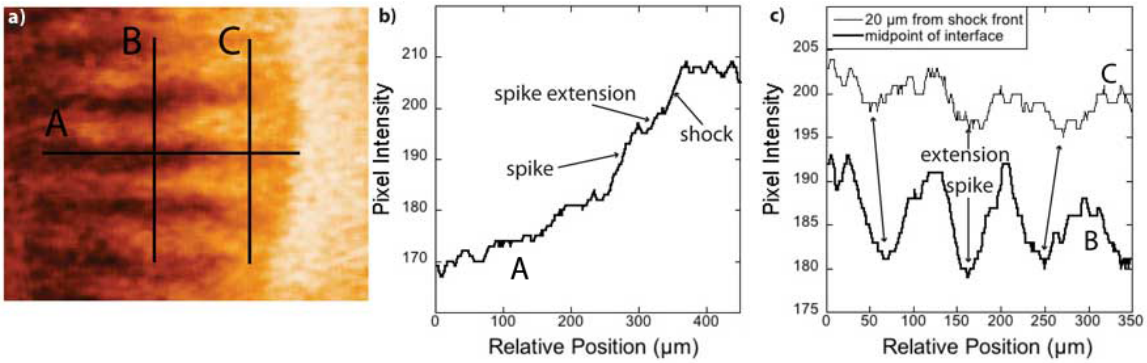

Figure 4.2: (a) Part of the radiographic image from Figure 4.1 with labels indicating the location of (b) a horizontal, 1D profile and (c) two vertical, 1D profiles taken at the midpoint of the spike, labeled line B, and 20 μm from the shock front, line C.

Similar analysis was performed on an experiment performed with 3D, 2-mode initial conditions. For this experiment the additional mode had a wavelength of 424 μm. A radiographic image of this 2-mode experiment is shown in Figure 4.3, which was imaged at 25 ns from the initial laser pulse. While this time is slightly later than the time of observation in of the single-mode experiment shown in Figure 4.1, the experimental conditions are very similar for both experiments. The spikes in the 2-mode experiment do not appear to be reaching the shock, in contrast to the single-mode experiment shown in Figure 4.1. 1D profiles were also taken from this image in locations similar to those labeled in Figure 4.2a. Figure 4.4a shows a horizontal profile from region A; it does not show an increase in intensity before the shock. Figure 4.4b shows two vertical profiles from approximately mid-interface, line B, and 20 μm from the shock, line C. The profile labeled C has fluctuations that probably result from Poisson noise due to the limited number of x-ray photons [37]. These fluctuations are not large compared to Figure 4.2c, line C and there is no correlation between the spikes, the lowest intensities, in line B and the lowest intensities in line C for the experiment performed with 2-mode initial conditions. The profile labeled C corresponds to the area between the spike and shock in Figure 4.3 where the spike

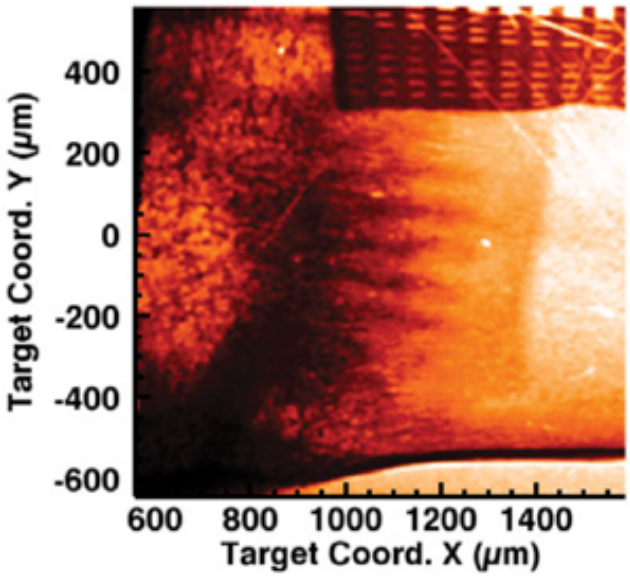

Figure 4.3: An experimental radiograph imaged at t = 25 ns. This experiment was performed with 3D, 2-mode initial conditions where the additional mode was 424 μm.

does not appear to be extending to the shock. In addition to the experiment with 3D, 2-mode initial conditions shown here, 10 other experiments were performed with similar conditions and none of these experiments showed evidence of spike extensions.

We emphasize that, excluding the feature we have labeled as a spike extension in Figure 4.2b, the shape of the spike structure seen in Figures 4.2b and 4.4a is very similar. These shapes are also similar to those seen in numerous other experiments. The qualitative difference in the shape of the horizontal profile, combined with the fact that these features reach the shock, led us to designate them as distinct elements of the structure.

In an additional 3D, 2-mode experiment the structure was observed at 21 ns. The image was calibrated and the relevant positions were measured. The mix-layer width is defined as the distance between the bubble-tip and the spike-tip. For the single-mode experiments the mix-layer width was 224 $\pm$ 15 μm, which does not include the 32 μm long spike extension. The mix-layer width of the 2-mode experiment was 255 $\pm$

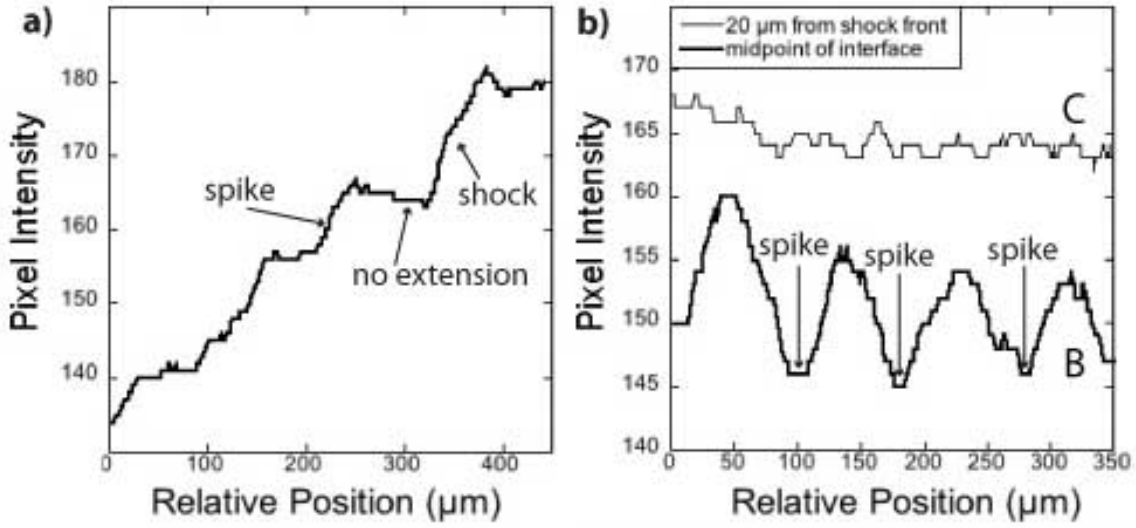

Figure 4.4: Several 1D profiles were taken in locations similar to the locations labeled in Figure 4.2a. (a) A horizontal, 1D profile taken along a single spike and (b) two vertical, 1D profiles taken at the midpoint of the spike, line B, and 20 μm from the shock front, labeled line C.

15 μm . The amplitude of the mix-layer due to instability growth is about one fourth of the total mix-layer width so the two experiments show similar instability growth. The instability growth of these experiments is further discussed in Kuranz (2009) [42]. The main difference between these two experiments is the distances between the dense plastic material and the shock front. In the 2-mode case the spike tip is 108 $\pm$ 15 μm from the shock front, while in the single-mode experiment the spike extension is 7 $\pm$ 15 μm from the shock front.

It is possible that the spikes produced in experiments performed with targets having 3D, 2-mode interfaces may also have some amount of mass moving to the shock, but there is a lower limit of mass that can be detected in these images. This limit will be discussed later in this paper. It is of great interest to measure the amount of mass that is transported to the shock in images where spike extensions are present.

4.3 Evaluation of mass in spikes

A method for calculating the amount of mass and the error in the mass in the spikes and spike extensions has been adapted from Hansen (2007) [25]. In an x-ray image, the x-ray attenuation due to mass absorption can be expressed as,

$$I = \sum_{\nu} I_{0,\nu} \prod_{i} e^{-\mu_i(\nu) m_i / A} + I_b, \tag{4.1}$$

where I is the measured intensity in the image at a pixel of interest (proportional to the number of x-ray photons incident on the pixel). The parameter $I_{0,\nu}$ is the unattenuated intensity at frequency ν incident on the pixel of interest, the subscript i designates a given material along the line of sight. Also, μ_i is the x-ray mass attenuation coefficient at frequency ν, m_i is the mass along the line of sight within the area of one pixel of a material i, A is the area of the pixel, and I_b is the background intensity in the image. This equation is summed over all x-ray frequencies, ν, and the product is taken over all materials, i, along the line of sight. In order to estimate the amount of mass in the spike and the spike extensions, the above equation must be simplified. First, the backlighter material, Sc, is assumed to have a monochromatic spectrum. The He-α line dominates the Sc spectrum as seen in Figure 4.5 and it accounts for 50% of the emission from the metal. The He-β and He-γ lines will be further discussed in the error analysis section of this paper. Also, there are up to 4 materials that intercept the x-rays from the x-ray source in the diagnostic view: the polyimide tube wall, the polyimide target layer, the CHBr target layer, and the CRF foam. The absorption of the CRF foam is negligible and will be ignored here. Including these assumptions, the above equation becomes

$$I = I_1^* T_{PI,\alpha} T_{CHBr,\alpha} + I_b, \tag{4.2}$$

where $T_{i,\alpha} = e^{-\mu_i(\alpha)m_i/A}$, where i refers to the material, and α refers the He-α emission line. In the above equation, note that the sum of the unattenuated intensities, $\sum_\nu I_{0,\nu}$, has been replaced by I_1^* , where includes attenuation from other materials. This is because I_0 is a measured value from the x-ray radiograph and cannot be divided into the separate x-ray frequencies. The transmission through the polyimide tube wall, $T_{wall,\alpha} = e^{-\mu_{wall}(\alpha)\rho_{wall}x}$, is assumed to be constant so that ρ_{wall} is the initial polyimide density, 1.43 g cm^{-3}, and x is the polyimide wall thickness at the center of the tube for both the front and back of the tube, which is 50 μm. The transmission through the polyimide wall is included in the I_1^* factor. Also, along the line of sight in the diagnostic view, near the center of the tube, there are about 13 spikes of material. Three of those spikes are CHBr and the other ten are polyimide. Including the ratio of CHBr to polyimide in Equation 4.2 and solving for m_{CHBr} yields,

$$m_{CHBr} = -\frac{A}{\frac{10}{3}\mu_{PI,\alpha}\mu_{CHBr,\alpha}} ln\left(\frac{I - I_b}{I_1^*}\right). \tag{4.3}$$

Equation 4.3 can be used to quantify the amount of mass in a spike in the center of the radiographic image seen in Figure 4.1a. This can be done by calculating the mass of each pixel in the spike and then summing all the masses for the total spike mass.

The image seen in Figure 4.1 is further processed to remove a background feature present in the image. This process is explained fully in Kuranz (2009) [41]. In order to estimate how much mass is in a spike or spike extension, one must use Equation 4.3 to find the mass in each pixel in the spike or extension. The value of the unattenuated pixel intensity, would be determined outside of the polyimide shock tube where there are no target components. However, since the foam has little attenuation by the Sc x-ray source and I_1^* is a combination of I_0 and T_{wall}, the value of I_1^* is found by taking an average of pixels in the unshocked foam region. Also, the background intensity, I_b, must be subtracted from this value. The value of I_b, which originates

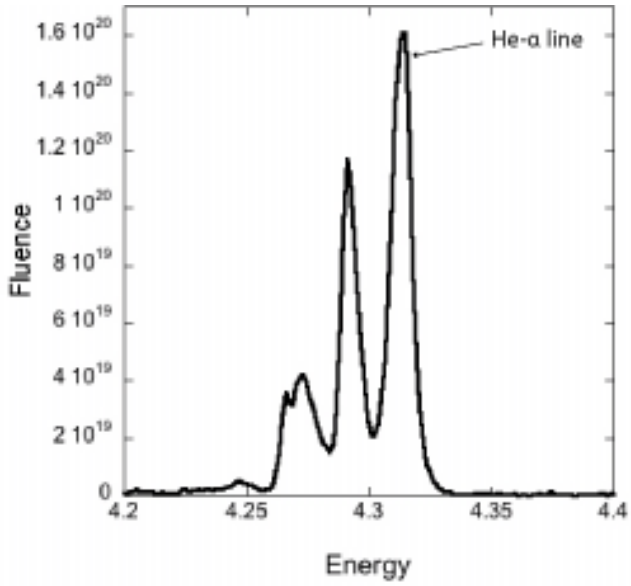

Figure 4.5: The spectrum of the backlighter material, Scandium. This plot shows fluence vs. energy. The three large peaks correspond to the He-α, He-β and He-γ x-rays lines.

from unattenuated high-energy x-rays or x-rays scattered within the diagnostic and is correspondingly uniform across the portions of the image of interest, is measured behind the large acrylic and gold shield.

The uncertainty of these mass measurements is due to the uncertainty in our measurement as well as to the assumptions in the model. In Equation 4.3, μ_{PI}, μ_{CHBr} and A are constants. The values of I_1^* and I_b are measured and therefore have some statistical error associated with them. The value of I is the single value of a single pixel and does not have any statistical error. The mass-attenuation coefficient μ is weakly dependent on x-ray energy, so we treat the corresponding small impact on the intensity as though there is a random error in μ. (If this effect were larger, one could obtain a more accurate result using an iterative calculation that accounted explicitly for the x-ray spectrum.) The error due to the approximation that the backlighter source is monochromatic can be represented by

$$\delta I_\mu^2 = \sum_\nu \left(\left[\frac{dI}{d\mu_{CHBr}(\nu)} \delta\mu_{CHBr}(\mu) \right]^2 + \left[\frac{dI}{d\mu_{PI}(\nu)} \delta\mu_{PI}(\mu) \right]^2 \right) \tag{4.4}$$

where $\delta\mu_i(\nu) = |\mu_i(\nu) - \mu_i|$. The above value is less than or equal to

$$\sum_{\nu} \left(\frac{I_0^*}{A} max(m_{CHBr}) T_{wall} e^{-\left(\frac{10}{3}\mu_{PI}(\nu) + \mu_{CHBr}(\nu)\right)\frac{max(m_{CHBr})}{A}} \right)^2 \left([\delta\mu_{CHBr}(\nu)]^2 + \left[\frac{10}{3}\delta\mu_{PI}(\nu) \right]^2 \right), \tag{4.5}$$

where $max(m_i)$ is the maximum mass of material i, which would be the initial mass of either the CHBr. The value of δI_{mu} adds in quadrature to the statistical error of I_1^*. Combining the above with a standard error calculation, the mean-square error in the mass becomes

$$\delta m_{CHBr}^2 = \left(\frac{\partial m_{CHBr}}{\partial I_1^*} \right)^2 \left((\delta I_1^*)^2 + \delta I_\mu^2 \right) + \left(\frac{\partial m_{CHBr}}{\partial I_b} \delta I_b \right)^2 \tag{4.6a}$$

$$= \left(\frac{A}{\frac{10}{3}\mu_{PI} + \mu_{CHBr}} \right)^2 \left(\frac{(\delta I_1^*)^2 + \delta I_\mu^2}{(I_1^*)^2} + \frac{\delta I_b^2}{(I - I_b)^2} \right). \tag{4.6b}$$

Therefore, the mean-square error in the total spike mass, from the N pixels of a spike, becomes

$$= \left(\frac{A}{\frac{10}{3}\mu_{PI} + \mu_{CHBr}} \right)^2 \left(N \frac{(\delta I_1^*)^2 + \delta I_\mu^2}{(I_1^*)^2} + \delta I_b^2 \sum_{p=1}^{N} \frac{1}{(I_p - I_b)^2} \right), \tag{4.7}$$

where I_p is the value of the intensity of a single pixel of the N total pixels.

Herein, a spike was defined as the pixels inside of an area that was centered on the spike with the base aligned with the neighboring bubble tip and including all the pixels up to the shock front. Due to the thickness of the tracer strip this is actually the attenuation through 3 spikes and the corresponding extensions. The width of the rectangle was defined by the full width at half maximum of the sinusoidal shape seen in Figure 4.1. The mass of the pixels in the rectangle are summed to find the total spike mass. The total spike mass is listed for several spikes and the corresponding spike extensions from different shots in Table 4.1. Images of these experimental radiographs and further experimental details are shown in Appendix F.

Shot #	spike mass (ng)	error (ng)	extension mass (ng)	error (ng)	% mass in in extension
45756	232	90	53	14	23%
	279	79	39	15	11%
	272	99	38	14	14%
41878	–	–	29	17	–
	–	–	28	16	–
	–	–	28	14	–
40932	154	44	27	6	18%
	175	41	24	6	14%
	180	42	18	9	10%
45754	265	96	42	9	16%
	240	79	38	7	16%
	224	70	31	7	14%

Table 4.1: The amount of mass in a spike and its spike extension for several 3D, single-mode experiments. The Shot # refers to an individual experiment. The error associated with each of these values is also listed.

The mass of spikes ranges from 154 ng to 279 ng with an error up to ± 99 ng. Shot number 45754 corresponds to the radiograph seen in Figure 4.1. The mass of the spike extensions was determined in similar way to the total spike mass. The base of the area defining the spike extension was located at the start of the spike extension, which is labeled in Figure 4.2b. The area extended all the way to the shock front, as did the area defining the total spike. The mass of several spike extensions is listed in Table 4.1. The mass of spike extensions ranges from 18 ng to 53 ng with errors ranging from ± 6 ng to ± 17 ng. This corresponds to 10 – 23% of the spike mass being in the spike extensions. Shot number 41878 only has the mass of the spike extension and not the total spike mass listed. This is because the entire spike was not visible in the experimental radiograph, however, the entire spike extension was observed.

The errors are listed for the total spike mass and the spike extension. The error listed includes the value of the error discussed previously, but also includes another, more prominent, source of error. This additional error is caused by the uncertainty

in the location of the position of the spike-tip, bubble-tip, shock front and base of the spike extension. These locations are typically known within 20 μm, but this uncertainty in position can alter the estimated mass in a spike between 18% and 59% in certain cases. The error listed in Table 1 is the total error in the total spike mass or spike extension. We used the 3D, single-mode pattern extensively while developing the experimental techniques that produced the data discussed here and in Kuranz (2009) [39] Of 13 experiments with this pattern, 9 were failures (4 were compromised by issues with target or backlighter construction, 4 were misaligned so that individual Rayleigh-Taylor spikes were undetectable, and 1 produced a radiograph with insufficient contrast for analysis). All four successful experiments with this pattern produced observable spike extensions and are listed in Table 4.1.

4.4 3D Simulation Results

Simulations of the experimental setup were performed using 3D FLASH. The FLASH multidimensional hydrodynamics code is used to model general compressible flows. This code uses the Piecewise-Parabolic Method [12] to solve the Euler equations. It allows for adaptive mesh refinement, placing resolution elements only in areas where refinement is needed [55]. The simulations were performed using 3D Cartesian geometry. The domain of the simulation was a rectangular prism with dimensions of approximately 1200 μm by 1200 μm by 2400 μm. The cylindrical target is embedded in this volume with a polyimide tube of inner radius 450 μm and outer radius of 475 μm. The simulation volume has reflective boundaries parallel to (but outside) the tube and an outflowing boundary at the tube end. The resolution of the simulation was $\sim$ 1.17 μm per zone or 60 zones per wavelength. A gamma law equation of state model was used with the polytropic gamma defined as 1.5 for the plastic and 1.4 for the foam, which is appropriate for the partially ionized media in this case [15]. FLASH is unable to model the deposition of the laser beams onto the

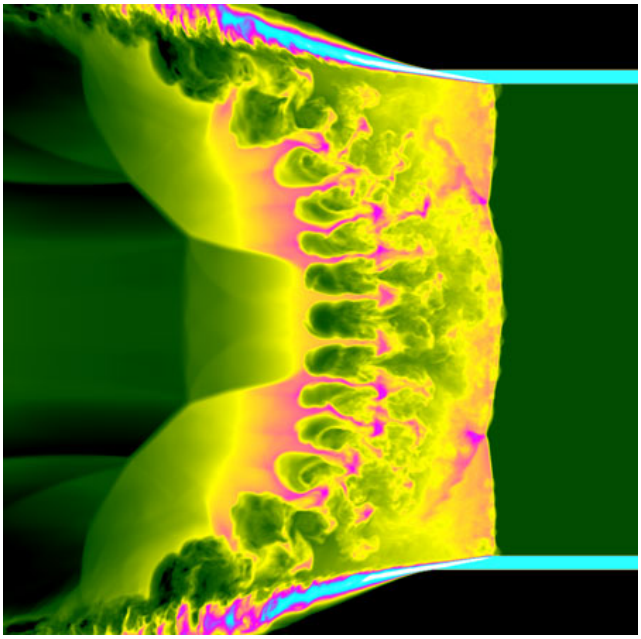

Figure 4.6: a) The results from a 3D FLASH simulation with 3D, single-mode initial conditions also at t = 21 ns. Note that no material has reached the shock.

target. The 2D, hydrodynamics code Hyades [45] contains a laser package and was used to define initial conditions for the FLASH code.

The results from 3D FLASH simulations are shown in Figure 4.6, which is a density plot at 21 ns after the initial laser pulse. This is the same time of observation as the experimental radiograph in Figure 4.1. The simulation results shown in Figure 4.6 was created by averaging over 71 μm in the center of the domain, which is one wavelength.

In the simulation output, the tips of the spikes and the midpoints of the spike are thickened due to Kelvin-Helmholtz effects. It is common in hydrodynamic simulations for the tip of the Rayleigh-Taylor spike to exhibit this kind of roll-up [29, 53, 52]. The roll-up in the midpoint of the spike is due to the three-dimensionality of the initial conditions where there is a saddle between neighboring spikes. This saddle is not as deep as the valley that will become a bubble. This can be seen in schematic of the initial conditions in Figure 3.2a on 56. These roll-up effects are not observed in results from experiments performed with 3D, single-mode or 3D, 2-mode initial

conditions as the spikes appear to have uniform thickness over their entire length, and whose width is approximately three resolution elements. This is seen in Figure 4.1, an experimental radiograph of a 3D, single-mode experiment, and in Figure 4.3, an experimental radiograph of a 3D, 2-mode experiment. However, the roll-up at the spike tips has been observed in previous experiments and FLASH simulations with 2D, single-mode and multi-mode initial conditions, both of which are further detailed in Kuranz (2009) [42]. For the case with 2D initial conditions, the simulation results showed a greater amount of roll-up than the experiment. In both 2D and 3D FLASH simulation results, more Kelvin-Helmholtz roll-up was observed in the spikes than compared to experiments performed with the corresponding initial conditions.

The spikes in Figure 4.6 are not of uniform thickness, whereas, the thickness of a single spike in the experimental radiograph is roughly the same along the length of that spike. The experiment does average over three spikes, which might contribute to the more uniform spke structure in the data. In the analysis of the simulation and experimental results, the mix-layer width is defined as the spike-tip position minus the bubble-tip position. In the 3D FLASH simulation, the mix-layer width is 250 $\pm$ 10 μm. As noted previously the mix-layer width in the single-mode experiment is 224 $\pm$ 15 μm. In the experiment, mix-layer width is similar at 256 $\pm$ 15 μm. While the experiment and simulation results show similar instability growth, their spike morphology differs.

In the 3D FLASH simulation results shown in Figure 4.6 the shock can be seen to the right of the interface. The spikes clearly do not reach the shock, but the shock structure and position need to be further addressed. The interaction of the shock with the tube wall creates a mach stem, which is seen on the edges of the shock front along the tube wall. The mach stem is not seen in the experimental radiograph shown in Figure 4.1 and is not generally seen in other, similar experimental radiographs. Instead a wall shock is observed, which seems to overtake the mach stem. In addition,

even in the absence of a wall shock, any Mach stem that may be present in the data is much smaller in radial extent than those seen in Figure 4.6.

It should also be noted that the shock position from the radiograph in Figure 4.1 and the simulation results differ by 179 μm. The experimental shock position from the experiment shown in Figure 4.1 is 1321 $\pm$ 60 μm and the simulated shock position is 1500 $\pm$ 20 μm. Since the error is much larger in the experiment, it is useful to consider several experiments observed at 21 ns performed under similar conditions. The range of shock positions for 7 experiments was 1175 μm to 1322 μm and the average shock position for these experiments was 1289 μm with an average error of 76 μm. This differs from the simulated shock position by 211 μm. The difference in shock position between the experiment and simulation is likely due to the fact that the simulation uses a constant gamma for the EOS of the foam. Miles (2004) found that adjusting the gamma of the foam had an effect on the shock position, but only a small effect on the interface position [52]. Also, the 2D Hyades simulation used to initiate the laser conditions used the full laser irradiance, but did not account for the reduced pressure that would arise from the laser beams irradiated the target at an angle. This resulted in an increase in the pressure due to the laser pulse, which in turn caused the shock speed in the simulation to be greater than in the experiment.

4.5 Discussion

Two aspects of the observation differ significantly from simulations, in ways that are not understood. One of these is the absence of enlarged structures on the spikes. Mushroom caps have been observed in all simulations of these and previous experiments performed over many years with several codes. Re-examination of previous, 2D data reveals that the mushroom caps appear to be smaller in those data that in the simulations of them, and also that the details of the mushroom caps are sensitive to the models used in the simulations.

The other difference between experimental and simulated spikes is the observed extension of spikes to the shock front, which has motivated a number of experiments. Initial experiments that showed spikes penetrating to the shock front were presented in Drake (2004) [18]. After the experiments were performed, it was discovered that the CHBr tracer strip was $\sim$5 μm lower than the surrounding polyimide material. This is a large depression considering that the initial amplitude of the perturbation is 2.5 μm. It was first thought that the vorticity deposited by the shock in passing over the depressed tracer strip had caused the spikes to reach the shock front. However, the present, subsequent experiments with a negligible tracer-strip depression still observed spike material penetrating to the shock front, experiments using a long-wavelength mode as a surrogate for the tracer strip did not, and 3D simulations to explore the impact of the tracer strip also found that the depression in the tracer strip did not produce increased spike penetration. We review these elements next.

Additional experiments were performed using long-wavelength modes as a surrogate for the depression of the tracer strip, discussed both in Kuranz (2009) [39] and above. These experiments showed no evidence of the spikes penetrating to the shock front. FLASH simulations performed with 3D, single-mode initial conditions with and without a depressed tracer layer found that there was not a significant difference in the growth of the mix layer or in the spike-tip position, and that the spikes did not reach the shock front. Therefore, it does not appear that the depressed tracer strip, or a long-wavelength mode, will cause the spikes to protrude to the shock front. Further simulations that consider the depressed tracer strip with 2D Hyades initial conditions and shock tube wall effects might be of value in understanding the detailed structure. The experiments in the present paper had 3D, single-mode initial conditions and the tracer strip was specified and measured to be 0.1 μm or less. Spike extensions were observed in the present experiment.

A second aspect of the target was identified as a potential cause of the spike

extensions. The CHBr tracer strip fits into a slot that is milled into the polyimide. If there were a gap between the CHBr and the polyimide, material could potentially jet through the gap. The specification of the gap is detailed in Appendix A. The gap is minimized and well characterized for each polyimide/CHBr piece. Furthermore, an additional diagnostic view confirms that material is not jetting through the gap between the CHBr and polyimide.

A third hypothetical cause of the spikes extensions was the acoustic flow within the system. A shock crossing a rippled interface also becomes rippled and then oscillates. This creates an acoustic structure behind the shock. It was possible that these sound waves might remove mass from the spikes and carry it forward to the shock. Simulations using FLASH with tracer particles show this is most likely not the case, as the flow patterns do not act to waft material forward.

A fourth possible mechanism that could cause spike material to penetrate farther than expected and that also could affect the spike-tip morphology, is turbulent mass stripping. This is the turbulent transfer of material from the spike to the surrounding flow [25]. In certain cases, material has been shown to be stripped at a rate that is significantly larger than that predicted by a laminar model. This model is fully described in the paper by Hansen (2007) [25]. It describes an experiment that models the crushing of a small dense region by a blast wave that is passing through an interstellar cloud. In the mass-stripping model the stripped, dense material is carried away by the flow of the lower density material. Simple models of mass stripping do not seem to explain the flow seen in the present experiment, but more complex models remain to be explored. If, for example, material were entrained in the shock as it crossed the interface, by some as yet unknown mechanism, then this could potentially explain the observed penetration. Also, if the spikes did develop roll-up at the tips of the spike and then another shock crossed the interface it could carry material forward to the primary shock. We know of no reason why a second shock would be present

in the experiment.

Another possibility is that a magnetic field wraps around the spikes, laterally confining them and resisting the expansion at the tip and midpoint of the spike as observed in the experiment. This magnetic pressure from the field may potentially exert pressure on individual spikes and squeeze material forward. Alternatively, the reduced drag on the narrower spike tips formed in the presence of the magnetic field might allow them to extend to the shock. Thus, in the abstract, the presence of the magnetic field might affect both spike length and the spike-tip morphology.

The known magnetic-field generation mechanism that is relevant here is the Biermann battery effect [3]. We also note that the origin of some recently observed magnetic fields in high-energy density plasmas remains unexplained [47, 68]. The battery effect is simply derived as follows. In these types of plasmas a magnetic field occurs when orthogonal components of ∇n_e and ∇T_e, where n_e is the electron density and T_e is the electron temperature, generate an electric field with finite curl. Ignoring electron inertia and the impact of any pre-existing magnetic field (zero here), an electric field is produced to balance the electron pressure,

$$\mathbf{E} = -\frac{1}{en_e}\nabla p_e \tag{4.8}$$

where e is the electric charge and p_e is the electron pressure. Using Faradays law in cgs units,

$$\frac{1}{c}\frac{\partial \mathbf{B}}{\partial t} = -\nabla \times \mathbf{E} \tag{4.9}$$

where $\mathbf{B}$ is the magnetic field and c is the speed of light. Inserting Equation 4.8 into Equation 4.9 we have

$$\frac{\partial \mathbf{B}}{\partial t} = \frac{ck_B}{e}\left[\nabla T_e \times \nabla \ln n_e\right], \tag{4.10}$$

where k_B is the Boltzmann constant. The electron density increases along the spike (or bubble) in the direction of shock propagation and it also increases in the spike-

to-bubble direction. The electron temperature also increases in the spike-to bubble direction, but it decreases along the spike. (or bubble). Due to the cross product in Equation 4.10, orthogonal pairs of these components will generate a magnetic field that wraps around a spike or bubble.

An estimate of the potential magnetic field magnitude shows that this possibility deserves further examination. We can approximate one component of the magnetic field generated around a spike using 1D simulations from Hyades to estimate the electron temperature and electron density variations. At 21 ns, the time of observation of the image in Figure 4.1, the electron density changes by about 10 eV in 300 μm in the plastic material (used as a surrogate for the spike). The value of $\nabla \ln n_e$ is taken to be in units of $1/\mu$m and therefore only the length scale of n_e is needed. Thermal conductivity dominates this length scale, which is defined as $\sqrt{\chi t}$, where χ is the thermal diffusivity for electrons in cm^2 s^{-1} for electron heat conduction from the hotter foam material to the plastic material and t is the time. At t = 21 ns we find the thermal conduction length scale to be 1.3 μm. These parameters correspond to a magnetic field generation at a rate of $\sim$ 2 x 10^{14} Gauss s^{-1}. After about 20 ns, the magnetic field generated would be $\sim$ 5 MGauss, in the absence of dissipation. The direction of the magnetic field would be azimuthal, so that it would wrap around the spikes and bubbles. The magnetic field would generate a magnetic pressure, $\frac{B^2}{8\pi}$, on the spikes or bubbles. The magnetic pressure would be about 10^{12} dynes cm^{-2}. This is similar to the plasma pressure at this time which is approximately ρu_s^2, where ρ is the density of the foam and u_s is the shock speed. Using the average shock speed from the experiment the plasma pressure is $\sim 10^{12}$ dynes cm^{-2} in the shocked foam. A pressure some orders of magnitude smaller than this might prove sufficient to resist the lateral expansion of the spikes, which is much slower. This estimate shows that magnetic pressure might be important. However, a full magnetohydrodynamic treatment of the system, including dissipation and plasma heating (which strongly

affects resistivity), must be considered to assess this hypothesis. However, one can conclude from the above estimation that the magnetic field and magnetic pressure may be large enough to have an effect on the system.

The FLASH simulation shown in Figure 4.6 does not include affects from magnetic fields. The lateral confinement of the spikes due to the magnetic field might potentially be responsible for the qualitative differences between the simulation results and the experimental results, specifically the thickness of the spikes. It was discussed previously in the present paper that Kelvin-Helmholtz roll-up of the spikes was more prevalent in FLASH simulation results performed with either 2D or 3D initial conditions. The magnetic pressure could prevent the spikes from expanding laterally, producing spikes of more uniform thickness. The magnetic field in experiments with 2D initial conditions would form in sheets rather than wrapping around individual spikes. This would create a weaker magnetic field. Recall that the 2D experiment showed some roll-up at the tip of the spike, but again, less roll-up than was observed in 2D FLASH simulations.

If the magnetic field is causing the spike extensions and affecting spike morphology, then it is of interest to estimate the magnetic field in SN1987A. Even though the temperature in the SN is much higher, the large distances over which the electron temperature and electron density vary cause the rate of magnetic field generation to be very small. According to the paper by Ryutov (1999) [69] the temperature scale is 900 eV but varies over 9 x 10^{11} cm as compared to 250 μm for the laboratory experiments. The time scale of the SN is also quite large, 2000 s compared to 20 ns in the laboratory experiment. For these values, the implied magnetic field remains small, $\sim$ 7 x 10^{-1} Gauss. This generates a magnetic pressure of about 10^{-1} dynes cm^{-2} while the plasma pressure in the supernova is 6 x 10^{11} dynes cm^{-2}. Therefore, it is unlikely that a magnetic field produced by the Biermann battery effect is affecting the fluid flow in a SN1987A.

This discussion of magnetic field generation raises the question of why the extensions are not observed in experiments using 3D, 2-mode initial conditions. Presumably, the parameters discussed previously to estimate the magnetic pressure are very similar in both types of experiments. Spike extensions could certainly be present in the case of 2-mode initial conditions, but our current diagnostic may be unable to detect them. While the mass of the spike extensions is estimated, it is the vertical variation in intensity so close to the shock that allows the spike extensions to be detected. The variation in pixel intensity from a spike to bubble at the midpoint of the interface is about 10 – 12 in units of pixel intensity. In Figure 4.2c the variation in pixel intensity across a spike extension is about 6, while the variation due to noise in Figure 4.4b is about 2 – 3. A variation of this size would correspond to a variation of 2 x 10^{-3} ng per pixel. The typical spike extension is about 35 pixels wide and 60 pixels long or about 38 μm wide and 66 μm long. This would correspond to a variation in mass of about 5 ng as a detectable mass limit. If there are spike extensions in the 2-mode experiments then their mass is probably less than 5 ng. This may indicate that the magnetic pressure is somewhat less in the 2-mode case than in the single-mode case. This might reflect that more complicated, less symmetric structures develop in the 2-mode case. Even so, in the 2-mode case one does not see the spike tip structure predicted by the simulations, and the above discussion shows that self-generated magnetic fields deserve close examination as a potential explanation of this difference.

4.6 Conclusions

In summary, we have observed the deep penetration of material beyond what is predicted for the Rayleigh-Taylor instability and narrow spike structure without broadened features, unlike that seen in simulations. This has been detected in several experiments with a 3D, single-mode pattern machined onto the experimental inter-

face. The amount of mass in the spike extension is about 10 – 23% of the total spike mass. Neither the spike penetration nor the spike-tip morphology have been detected in 3D FLASH simulations. It is possible that magnetic pressure from magnetic fields wrapping around individual spikes confines them, producing a more uniform thickness than those seen in simulation results. The magnetic pressure may also be involved in the extension the spikes to the shock front. It may turn out that magnetic-field generation must be included in simulations in order to explain this spike penetration and the difference in spike morphology.

Further experiments need to be performed in order to test the magnetic-field hypothesis and any others that may arise. Experiments can explore different amplitudes for 3D, sinusoidal perturbation to study the effects this has on the amount of mass flowing to the shock front. The magnetic field generated can be measured and compared to predicted values. Other laser experiments [68] have measured magnetic fields of 0.6 MGauss. The magnetic field of both the 3D, single-mode and 3D, 2-mode perturbations should be measured and compared since spike extensions are detected in only the 3D, single-mode experiments.

CHAPTER V

Conclusions and Future Directions

5.1 Conclusion

This thesis has presented experiments and simulations relevant to hydrodynamic processes believed to occur in core-collapse supernovae, specifically SN1987A. Heavy elements were observed earlier than predicted in the case of SN1987A. In order to reproduce the light curve from this supernova, models distributed some heavy elements, that were created in the core, halfway to the star's surface. This suggests that these elements were not concentrated at the core, as previously thought, but mixed into the envelope of gas. It is possible that this was caused by large-scale hydrodynamic mixing. This theory led to the experiments and simulations in this thesis that study the effects of blast-wave-driven hydrodynamic instabilities relevant to SN1987A.

My role in this work included performing the majority of the 3D experiments presented in this thesis. This involved designing the experimental targets and creating the specification and characterization requirements of the plastic/CHBr disks, which are detailed in Appendix D. Also, I performed the characterization on the completed targets, which is necessary to calibrate the resulting x-ray radiographic images. I was key in developing the new diagnostic technique discussed in Appendix A. This technique improved the quality of experimental radiographic images. I was also responsible for the execution of the experiment at the Omega laser facility. This

included specifying the laser and diagnostic conditions needed in the experiment. These specifications are shown in Appendix E. After the experiment, the data must be calibrated and analyzed. A sample of the calibrated data collected for this thesis is shown in Appendix F and two data analysis techniques are detailed in Appendix B and Appendix C. These data were then compared to a Rayleigh-Taylor model for mixing in Chapter II and Chapter III, and the mass of certain structures was estimated in Chapter IV. I also performed 1D and 2D simulations. The 2D simulations are shown in Chapter II. I guided an undergraduate student in the execution of the 3D simulations shown in Chapters III and IV.

While supernova hydrodynamics experiments on high-energy lasers have been in progress for 12 years, the first experiments detailed in this thesis are experiments performed on the Omega laser with 2D initial conditions. Three different initial conditions, all 2D, were studied. A single-mode, 2-mode and 8-mode pattern were used. Some targets included a flat, or planar interface to study the motion of the mean interface. The patterns were machined onto the polyimide/CHBr disk, which was followed by a low-density foam. These experiments used the Omega laser to create a ~ 50 Mbar shock in the plastic/CHBr disk. The shock quickly decayed into a blast wave while it was still in the plastic. The blast wave crossed the interface where the density drops, inducing hydrodynamic instabilities. At the times the experiment was observed, it was dominated by the Rayleigh-Taylor instability.

Supernova hydrodynamics experiments progressed to include more complicated initial conditions. This included 3D initial conditions. The first 3D experiments were performed with a 3D, single-mode perturbation and the experimental results showed further than expected spike penetration. After the experiment, an unintended target structure was discovered; the CHBr tracer strip was depressed by 5 μm relative to the surrounding polyimide. Recall that the initial amplitude of the machined pattern was 2.5 μm. It was initially thought that the deposition of vorticity by the shock

crossing the depressed tracer strip was the cause of the unexpected spike penetration. Further experiments were needed to study the effects of the depressed tracer strip. It was also clear that target characterization as well as the quality of the radiographic images needed to be improved.

The primary diagnostic for the experiments in this thesis was x-ray radiography. Until this point, area backlighting with a gated, x-ray pinhole framing camera was used. It was found that using a pinhole backlighter with ungated x-ray film was a superior technique. This lead to x-ray radiographic images with improved contrast and resolution. In experiments where the pinhole aperture was decreased, the resolution was further increased. The demonstration of this technique was further complicated by the use of dual, orthogonal radiography. Signal from a neighboring backlighter can fog the film, deteriorating the data. Despite these potential difficulties, this technique proved successful for this experiment and other, similar, experiments.

After the discovery of the recessed tracer strip, it was clear that more stringent specifications for the plastic disks were needed. It was also evident that more thorough characterization was needed prior to the experiment. While this thesis thoroughly discussed the recession or step height of the tracer strip, there are many other specifications to consider, each of them is discussed thoroughly in Appendix D. Each individual plastic disk was characterized before the experiment.

With the improvements in radiographic images and target fabrication, supplemental experiments were performed to investigate the increased spike penetration observed in the initial experiments with 3D, single-mode perturbations. In these experiments, the recession was approximated by a long-wavelength mode added to the basic 3D, single-mode pattern. The additional mode was added in one direction and had a wavelength of 212 μm or 424 μm. 3D, 2-mode experiments did not show the spikes moving to the shock front as the initial 3D experiments did, therefore, long-wavelength modes are not responsible for this phenomenon.

Additional experiments were executed with 3D initial conditions. These experiments used a 3D, single-mode pattern. This is the same perturbation as the initial, 3D experiments, however, due to improved machining techniques the tracer strip depression was about 0.1 μm instead of 5 μm. Resulting radiographic images showed the spike extending to the shock front, similar to what was observed in previous 3D, single mode experiments. Through mass estimation of the radiographic image it was found the 10 – 23 % of the spike mass was in the spike extension. The leading hypothesis for the cause of the spike extensions is that magnetic pressure, generated by an azimuthal magnetic field produced by plasma dynamics, reduces the spreading of the spike tip, decreasing the drag and allowing the spike to penetrate forward more rapidly.

2D and 3D hydrodynamic simulations of the experiments were performed using the FLASH code. I performed 2D simulations with 2D single-mode, 2-mode and 8-mode initial conditions were analyzed and compared to the experiment. The growth of the mix-layer for the simulation results and the experiment agreed within error. The shock position from the simulation results was further from the initial irradiated surface than the experimental shock position. This is most likely due to an unsatisfactory EOS in the foam and the lack of lateral expansion in the simulation.

I assisted an undergraduate student who performed 3D simulations with 3D, single-mode initial conditions. Supplemental 3D simulations were performed to study the effects of the tracer strip depression. The strip was recessed 0.1 μm and 5 μm relative to the surrounding polyimide material. Simulation results showed that the tracer strip depression had small but definite qualitative effects on the detailed structure of the mix layer. However, the tracer strip depression did not affect the overall growth of the mix layer. The simulated shock position from 3D FLASH was again larger than the experimental shock position, as was the case with 2D FLASH. In all of these simulations, the spikes did not reach the shock.

The results from experiments performed with 2D and 3D initial conditions were compared to the buoyancy-drag model for Rayleigh-Taylor growth. In order to compare the experimental results to this incompressible model, the data must be corrected for mix-layer growth due to material expansion. It is also important that the length scale of the model, L, is correctly interpreted. L is defined as the ratio of the volume to the cross-sectional area of a single spike or bubble. In these experiments, this is the mix-layer amplitude. Since the overall, initial amplitude of all of the experiments in this thesis is 2.5 μm, it is understandable that they would have the same mixed layer growth. The 2D and 3D experiments showed good agreement with the respective 2D and 3D buoyancy-drag models.

5.2 Future Directions

I have performed (but not included here) supernova hydrodynamics experiments with more realistic initial conditions. The hydrodynamics of the pre-supernova interior has been modeled by our collaborators using stellar evolution codes. An interface distortion at the convective boundary layer is used as a model for the experimental target interface. The simulated pre-supernova interface contained over 10,000 modes and was not feasible to machine. The number of modes was reduced to 51 modes while keeping the slope of the power spectrum the same as that of the original interface. These experiments were successful, but the results have yet to be analyzed.

Further experiments and simulations need to be performed to investigate the cause of the spike extensions seen in the 3D, single mode experiments. The results of 3D, resistive MHD simulations should be compared to the estimates of magnetic pressure for the experiment given in this thesis. Experimentally, the strength of the magnetic field can be measured. These measurements should be made on 3D, single-mode experiments and 3D, 2-mode experiments. Further thinking about why spike extensions have not been observed in experiments with 3D, 2-mode initial conditions should be

done. Experiments with a larger initial amplitude, which should show increased mix-layer growth, according to buoyancy-drag model, are currently being prepared. As mentioned earlier, the EOS in the foam is not well understood. Additional hydrodynamics experiments can be executed with different types and densities of foam. Further hydrodynamic simulations can also explore variations in the foam EOS.

APPENDICES

APPENDIX A

Diagnosing the instability: Dual, orthogonal backlit pinhole radiography

A.1 Introduction

Backlit pinhole radiography used with ungated film as a detector creates x-ray radiographs with increased resolution and contrast. In some cases, the hydrodynamics experiments described in this thesis use a 3D sinusoidal pattern as a seed perturbation for the study of instabilities. The structure of this perturbation makes it highly desirable to obtain two simultaneous, orthogonal backlighting views. We accomplished this using two backlit pinholes each mounted 12 mm from the target. The pinholes, of varying size and shape, were centered on 5 mm square foils of 50 μm thick Ta. The backlighting is by He-α emission from a 500 μm square Ti or Sc foil mounted 500 μm from the Ta on a plastic substrate. Four laser beams overfill the metal foil, so that the expanding plastic provides radial tamping of the expanding metal plasma. The resulting x-rays pass through the target onto (ungated) Direct Exposure Film (DEF) which is loaded into an Static Pinhole Camera Array (SPCA). In some cases, another x-ray film, Agfa D7, is used [44] in the experiments described

in this thesis. Interference between the two views is reduced by using a nose cone in front of the film, typically with a 9 mm Ta aperture and with magnets to deflect electrons. Comparison of varying types of pinholes and film exposures will be presented from recent experiments as well as an analysis of the background noise created using this experimental technique.

Backlit-pinhole radiography [46, 56, 8, 74, 5, 75] is a technique in which laser irradiation produces x-ray emission from an area of a target, after which a pinhole directs a small diverging beam of x-rays through the object to be imaged and onto a detector. This technique, under development for a number of years [62, 21, 4], provides a higher intrinsic brightness than a traditional pinhole box camera, permitting increased magnification and improved resolution. In principal, one can minimize the noise by detecting the x-rays with film when a gated detector is not required. This requires, however, that the film be shielded at all times from all other sources of emission at energies above about 1 keV. In recent years, techniques to accomplish this have been developed [21].

A natural extension of this technique is to obtain such data on the same experiment simultaneously along two orthogonal lines of sight. Such dual, orthogonal, backlit-pinhole radiography is an essential tool in diagnosing 3D structure in hydrodynamics experiments [18, 39]. The experiments described in Chapter III and Chapter IV consist of a 3D sinusoidal perturbation having orthogonal rows of peaks and valleys that is shown in Figure 3.2a on page 56. Obtaining two such images is significantly more difficult than backlit-pinhole radiography in only one direction, because of crosstalk created by signals from the laser-produced plasmas that emit the diagnostic x-rays. To our knowledge, our team is the first to have successfully obtained physics data simultaneously in two orthogonal directions by this technique. The present appendix discusses how this was accomplished.

A.2 The Experimental Design

The experiments each involved three targets. The main target was the hydrodynamics target with 3D initial conditions described in Chapters III and IV. The other two targets were backlit pinhole targets. A diagram of the pinhole structure can be seen in Figure A.1. The front surface consists of a 5 mm square foil of Ta with a pinhole in the center. The purpose of this large foil is to shield the diagnostic from emission from the hot plasma created by the laser beams that irradiate the rear surface of the structure. Five hundred microns behind the pinhole is a 3 mm square CH foil attached to the Ta by plastic spacers on each side of the CH. Attached to the rear surface of the plastic square is a 500 μm square metal foil. Laser beams irradiate the foil and the surrounding plastic, creating metal plasma, plastic plasma, and the desired Ti or Sc He-α x-rays of energies 4.51 or 4.09 keV, respectively.

The plastic foil serves three purposes. First, it provides plastic plasma that flows outward with the metal plasma [27] and tamps the radial motion of this plasma. This has proven essential to avoid the exposure of the film by x-rays from the metal plasma, seen around the edges of the Ta shield. Second, as the pressure from the laser-irradiated foil drives a shock through the plastic, this distributes the momentum and energy delivered to the metal foil over a larger mass of material, reducing the tendency to create shrapnel when this material strikes the Ta. Third, the plastic can be expected to absorb most of the energetic electrons produced by laser-plasma interactions in the metal plasma. Even so, experience has shown that the irradiance of the metal foil cannot exceed a few times 10^{14} W cm^{-2} without creating greatly increased noise. This particular experiment uses both Ti and Sc foils because the opacity of the target structures of interest is different along the two lines of sight.

The pinhole in the Ta serves as a filter, only allowing x-rays pointing directly at the target to pass through. These specific experiments used a pinhole aperture of 10 μm or a stepped pinhole with the large side being 50 μm and the smaller opening

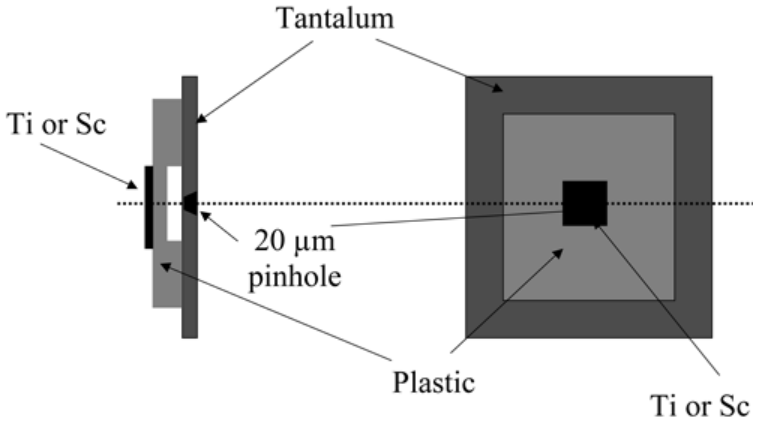

Figure A.1: Design of backlit pinhole target from the side and rear views. The pinhole in the Ta is stepped with a large opening of 50 μm and a smaller opening of 20 μm. Five hundred microns behind the pinhole is a 50 μm thick layer of plastic followed by a 500 μm square foil of Ti or Sc.

being 20 μm. The step refers to a large hole on one side of the Ta and a smaller hole on the other. Using a stepped structure (or a tapered pinhole), as opposed to a straight pinhole, produces x-rays having a larger cone angle and a more uniform intensity. This reduces the sensitivity of the pinhole backlighters to rotational alignment (though their alignment remains quite demanding). By comparison, the 10 μm straight pinhole allows for better resolution than the 20 μm stepped pinhole achieves, but any tilt in the foil will quickly decrease the source size, limiting the number of photons on the detector. A comparison of intensities from these two pinhole types is shown later in this appendix. Accomplishing backlit-pinhole radiography along two orthogonal lines of sight proved significantly more demanding than using only one line of sight. Using two backlighters is very difficult because any illumination from one will interfere with the other. This crosstalk effect is further complicated when using ungated film. In previous attempts, gated diagnostics were used and fired at different times during the experiment in an effort to prevent interference. However, in some cases, it has been noted that standard microchannel-plate framing cameras provided insufficient extinction of the ungated signals and so this approach generally failed. In order to

reduce the crosstalk, the present experiments protected each film holder with a nose cone. The narrow front end of the nose cone was located $\frac{1}{3}$ of the (228 mm) distance from the target to the film. At this front end a Ta shield having a 9 mm circular aperture was mounted, and magnetic material was included to deflect any electrons away from the film. With the 2 pinholes each displaced 12 mm from the target axis along orthogonal lines of sight, the 9 mm aperture was just sufficient to prevent the exposure of a portion of a given film pack by emission from the orthogonal backlighter. There was apparently some remaining exposure, presumably due to scattering of the x-rays, but this was small. With these techniques, it is possible to obtain data simultaneously along both lines of sight.

Figure A.2 shows the configuration of the experiment using this technique. The hydrodynamics target is placed so that the laser beams that deliver energy to it are focused at the center of the Omega chamber. The two backlit pinhole structures are placed 12 mm from the target and 90 degrees from each other. The placement of the film allows for a magnification of about 20 on the radiograph. During the experiment, 10 Omega laser beams irradiate the target, and the backlighters are irradiated after a delay of 7 – 40 ns. The group of beams irradiating the rear side of each pinhole structure consists of 2 – 4 Omega laser beams with a 1 ns pulse, 200 – 400 J beam^{-1}, and 1000 – 1200 μm spot size. The diagnostic x-rays pass through the target and onto the film, either DEF or other x-ray film. DEF is well characterized; by using the Henke model the optical density of the film can be converted to intensity in photons μm^{-2} [26]. In the film holder up to three pieces of film are layered on top of one another and behind Be, plastic and Ti or Sc light shields. The film is $\sim$ 50 mm in diameter and allows a field of view of about 1500 μm of the target.

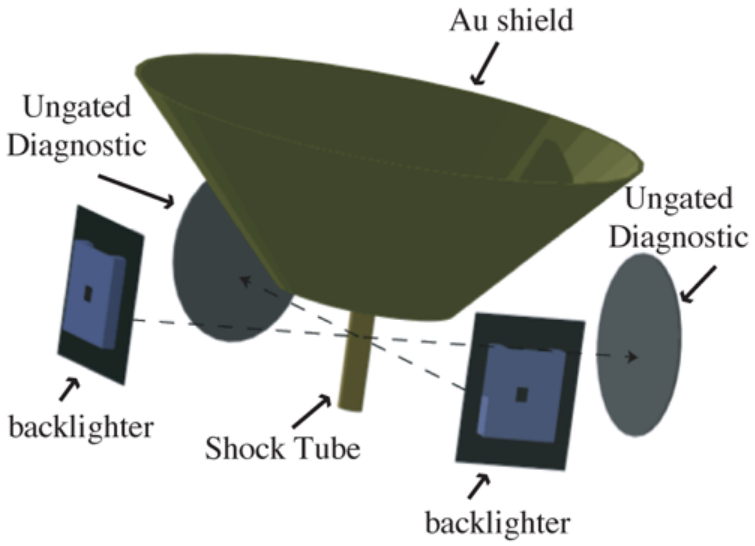

Figure A.2: Positions of the three targets and two diagnostics of experiment. The large, center target is the hydrodynamics target with the two backlighters perpendicular to the target and the other backlighter. There is an SPCA loaded with x-ray film on the opposite side of the target from each of the backlighters. The large gold cone on the main target shields the ungated diagnostics from the laser beams and hot plasma that is created during the experiment.

A.3 Results and Discussion

Figure A.3 shows radiographs from the experiment. These images, taken at 17 ns after the drive beams fired, are from the same laser shot. Figure A.3a is the first layer of film closest to the experiment itself and Figure A.3b is the layer that was directly behind it. Each image has a horizontal colorbar showing the intensity in units of photons μm^{-2}. In both images the dark area in the center of the image is the least-exposed region of interest, created by a long, rectangular, tracer strip of brominated plastic that is a comparatively strong absorber of x-rays. In Figure A.3a the spikes, long dense fingers moving to the right, and bubbles, less dense structures moving to the left, from the Rayleigh-Taylor [60, 70] instability are more clearly seen. The shock front is also seen at ~ 950 μm.

We evaluated the exposure and noise in the calibrated radiographic images as

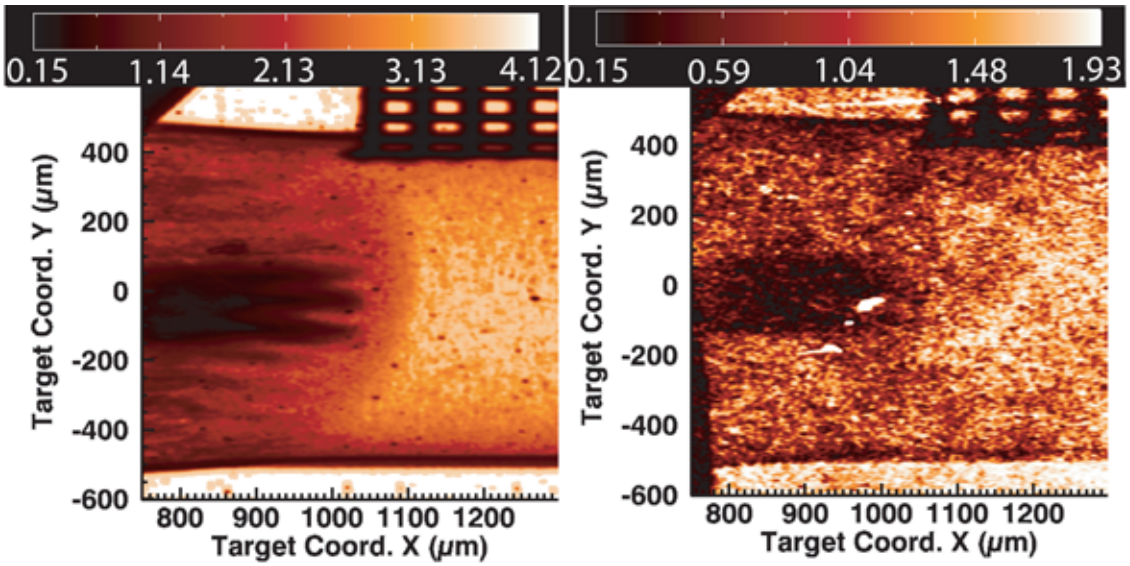

Figure A.3: Radiographic images from the experiment taken at 17 ns after the drive beams have fired. These radiographs are from the same experiment with a) being the top layer of DEF and b) being directly behind it. Each image has a colorbar associated with it that is in units of photons μm^{-2}

follows. Lineouts were taken across 1 pixel of the radiograph from a uniformly exposed area on the film. In this case, one pixel is equal to 22 μm on the film and the experiment had a magnification of 20, therefore, one pixel is 1.1 μm on the target. The mean and standard deviation were calculated from this lineout. The same process was done on an area where there should be no signal, in this case, behind the gold shield. The mean exposure there was considered to arise from either background noise or processing of the film. The number of photons μm^{-2} of interest was found by subtracting the intensity from noise signal from the intensity across a uniformly exposed area. From Figure A.3a the average number of photons μm^{-2} was 2.99 vs. 0.03 in Figure A.3b. Clearly, the 1st layer of film acts as a filter and fewer photons get to the second layer of film. This information is shown in Table A.1 along with anticipated and observed values of photon statistics. These values are also listed for several other experiments, including a comparison between a pinhole with an aperture of 50 μm stepped to 20 μm and a 10 μm straight pinhole.

Description	Mean	Expected $\frac{1}{\sqrt{N}}$	Observed $\frac{1}{\sqrt{N}}$
1^{st} layer of DEF	2.990	0.026	0.055
2^{nd} layer of DEF	0.033	0.250	0.212
20 μm stepped pinhole	1.082	0.044	0.029
10 μm straight pinhole	0.174	0.109	0.70

Table A.1: Estimated and observed values of the Poisson noise, $\frac{1}{\sqrt{N}}$, for four different experiments. Values for rows 1 and 2 are from 2 layers of DEF from the same experiment. Rows 3 and 4 were similar experiments except for difference pinhole apertures. N is the number of photons pixel^{-1}.

It is also of interest to estimate the expected number of photons pixel^{-1}. Using conclusions made by Kyrala (2003) the conversion efficiency of Ti is 5.66 $\times$ 10^{11} photons (J sphere)$^{-1}$ [43]. The laser beams striking the Ti foil have a total energy of 800 J and the area of the foil is 2.5 $\times$ 10^5 μm^2. If we estimate that only $\sim$ 50 % of these photons get transmitted through the foil and then pass through the pinhole with an area of 100π μm^2. The distance to the film is $\sim$ 230 mm and one pixel is equal to 484 μm^2 on the film, so there are 9.15 $\times$ 10^{-9} steradians pixel^{-1}. This gives about 200 photons pixel^{-1} or about 0.5 photons μm^{-2}, which does not take into account the plastic, Be, or Ti light filters. This is in good agreement with the values of Table A.1.

To calculate the values in Table A.1 let N be the number of photons pixel^{-1}. We find N by multiplying the average number of photons μm^{-2} by the area in one pixel, 484 μm^2. If Poisson noise were the only type of noise in this radiograph then the standard deviation divided by the signal would be $\frac{1}{\sqrt{N}}$. Table A.1 shows this value, and shows for comparison the observed noise obtained by dividing the standard deviation of the values obtained in the lineout described above by the mean, background-subtracted signal. The comparison of the expected and observed values is important because it determines whether the majority of noise on the radiograph is from Poisson noise or if there is a larger noise source in the experiment.

The anticipated and observed values agree within a factor of two and very closely

agree in some cases. It should be noted that the film used in these experiments had been stored over a long period and this increases the fog level of the film. As the fog level increases the film has a lower dynamic range. There is also an area of uncertainty in the difference among the film processing techniques used by Henke and the Laboratory for Laser Energetics. Other possibilities as to the difference between the theoretical and observed Poisson noise include saturation of the film if the actual Poisson noise is lower than the theoretical value. The 1st layer of film in Figure A.3a is presumably close to this point, although the observed noise is reasonably consistent with the expected Poisson noise. In this image, a lineout of an area outside the target is flat meaning the film is fully exposed. In this experiment the lasers striking the metal foil had an intensity of 6.4×10^{14} W cm^{-2}. Compare this to the last line in the table, which is the case of the 20 μm stepped pinhole that had a lower energy beam^{-1} as well as a larger spot size to decrease the intensity to 2.2×10^{14} W cm^{-2}. The experiment using a 10 μm straight pinhole also had an intensity of 2.2×10^{14} W cm^{-2}; however, the area of the pinhole was decreased by a factor of 4 making the radiograph dim. In all cases in Table A.1 the observed noise is within a factor of two of the Poisson noise, meaning that other sources of noise in the experiment, if present, are not dominant.

A.4 Conclusion

This appendix has discussed the design and geometry needed for dual, orthogonal backlit radiography. Results from these experiments show that only $< 1\%$ of the backlighter beam energy exposes the film and the Poisson noise is the dominant source of noise. In future experiments, the backlighter structure will have a Ta foil with 10 μm tapered pinholes. The taper is similar to the step, but has a smoother transition. These pinholes will have a large opening of ~ 20 μm tapered to 10 μm.

APPENDIX B

Assessing mix-layer amplitude in 3D Rayleigh-Taylor instability experiments

B.1 Introduction

This appendix describes the technique used to analyze data from HED laboratory experiments designed to explore the Rayleigh-Taylor [60, 70] instability under conditions relevant to supernovae. The Omega laser [7, 6] is used to create a blast wave structure that is similar to that of the explosion phase of a core-collapse supernova. An unstable interface is shocked and then decelerated by the planar blast wave, producing Rayleigh-Taylor growth. Recent experiments were performed using dual, side-on, x-ray radiography to observe a 3D "egg crate" mode and an imposed, longer-wavelength, sinusoidal mode as a seed perturbation. This appendix explores the method of data analysis and accurately estimating the position of important features in the data.

B.2 Discussion

Experimental radiographic images had been shown throughout this thesis and additional calibrated images are shown in Appendix F. As mentioned in Chapters II and III, determining the location of features in these radiographs is done using a lineout across the feature. A schematic of the target geometry is shown in Figure A.2. This experiment uses dual, orthogonal radiography. Two diagnostic views observe different dimensions of the tracer strip. One diagnostic view observes the length of the tracer strip and will be referred to as the "across the strip" view. The second diagnostic view, 90° from the first, observed the width or short side of the tracer strip. The second view will be referred to as the "down the strip" view. The view across the strip allows one to see about 13 spikes on the radiograph and the view down the strip allows one to see 3 or 4 spikes. An example of a view across the strip can be seen in Figures 4.1 on page 75 and Figure 4.3 on page 78. Likewise, an example of a view down the strip is seen in Figure A.3 on page 109. This image is looking down 3 or 4 rows of about 13 spikes each. Note that in Figure A.3 on either side of the high contrast tracer strip are fainter spikes. These are spikes of the polyimide material surrounding the tracer strip. While polyimide is nearly transparent to the He-α x-rays used in this experiment, these spikes are a result of seeing an entire row of polyimide spikes aligned to be seen as one. The positions of notable features are more clearly seen in the horizontal profiles or lineouts taken from radiographs similar to the examples listed above.

Figure B.1a shows horizontal lineouts from a radiograph of the across the strip view. Two lineouts were taken from this radiograph in order to estimate the position of the shock, spike tip and bubble tip. One lineout was taken across a Rayleigh-Taylor spike, shown by the red line, and the other across a bubble structure, shown by the black line. In Figure B.1a the shock, spike-tip and bubble-tip position are shown. The lineouts across the spike and bubble have a sharp decrease in intensity across

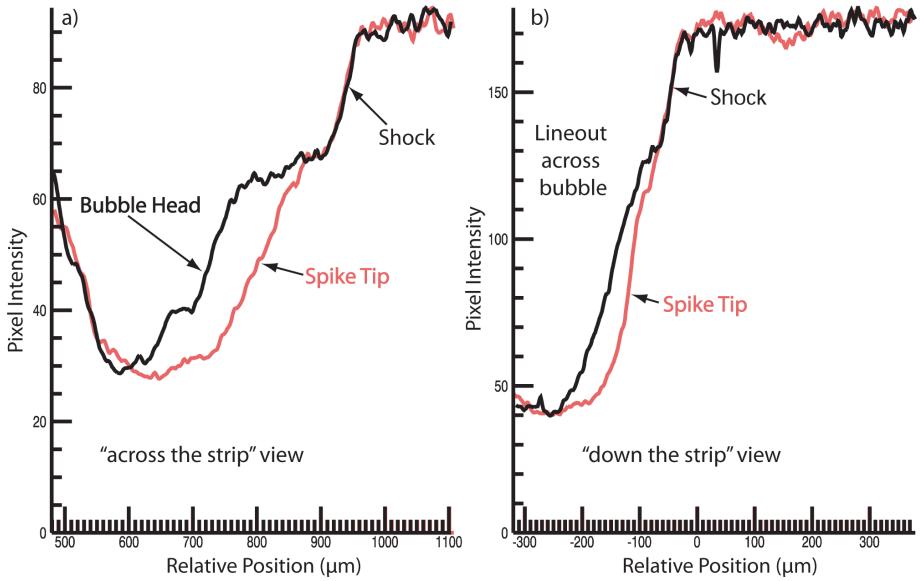

Figure B.1: Horizontal profiles across a spike and bubble from an experimental radiograph viewing a) the length of the tracer strip and b) the width of the tracer strip.

the shock. Moving to the right of the shock, the lineout across the spike then has a decrease in intensity at the tip of the spike. The lineout across the bubble also has a gradual decrease in intensity after the shock followed by an abrupt decrease and then a gradual increase in intensity from the remaining plastic layer. However, the bubble has a higher intensity than the spike since it appears lighter in the radiograph.

Figure B.1b shows lineouts across a spike and bubble from a radiograph of the down the strip view. Again the spike is in red and the bubble is in black. The sharp decrease across the shock and spike tip are clearly seen and similar to Figure B.1a. However, the bubble tip is difficult to discern in Figure B.1b. There is only a slight difference in the lineouts of the bubble and spike, making it almost impossible to locate the position of the bubble tip. For the same reason it is very difficult to see the location of the bubble tip within the tracer strip in Figure A.3. Looking through a row of 13 aligned spikes and bubbles causes a blurring of features in the radiograph. In contrast, the view across the tracer strip is only looking through 3 rows of aligned spikes and bubbles. Compare these lineouts to the lineout from a view across the

strip in Figure B.1a. Notice that the bubble position in the across the strip view is much more distinct than in the down the tracer strip view.

B.3 Conclusions

These experiments have been successful in obtaining dual-orthogonal x-ray radiographic data from targets well-scaled to the expected conditions at the He-H interface in the explosion phase of SN1987A. Dual, orthogonal radiography has allowed two views of the interface and the resulting growth of the mix layer from the Rayleigh-Taylor instability. Estimating this amplitude can be done by finding the positions of the spike tip and bubble tip. This appendix has shown that it is challenging to estimate the position of the bubble tip in the view down the strip because many spikes form a line blurring its position. However, the bubble-tip position can be found more easily and more accurately from the view across the tracer strip. The view down the strip is still very useful for confirming the spike-tip and shock position as well as diagnosing target abnormalities.

APPENDIX C

Image Processing of Radiographs in 3D Rayleigh-Taylor instability experiments

C.1 Introduction

The primary diagnostic data produced in the experiments is radiographic images, from which one desires to extract quantitative measures of instability development, such as the location of the RT bubble tips and spike tips as well as to calculate the mass of features produced by the RT instability. The present chapter is concerned with the analysis of data from a recent sequence of experiments, in which an improved diagnostic technique enabled us to obtain better diagnostic resolution, but introduced a challenging background feature into the experimental images. This background feature increases the difficultly in accurately locating and characterizing the features related to the RT instability. We describe and demonstrate here a method to remove enough of this background feature that improved analysis of the images is possible. We also illustrate a change in experimental technique that eliminates the background feature for future experiments, however, there is still a large amount of data that requires the image analysis technique described in this chapter.

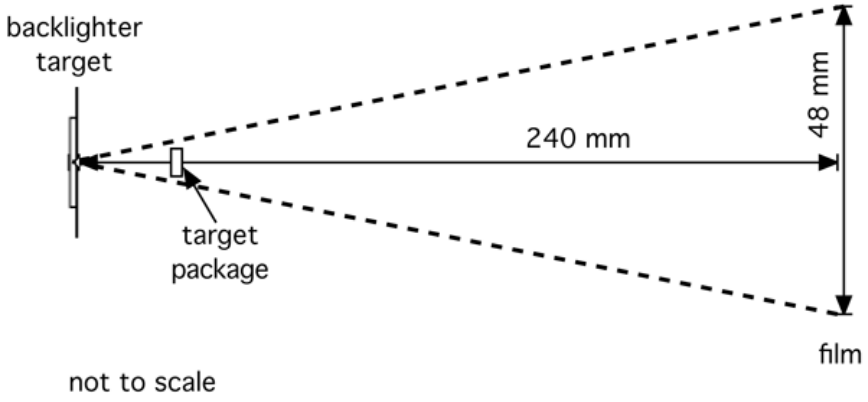

Figure C.1: A schematic of the backlighter, main target and diagnostic positions (not to scale) showing that, with the aperture specified above, there should be a uniform intensity from the x-rays over about $\sim 90\%$ of the film.

The primary diagnostic is side-on x-ray radiography, which is further detailed in Appendix A. The target shown in Figure A.1 on page 106 is a point projection pinhole backlighter used to create, in the images in this ppendix, 4.32 keV Sc He-α x-rays for the purpose of radiography. The x-rays from the backlighter pass through the target and are recorded on x-ray film loaded in an ungated SPCA. In the experiments described in this appendix, the SPCA was loaded with Agfa D7 x-ray film (DEF was also used in similar experiments). After the experiment, the film is digitized with a resolution of 22 μm per pixel on the film. The film is 240 mm from the backlighter target as shown in Figure C.1. From a geometric-optics perspective, this distance and the aperture of the pinhole should create a relatively flat intensity over an area of ~ 18 cm^2 and area of the entire film is ~ 20 cm^2. Thus, the intensity from the backlighter should be flat over roughly 90% of the film.

C.2 Discussion

Figure C.2a shows a radiographic image taken at 21 ns after the laser beams irradiated the target. This particular target had a 3D, 2-mode perturbation with an additional wavelength of 424 μm as the initial condition. In this image the interface

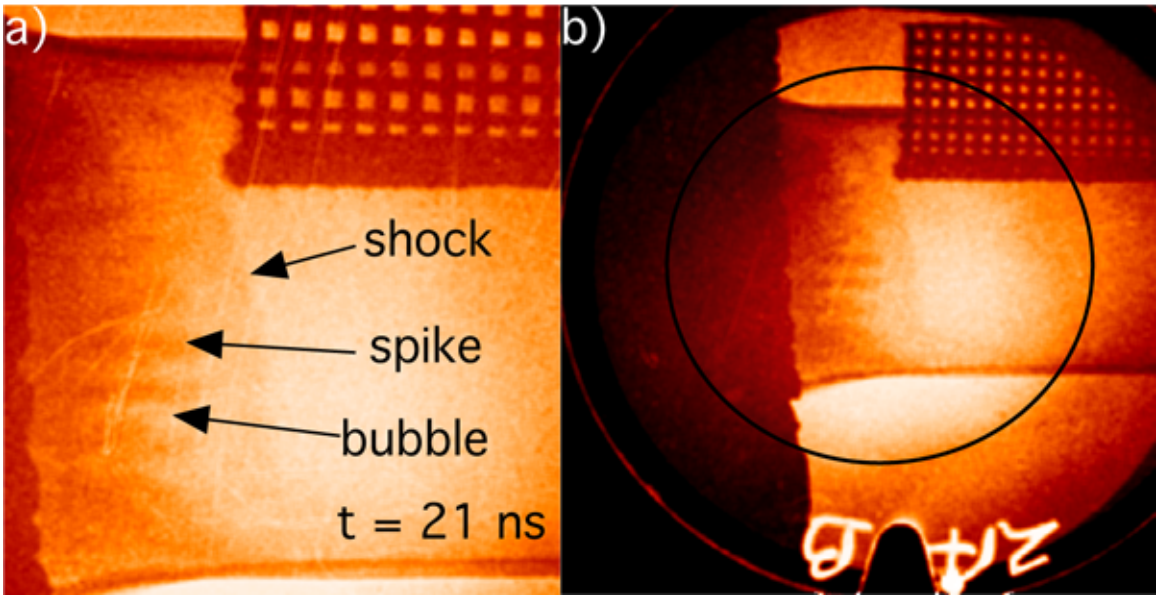

Figure C.2: (a) An x-ray radiograph of an experiment that had a 3D, 2-mode perturbation, where the additional mode had a wavelength of 424 μm. The shock wave and interface are moving to the right in this image. (b) This is the entire piece of film from this experiment. Note the circular spot that is roughly in the center of the image and indicated by the black circle.

and shock are moving to the right. The long, dark fingers are spikes due to the Rayleigh-Taylor instability. Bubbles of foam are in between the spikes of brominated plastic. The gold grid, with a wire period of 63 μm, can be seen in the upper right hand corner. The dark portion of the image on the far right is the edge of the gold-covered acrylic shield. The various thin, white streaks on the image are scratches on the film.

For this experimental series, several targets are imaged at different times after the initial laser pulse. The resulting radiographs are similar to the one seen in Figure C.2a. It is important to fully characterize the features described above in each image. Some examples of characterization are finding the location of the tip of the spike and the tip of the bubble as well as finding the amount of mass in a spike, bubble or the entire interface region. This information can be taken from several radiographic

images at several different times, which allows the study of the evolution of the RT instability.

Figure C.2b is an image of the entire piece of film, which is about 50.8 mm in diameter. An interesting feature in this image is the large spot, outlined by a dark circle, that is a little over 1 mm in diameter in the target plane and $\sim$ 20 mm on the film. This spot appears on all of our data images under similar conditions although its location, brightness and shape vary. Since the spot is circular it is thought that it is coming through the pinhole. The spot is apparently produced by very-high-energy photons or electrons, absorbed very weakly by the target, because it reduces the contrast of the observed structures in the image. The size of the pinhole and its position in relation to the experiment should provide a mostly flat illumination as discussed earlier in this chapter. One can look at the unshocked foam, where the intensity in the image should be relatively uniform to see that this is not the case in this image. A 1D profile from the unshocked region in the foam is shown in Figure C.3. This plot shows the relative pixel intensity vs. relative position in the unshocked foam. The fluctuations in the profile probably result from Poisson noise due to the limited number of x-ray photons. In similar, previous data we have shown this to be the primary source of noise as discussed in Appendix A.

This spot is of unknown origins and diminishes the contrast in the image. Eliminating the bright area from the image would greatly improve the image contrast and make the spike and bubble tips as well location of the shock front less obscured by the bright area on the radiographic image. Also, when calculating the mass of a spike, another way of analyzing this data, the background spot would lead to erroneous measures of mass. One possible way to remove much of the spot is to invert the image to k-space using a Fast Fourier Transform (FFT) and subtract the modes that are related to the spot in the image and then invert the image back to optical density space. These operations were performed using the Interactive Data Language (IDL).

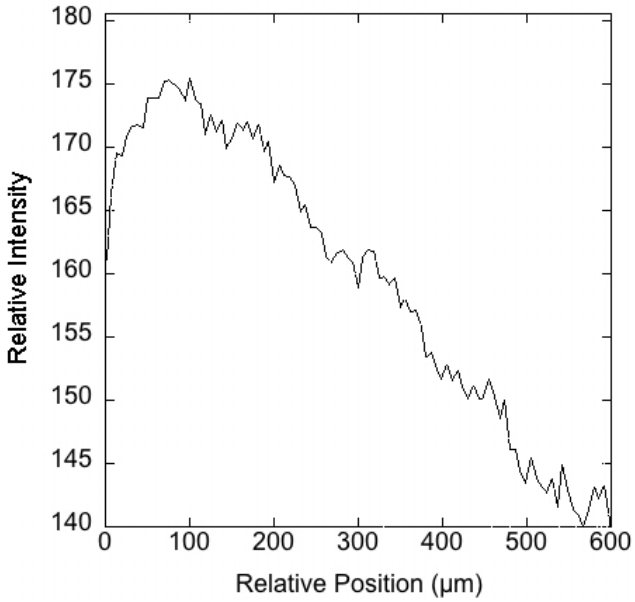

Figure C.3: A 1D profile through the unshocked foam region. This plot of relative pixel intensity vs. relative position should be uniform, but there is a prominent drop off due to the bright, circular emission on the film.

When an FFT is taken of a 2D array in IDL there are 4 elements in the power spectrum that corresponds to each 2D mode in the image, the real and imaginary parts of k_x and k_y. To remove the spot, one must identify the modes that correspond to it and subtract them in Fourier space.

The image shown in Figure C.2a contains numerous modes of varying amplitudes. The spot is roughly 1 mm in diameter in the target plane or covers about half of the image. As an approximation, assume this relates to a single low-order mode with a wavelength the entire length of the image. The four elements for that mode are then set to zero in the array of the power spectrum. Then the power spectrum is inverted to optical density space and then image should be of better quality. The image with the long-wavelength mode removed is shown in Figure C.4a and a magnified image of the film is seen in Figure C.4b. Even in this approximation the quality has improved from the initial image both in contrast and intensity uniformity. There is still a variation in the unshocked foam region, however, it is smaller and of less intensity than the original spot. This can be seen by the 1D profile taken from the image of

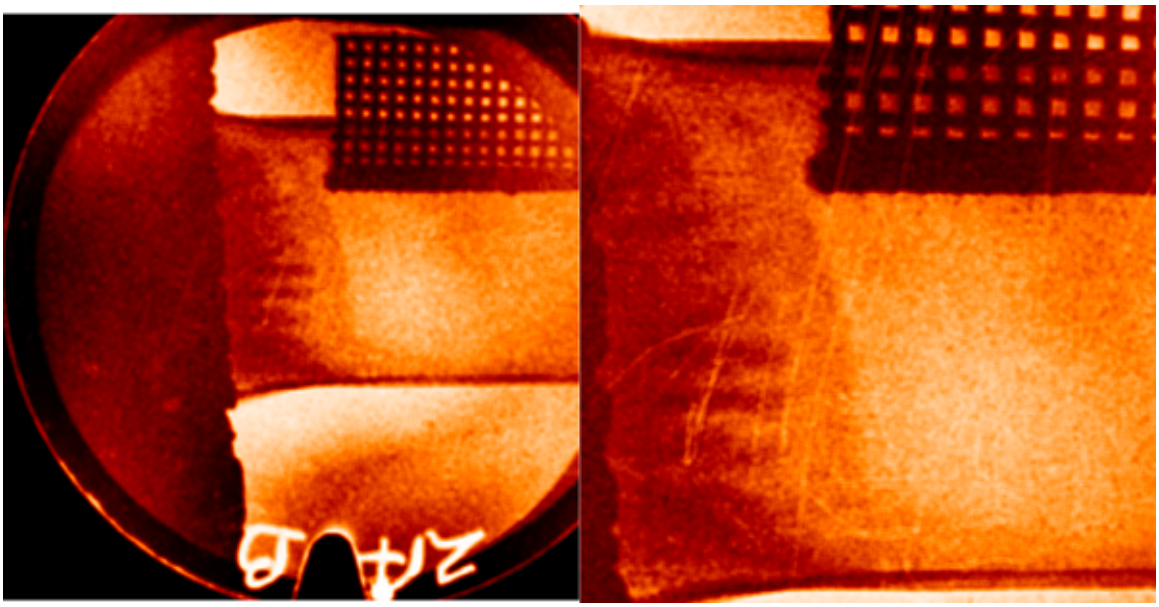

Figure C.4: (a) This is the x-ray radiograph shown in Figure C.2 with the bright spot mostly removed using the FFT method described here. (b) This expanded image shows that the bright area is greatly diminished.

Figure C.4b, shown in Figure C.5. Similar to Figure C.3, this plot is the relative pixel intensity vs. the relative position in unshocked foam. There also remains a variation outside of the shock tube, which can be seen in the image of the entire piece of film, Figure C.4a. The fact that the spot was not completely removed means that the spot is not entirely sinusoidal in nature. The majority of the spot can be modeled as a 2D sinusoid; however, when that is subtracted some smaller wavelength components of the spot still remain and can be seen on the image. Largely, the image with the long wavelength component of the bright feature removed is much improved.

Another way to remove the spot is to use the 1D profile in the unshocked foam from Figure C.3 in order to model the structure of the spot in the film. Then this modeled spot can be subtracted from the image. It is assumed that spot is circular and the 1D profile is essentially rotated 360° to create this model. The center of the spot is estimated by looking at the brightest area on the radiographic image as well as measuring the overall size of the spot and taking the midpoints. If the center of

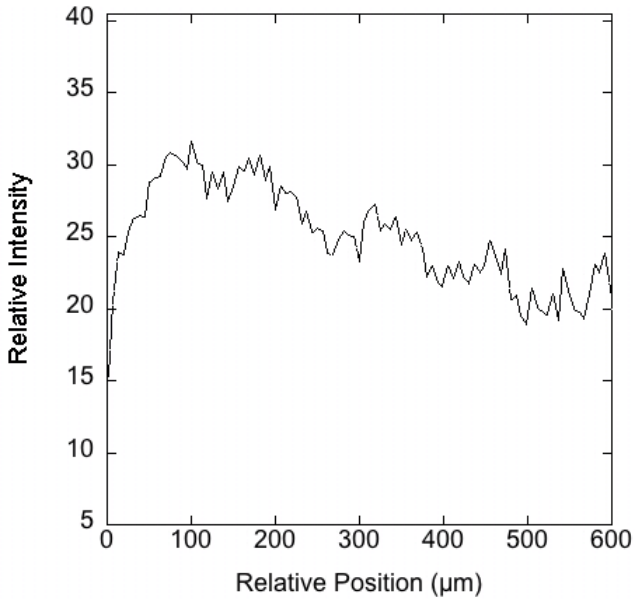

Figure C.5: A 1D profile through the unshocked foam region of an image with the spot removed by the FFT method shows a much flatter intensity than seen in Figure C.3.

the spot, which we are assuming to be the maximum intensity, lies outside of the unshocked foam region it is difficult to accurately model the spot. This is because there is variation in the shocked material due to the RT instability and one cannot ascertain how much of the pixel intensity is due to the background spot. However, this method captures the general size and variation in the background feature. The result from subtracting the modeled spot from the radiographic image is shown in Figure C.6a. As with the FFT method, the important features in the radiograph, the spike and bubble tips as well as the shock front, are clearer than in original radiograph. Also, a 1D profile in the unshocked foam section from the resulting image is shown in Figure C.6b. Again, this is relatively flat compared to Figure C.3.

It is important to compare the results of both methods as they can both be utilized for different purposes. Important features can be seen more clearly in Figure C.4b than in Figure C.6a. For this image it would be best to use the FFT method to find the location of the spike tip, bubble tip and shock front. Also, when the center of the background spot is located far from the unshocked foam region the spot subtraction

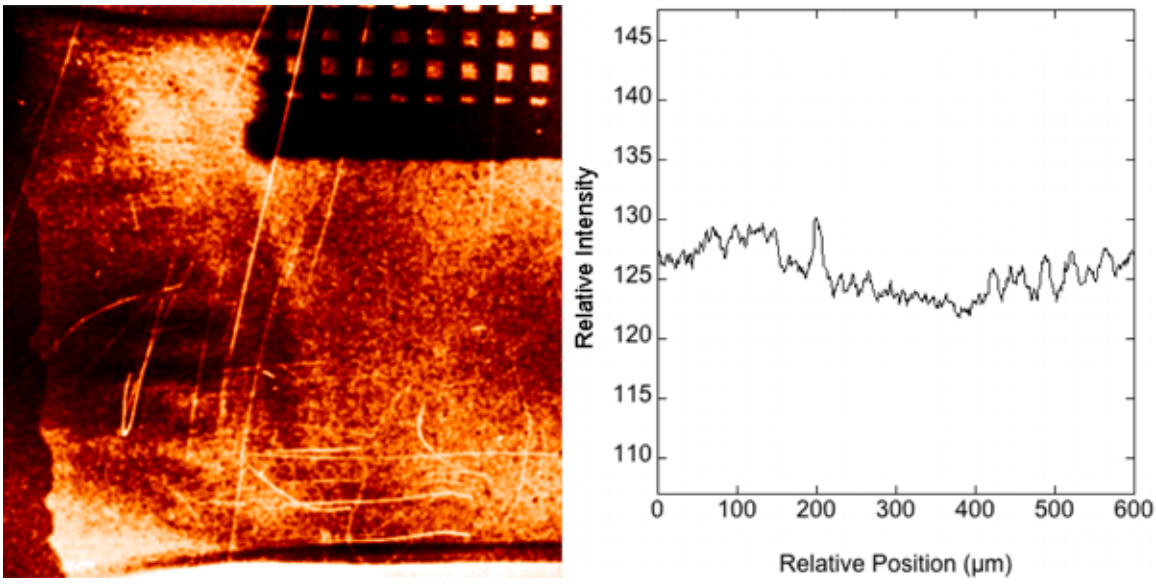

Figure C.6: (a) This is the x-ray radiograph similar to the one shown in Figure C.2a with the bright spot mostly removed using the spot modeling technique. (b) A 1D profile through the unshocked foam region of (a) shows a much flatter intensity that in Figure C.3.

method would become less accurate, as discussed previously, and it would also be best to use the FFT method. However, the spot subtraction method also proves to be more useful in certain cases. In observing the RT instability, it is of great interest to be able to study the flow of mass due to the instability. For instance, one can calculate the amount of mass in the spikes using method described by in Chapter IV. The method described uses the pixel intensity as one parameter in calculating the mass from a radiographic image. If an image had the background feature shown in this chapter the pixel intensity would not truly reflect the mass of that pixel. In this case, modeling the spot and subtracting it from the image would yield more accurate pixel intensities and therefore masses. Since the method of "removing" the mode includes setting the value of that mode to zero this method changes the pixel intensity as can be seen be comparing the 1D profiles in Figure C.2b and C.4b. Therefore, when calculating the amount of mass of a specific region in the image, the spot subtraction method is more precise.

As mentioned previously, the cause of this spot is unknown, although it plausibly may result from laser-plasma-interaction processes that can produce very energetic electrons. Accordingly, it was suggested that the spot would not appear if the beams irradiating the pinhole backlighter target came to the backlighter foil as a divergent beam, having passed through its focus, as opposed to a converging focus. (The diverging beam is more uniform than the converging one.) This hypothesis was tested on another experimental day using the same experimental setup except that the backlighter beams were diverging and the film was D8, another type of Agfa film instead of D7. The resulting image shown in Figure C.7a does not show a bright spot. A 1D profile of the relative intensity vs. relative position in the unshocked foam is shown in Figure C.7b. The profile is flatter overall. The use of D8 film rather than D7 cannot explain the disappearance of the spot, since D8 is more sensitive than D7. If the spot existed it would only appear brighter on D8. That same experimental day D7 film was used and it did not show a bright spot either, however, the overall quality of the film was poor due to low signal from our backlighter.

C.3 Conclusions

Recent experiments, motivated by supernovae hydrodynamics, have observed growth due to the RT instability from 3D multimode initial conditions. The quality of the resulting radiographic images is variable. This is due to a bright spot of unknown origin that appears on the film in some images, reducing the contrast of the data. However, the data can be made more suitable for quantitative analysis by taking the FFT of the image and removing the dominant modes that correspond to the global scale of the spot. An alternative method is to model the structure of the spot and subtract it from the image. Both of these methods improve quality of the radiographic image. Which method should be used depends on what type of further analysis will be implemented on the image pertaining to the RT instability. In limited tests, the spot

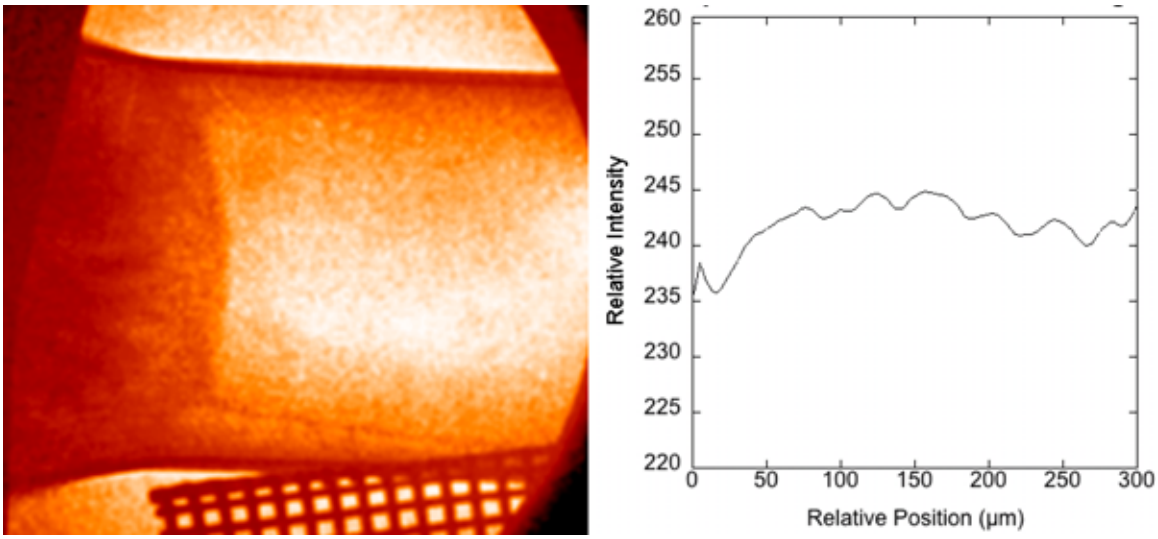

Figure C.7: (a) This x-ray radiograph was taken under conditions similar to the previous radiograph except that the beams that irradiated the backlighter target came to a diverging focus whereas in the Figure C.2 the backlighter beams came to a converging focus. (b) A 1D profile in the unshocked foam is more uniform than in Figure C.3 as is predicted by our backlighter geometry shown in Figure C.1.

has not appeared when the backlighter beams are diverging rather than converging. The data analysis approach discussed here will enable more accurate determination of the structure produced by the instabilities. The change in experimental technique should lead to improved data in future experiments.

APPENDIX D

Target Specifications

The specifications of the plastic/CHBr disks which are shown in Figure 3.1a have been optimized to give the best experimental results based on the capabilities of target fabrication. These disks are fabricated and characterized at General Atomics. The disk has a diameter of 915 $\pm$ 5 μm. This specification is based on the inner diameter of the polyimide tube, 912 μm. The outer diameter of 962 μm, makes the walls thin enough that x–rays used to diagnose the experiment have small attenuation. The tube is roughly the size of the laser spot, which is dictated by the phase plates used by Omega, corresponding to an 820 μm FWHM, and by their angle of incidence on the target (typically 45 degrees). The diameter of the polyimide/CHBr disk was chosen to be slightly larger than the polyimide tube so that it fit snugly into the tube once it has been inserted. The thin walls of the polyimide tube are malleable and are slightly distorted by the disk. The tolerance placed on the diameter specification is relatively tight at $\pm$ 5 μm, but this is to prevent the disk from slipping out of the tube if the disk is too small or potentially damaging or not fitting into the tube if the diameter is too large.

The width of the CHBr tracer strip is 230 $\pm$ 10 μm. In some targets the width is 250 $\pm$ 10 μm. The reason for this width is twofold. First, the main diagnostic view

observes the long dimension of the CHBr strip. Recall that the polyimide surrounding the strip is nearly transparent to the x–rays used to diagnose the experiment. It would be ideal to only observe the evolution of one row of spikes. However, it is not possible to reliably machine such a thin (71 μm) strip of material and such a narrow strip would have less than optimum x-ray absorption. In addition, it is useful for the orthogonal diagnostic view, discussed elsewhere [37, 38] to observe multiple wavelengths. With a strip width of 230 – 250 μm, approximately 3 spikes are visible.

Once the strip slot is milled, the CHBr material is glued in to the slot, the entire polyimide/CHBr surface is machined flat and then the specified pattern is machined. It is vital that the strip fit tightly into the slot, and that the remaining small space be filled with glue, otherwise, plasma could potentially squirt through the gap causing a jet–like flow of material. Components with glue–filled gaps of up to 4 μm were accepted. At this point, the informed reader might ask whether the squirting of material due to gaps is responsible for the spike extensions seen in the current experiment. Data from two, simultaneous, orthogonal diagnostic views showed that this is not the case. It was also important that a minimal amount of glue was between the base of the CHBr strip and the polyimide, as the larger shock speed would introduce structure in the shock front. Glue thicknesses up to 7 μm were accepted.

As discussed in Chapters III and IV, it is important that the surface depression of the CHBr strip be minimized. In previous experiments, a 5 μm depression caused the experimental results to be questioned, which led to rigorous specifications and characterization detailed here. A surface depression up to 0.3 μm is accepted. FLASH simulations showed that depressions larger than this had no measurable effect on the mix-layer amplitude [39]. The surface also had tool marks of characteristic spacing about 1 μm and amplitude about 0.6 μm.

The most carefully considered specifications are the disk thickness and polyimide web thickness. The web thickness is the thickness of the material below the CHBr

slot. The overall thickness is specified to be 142 +10/−5 μm. An additional 8 μm polyimide disk is attached to the polyimide side of the disk for a nominal total thickness of 150 μm. However, this gives an acceptable thickness range of 145 160 μm. The overall thickness of the plastic disk affects the speed of the shock when it reaches the interface. The thickness variation is $< 7\%$. The polyimide web thickness is 62 +10/−5 μm. When milling the slot out of the polyimide, it is important that the polyimide web is not too thin, as this would jeopardize the integrity of the piece. However, if the web is too thick the tracer strip will be too thin. It was discovered, during the course of this experiment, that a tracer strip of less than 40 μm was too thin to be properly diagnosed. Due to the order of the machining process the tracer strip thickness is solely determined by the overall disk thickness and the polyimide web thickness. With these tolerances, the tracer strip will range from 65 – 85 μm. This is well above the minimum threshold for tracer strip thickness.

These gaps and glue thicknesses, as well as, the measurement of other specifications, were determined by meticulous characterization by multiple instruments including a white light interferometer, a confocal scanning microscope and an optical microscope. This characterization is provided for each target component to ensure specifications detailed above are met for each experiment performed.

APPENDIX E

Experimental Specifications

The purpose of this appendix is to summarize the experimental setup at the Omega laser facility for experimental days that I was involved in and provided the majority of the data shown in this thesis. Table E.1 details the diagnostic used for each day, with the primary diagnostics is in bold. The specific setup for each individual diagnostic is also listed. The diagnostics are inserted into a Ten Inch Manipulator (TIM) and there are 6 TIMs at the Omega facility. The diagnostics in each TIM is listed as well as the fixed diagnostics in the Omega chamber that were used each of 3 experimental days. Some of the acronyms used in the following tables are, X-ray Framing Camera (XRFC), Laboratory for Laser Energetics (LLE), Lawrence Livermore National Laboratory (LLNL), backlighter (BL) and Magnetic Point Backlighter (MPBL). Table E.2 lists the laser conditions for each experimental day. in this table, SG1018, SG1017, SG1014 refer to the pulse shape of the laser beams. In all experiments the drive beams have a 1-ns square pulse shape.

Shot date	Primary Objective	TIM 1	TIM 2	TIM 3	TIM4	TIM5	TIM6	Fixed Diagnostic
30-Aug-05	Dual, Orthogonal Radiography	**Target Positioning System**	**SPCA 2, LLNL MPBL snout, 9mm pinhole, 8 mil Be blast shield, 20 mil Be rear filter, DEF, cranked frame P5.24, Y9.73 S9**	XRFC 3, 4 strip, LLE nosecone 6x-16 mag, 10 um pinhole, .004"Be, straight frame, .001" pinhole substrate, .001"Be rear filter	XRFC 4, 4 strip, LLE nosecone 6x-16 mag, 10 um pinhole, .004"Be, straight frame, .001" pinhole substrate, .001"Be rear filter	**Target Positioning System**	**SPCA 1, LLNL MPBL, 7mm pinhole, 8 mil Be +0.5milTi blast shield, 20 mil rear filter**	all pinhole and visible cameras
30-Nov-05	Dual, Orthogonal Radiography	**Target Positioning System**	**SPCA 2, LLNL MPBL snout, 9mm pinhole, 8 mil Be blast shield, 20 mil Be +.5mil Ti rear filter, DEF, cranked frame P5.24, Y9.73 S9**	XRFC 3, 4 strip, LLE nosecone 6x-16 mag, 10 um pinhole, .004"Be, straight frame, .001" pinhole substrate, .001"Be rear filter	XRFC 4, 4 strip LLE nosecone 6x-16 mag, 10 um pinhole, .004"Be, straight frame, .001" pinhole substrate, .001"Be rear filter	**Target Positioning System**	**SPCA 1, LLNL MPBL, 7mm pinhole, 8 mil Be +0.5mil Sc blast shield, 20 mil rear filter**	all pinhole and visible cameras
5-Dec-06	Dual, Orthogonal Radiography	**Target Positioning System**	empty	**SPCA 2, LLNL MPBL snout, 9mm pinhole, 8 mil Be blast shield, 20 mil Be +.5mil Ti rear filter, DEF/D7**	XRFC 3, 4 strip, LLE nosecone 6x-16 mag, 10 um pinhole, .004"Be, straight frame, .001" pinhole substrate, .001"Be rear filter	**Target Positioning System**	**SPCA 1, LLNL MPBL snout, 9mm pinhole, 8 mil Be blast shield, 20 mil Be +.5mil Ti rear filter, DEF/D7**	all pinhole and visible cameras

Table E.1: A summary of the experimental diagnostics used during a sample of the experimental days that I executed. These experiments provided the majority of the data in this thesis.

Shot date	Main driver pulse shape	BL driver pulse shaper	drive beams	drive energy	drive DPP	BL 1 beams	BL 2 beams	BL beam energy	BL beam spot
30-Aug-05	SG1018	SG1017	12, 14, 19, 21, 23, 25, 27, 29, 45, 50	450 J beam-1	SG8	31,33,35,37	38,63,64,60	300-400 J/beam	1000 μm
30-Nov-05	SG1018	SG1014	12, 14, 19, 21, 23, 25, 27, 29, 45, 50	450 J beam-1	SG8	31,33,35,37	38,63,64,60	200 J/beam	1200 μm
5-Dec-06	SG1018	SG1014	33,34,36,38,41,43,48,49,63,60	450 J beam-1	SG8	21,22,28,20	52, 55, 56, 58	425 J/beam	1000 μm

Table E.2: A list of the laser conditions used during a sample of the experimental days that I executed. These experiments provided the majority of the data in this thesis.

APPENDIX F

Radiographic data

The appendix shows data from 3 different experimental days and account for the majority of the data used in this thesis. The diagnostics and laser conditions for each experimental day are described in E. Each image is absolutely calibrated and enhanced to bring out pertinent features. The shot number of each image is located in the upper right corner. Each image is referenced by its shot number in Tables F.1, F.2, and F.3. These tables list the initial condition for each experimental image. "Single" refers to a single-mode perturbation and "2-mode, 212" or "2-mode, 424" refer to a 2-mode perturbation and a specific long-wavelength mode. "Planar" refers to targets with a flat interface. These tables also note the time the experiment was observed. The diagnostic view is also listed, where "across" refers to across the tracer strip and "down" refers to down the tracer strip. The diagnostic views are further discussed in Appendices A and B. If there is something specific to notes about the image a comment is added. Target coordinates are absolute unless noted.

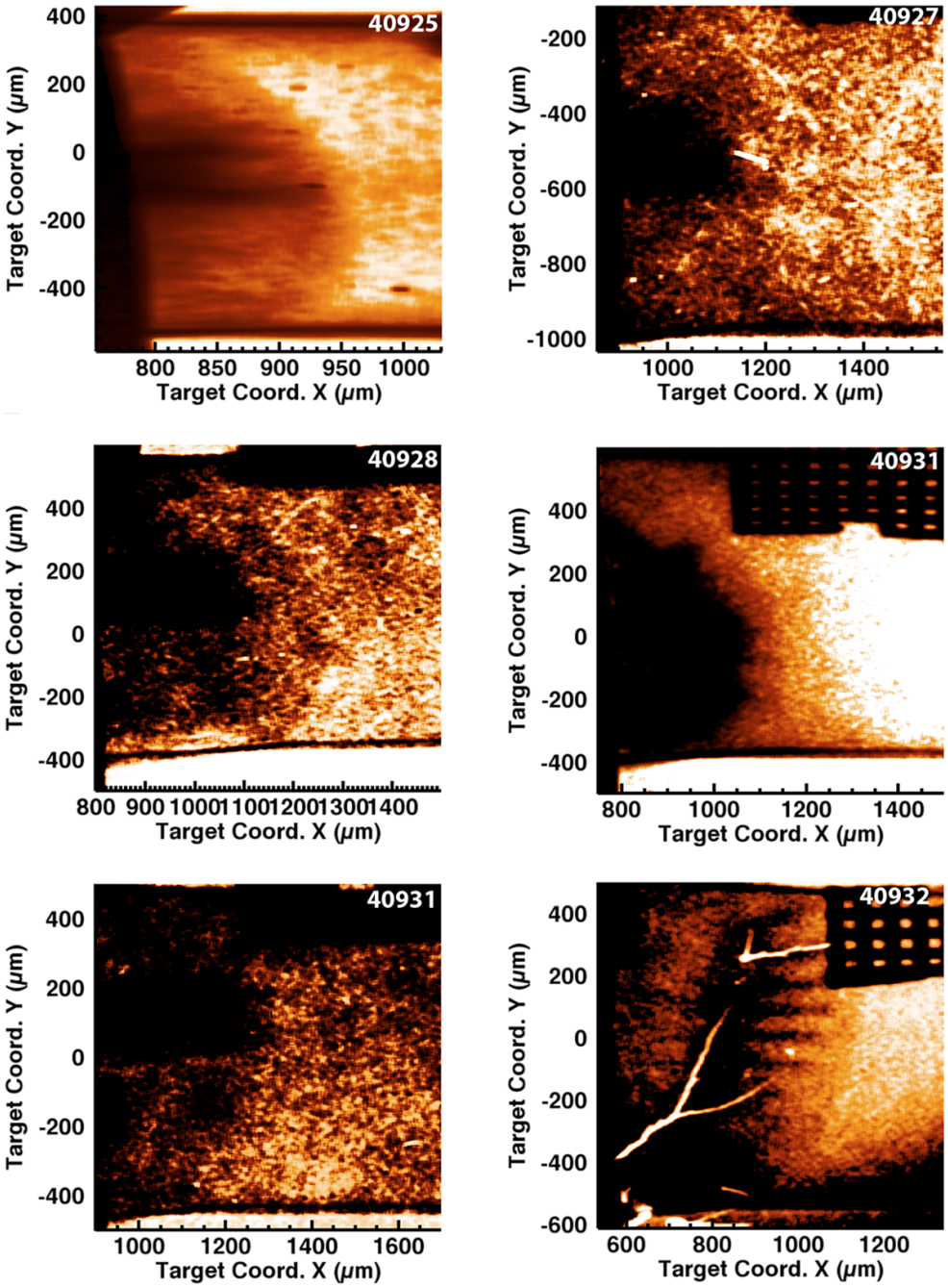

Figure F.1: Examples of data from the August 30, 2005 experimental day. The shot number is listed in the upper right corner of each image. More detail about each experiment can be found in Table F.1.

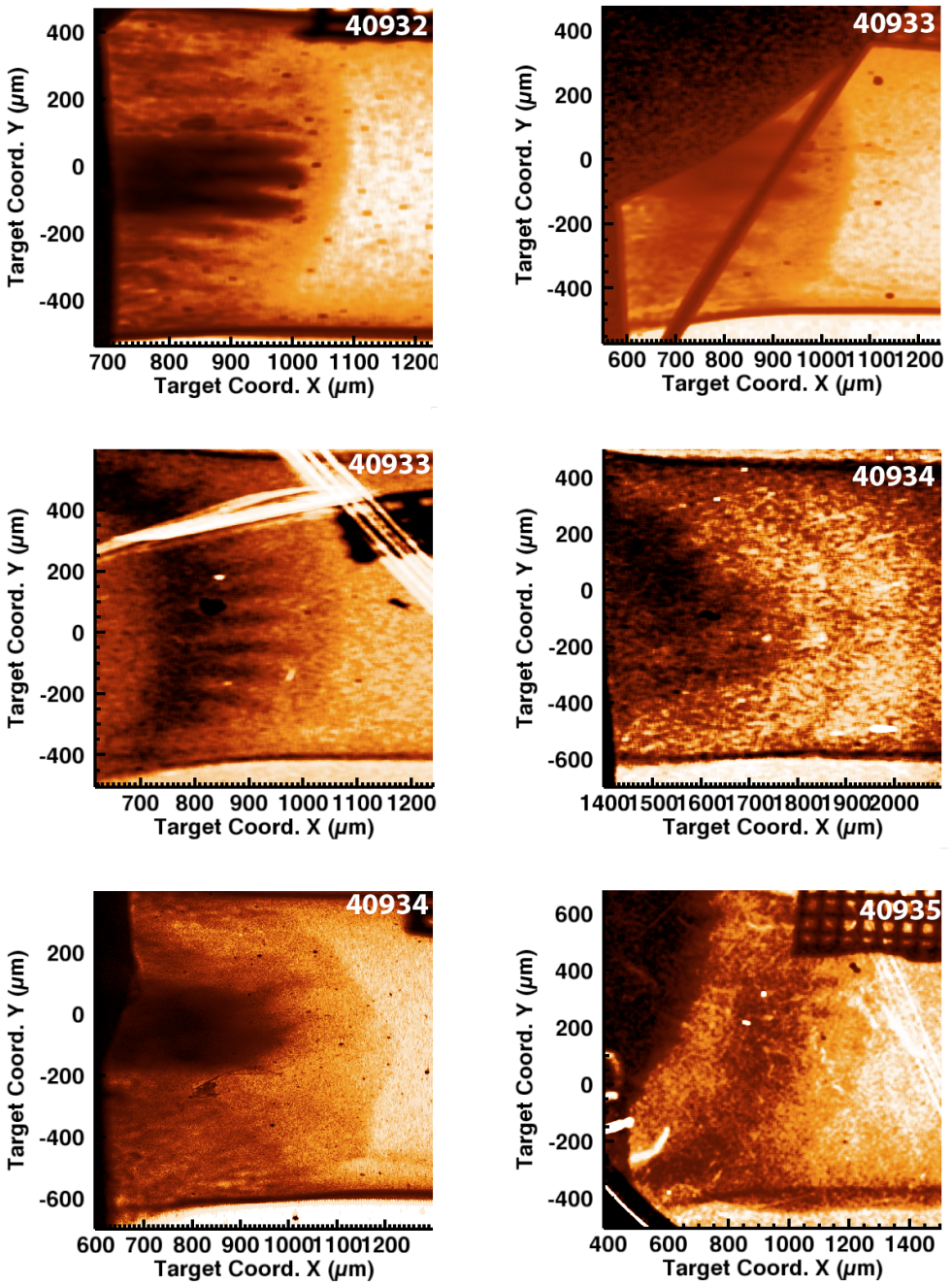

Figure F.2: Examples of data from the August 30, 2005 experimental day. The shot number is listed in the upper right corner of each image. More detail about each experiment can be found in Table F.1.

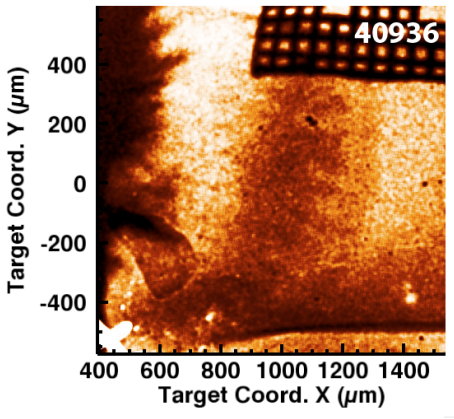

Figure F.3: Examples of data from the August 30, 2005 experimental day. The shot number is listed in the upper right corner of each image. More detail about each experiment can be found in Table F.1.

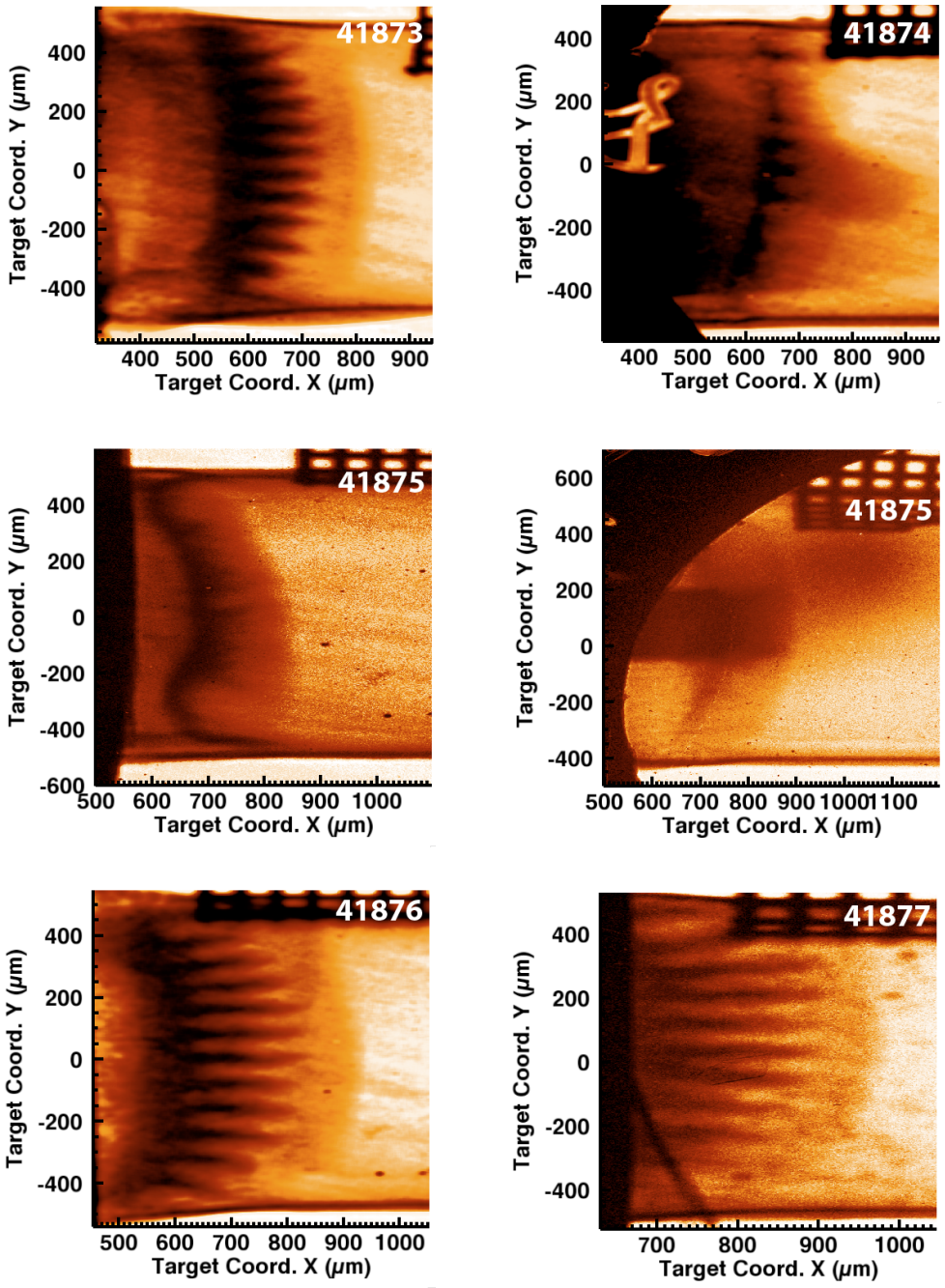

Figure F.4: Examples of data from the November 30, 2005 experimental day. The shot number is listed in the upper right corner of each image. More detail about each experiment can be found in Table F.2.

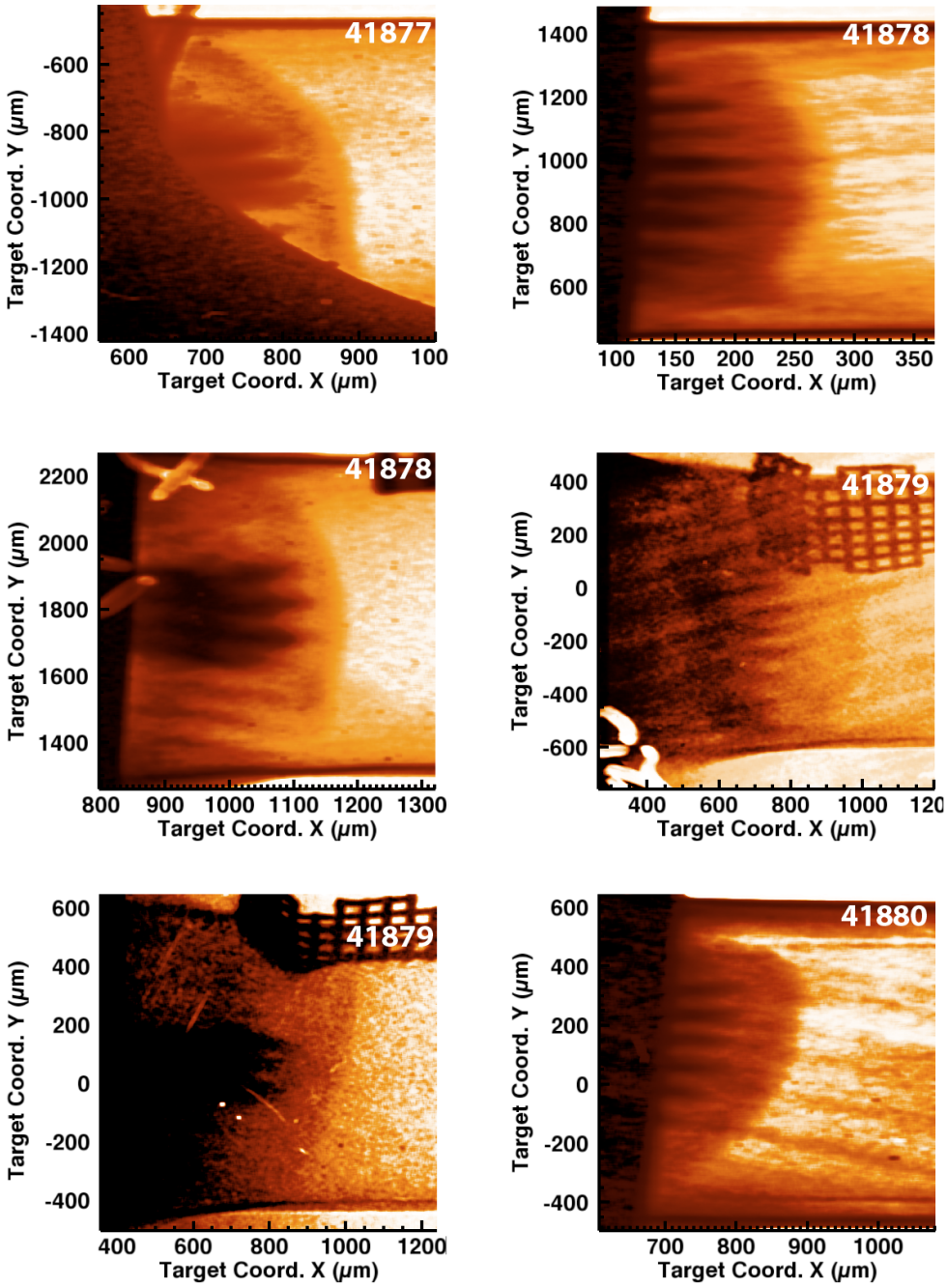

Figure F.5: Examples of data from the November 30, 2005 experimental day. The shot number is listed in the upper right corner of each image. More detail about each experiment can be found in Table F.2.

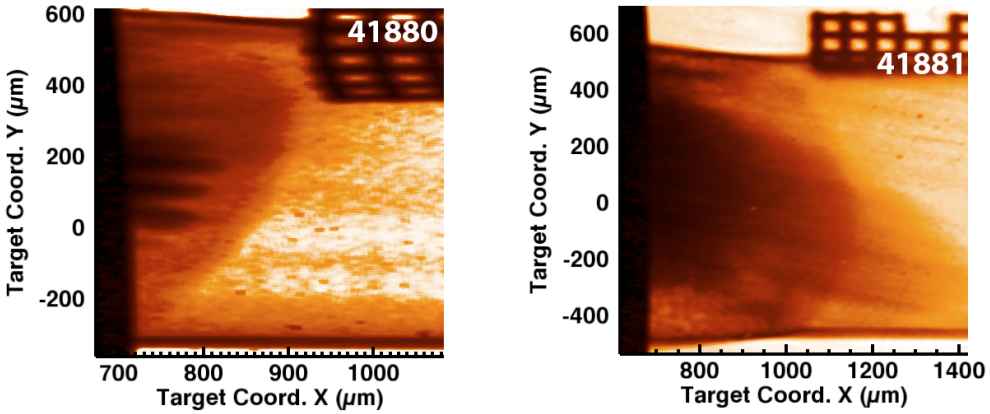

Figure F.6: Examples of data from the November 30, 2005 experimental day. The shot number is listed in the upper right corner of each image. More detail about each experiment can be found in Table F.2.

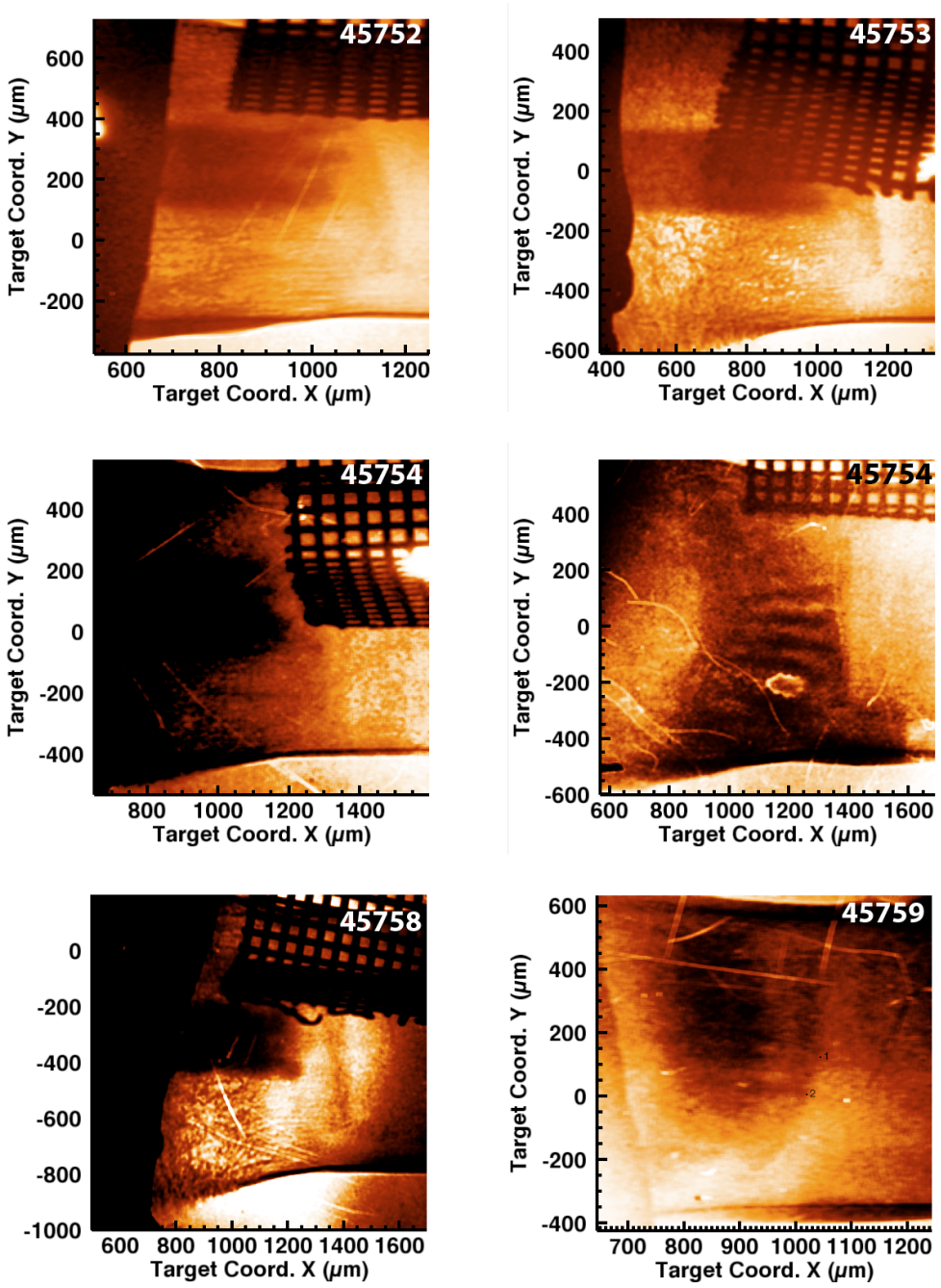

Figure F.7: Examples of data from the December 5, 2006 experimental day. The shot number is listed in the upper right corner of each image. More detail about each experiment can be found in Table F.3.

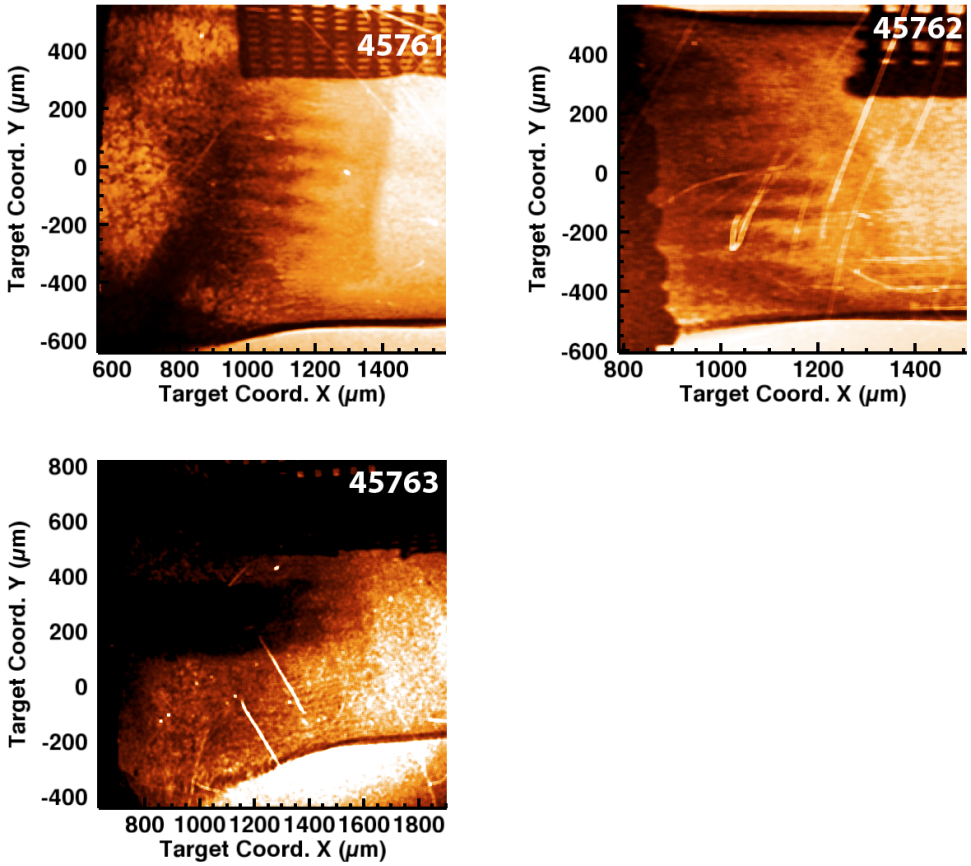

Figure F.8: Examples of data from the December 5, 2005 experimental day. The shot number is listed in the upper right corner of each image. More detail about each experiment can be found in Table F.3.

Shot number	Initial conditions	time (ns)	view	comment
40925	2-mode, 212	13	down	–
40927	single	17	down	possible target misalignment
40928	planar	17	down	–
40931	planar	17	across	–
40931	planar	17	down	–
40932	single	17	across	scratches on film visible
40932	single	17	down	–
40933	2-mode, 212	17	down	glass stalk and target wire visible
40933	2-mode, 212	17	across	scratched on film visible
40934	planar	21	across	–
40934	planar	21	down	–
40935	single-mode	21	across	target misaligned
40936	2-mode, 212	21	across	target misaligned

Table F.1: Description of images from August 2005 and seen in Figures F.1, F.2, and F.3.

Shot number	Initial conditions	time (ns)	view	comment
41873	2-mode, 424	13	across	striations on film due to filter
41874	single	17	across	thin CHBr tracer strip
41875	planar	13	across	striations on film due to filter
41875	planar	13	down	edge of nose cone visible
41876	2-mode, 424	17	across	striations on film due to filter
41877	2-mode, 212	17	across	spots in foam due to debris on filter
41877	2-mode, 212	17	down	relative coordinates
41878	single	17	across	relative coordinates
41878	single	17	down	relative coordinates
41879	2-mode, 424	17	across	striations on film due to filter
41879	2-mode, 424	17	down	–
41880	2-mode, 424	13	across	striations in foam due to filter
41880	2-mode, 424	13	down	–
41881	planar	17	across	anomalous target feature in foam

Table F.2: Description of images from November 2005 and seen in Figures F.4, F.5, and F.6.

Shot number	Initial conditions	time (ns)	view	comment
45752	2-mode, 212	21	down	–
45753	2-mode, 212	21	down	–
45754	single	21	down	–
45754	single	21	across	–
45758	planar	25	across	–
45759	single	13	down	target/strip misaligned
45761	2-mode, 424	25	across	–
45762	2-mode, 424	21	across	–
45763	2-mode, 212	21	down	–

Table F.3: Description of images from Decmber 2006 and seen in Figures F.7 and F.8.

BIBLIOGRAPHY

BIBLIOGRAPHY

[1] D. Arnett, B. Fryxell, and E. Muller. Instabilities and nonradial motion in SN 1987A. *ApJ Lett.*, 341(2):63–6, 1989.

[2] R.T. Barton. Development of a multimaterial two-dimensional, arbitrary lagrangian-eulerian mesh computer program. In J.M Centrella, J.M. LeBlanc, and R.L. Bowers, editors, *Numerical Astrophysics*, page 482. Jones and Bartlett, 1985.

[3] B. Biermann. Uber den ursprung der magnetfelder auf sternen und im interstellaren raum. *Zeitschrift Fur Naturforchung*, 5(65), 1950.

[4] BE Blue, HF Robey, SG Glendinning, MJ Bono, SC Burkhart, JR Celeste, RF Coker, RL Costa, SN Dixit, JM Foster, JF Hansen, CA Haynam, MR Hermann, JP Holder, WW Hsing, DH Kalantar, NE Lanier, DA Latray, H Louis, BJ MacGowan, GR Maggelssen, CD Marshall, EI Moses, AJ Nikitin, DW O'Brien, TS Perry, MW Poole, VV Rekow, PA Rosen, MB Schneider, PE Stry, BM Van Wonterghem, R Wallace, SV Weber, BH Wilde, DT Woods, and BK Young. Three-dimensional hydrodynamic experiments on the National Ignition Facility. *Physics of Plasmas*, 12(5), MAY 2005. 46th Annual Meeting of the Division of Plasma Physics of the American-Physical-Society, Savannah, GA, NOV 15-19, 2004.

[5] Blue, B.E., Hansen, J.F., Tobin, M.T., Eder, D.C., Robey, H.F. Debris mitigation in pinhole-aperatured point-projection backlit imaging. *Review of Scientific Instruments*, 75(11):4775–4777, 2004.

[6] T.R. Boehly, D.L. Brown, R.S. Craxton, R.L. Keck, J.P. Knauer, J.H. Kelly, T.J. Kessler, S.A. Kumpman, S.J. Loucks, S.A. Letzring, F.J. Marshall, R.L. McCrory, S.F.B. Morse, W. Seka, J.M. Soures, and C.P. Verdon. Initial performance results of the OMEGA laser system. *Optics-Communications*, 133:495–506, 1997.

[7] T.R. Boehly, R.S. Craxton, T.H. Hinterman, J.H. Kelly, T.J. Kessler, S.A. Kumpman, S.A. Letzring, R.L. McCrory, S.F.B. Morse, W. Seka, S. Skupsky, J.M. Soures, and C.P. Verdon. The upgrade to the OMEGA laser system. *Rev. Sci. Intsr.*, 66(1):508–510, 1995.

[8] K.S. Budil, T.S. Perry, P.M. Bell, J.D. Hares, P.L. Miller, T.A. Peyser, R. Wallace, H. Louis, and D.E. Smith. The flexible X-ray imager. *Rev. Sci. Inst.*, 67(2):485–8, 1996.

[9] A. Calder, B. Fryxell, T. Plewa, R. Rosner, L.J. Dursi, VG Weirs, T. Dupont, H.F. Robey, J.O. Kane, B.A. Remington, R.P. Drake, G. Dimonte, M. Zingale, F.X. Timmes, K. Olson, P. Ricker, P. MacNeice, and H.M. Tufo. On validating an astrophysical simulation code. *Astros. J. Suppl. Ser.*, 143(1):201–229, 2002.

[10] W.H. Calvin. The great climate flip-flop. *Atlantic Monthly*, 281:47–64, 1998.

[11] R.A. Chevalier. Supernova 1987A at five years of age. *Nature*, 355(6362):691–6, 1992.

[12] P. Colella and P.R. Woodward. The piecewise parabolic method (PPM) for gas-dynamical simulations . *J. Comp. Physics*, 54(1):174–201, 1984.

[13] G. Dimonte. Spanwise homogeneous buoyancy-drag model for Rayleigh-Taylor mixing and experimental evaluation. *Phys. Plasmas*, 7(6):2255–2269, 2000.

[14] F.W. Doss, R.P. Drake, H.F. Robey, and C.C. Kuranz. Wall Shock in High-Energy-Density Shock Tube Experiments. *Phys. Rev. Lett.*, submitted.

[15] R. P. Drake. *High-Energy-Density Physics: Fundamentals, Inertial Fusion, and Experimental Astrophysics*. Springer-Verlag, Berlin, 2006.

[16] R.P. Drake. Laboratory experiments to simulate the hydrodynamics of supernova remnants and supernovae. *J. Geophys. Res.*, 104(A7):14,505–14,515, 1999.

[17] R.P. Drake. Radiative Shocks in Astrophysics and the Laboratory. *Astrophysics and Space Science*, 2004.

[18] R.P. Drake, D.R. Leibrandt, E.C. Harding, C.C. Kuranz, M.A. Blackburn, H.F. Robey, B.A. Remington, M.J. Edwards, A.R. Miles, T.S. Perry, R. Wallace, H. Louis, J. Knauer, and D. Arnett. Nonlinear mixing behavior of the three-dimensional Rayleigh-Taylor instability at a decelerating interface. *Phys. Plasmas*, 11(5):2829–2837, 2004.

[19] R.P. Drake, H.F. Robey, O.A. Hurricane, Y. Zhang, B.A. Remington, J. Knauer, J. Glimm, D. Arnett, J.O. Kane, K.S. Budil, and J. Grove. Experiments to produce a hydrodynamically unstable, spherically diverging system of relevance to instabilities in supernovae. *Astrophys. J.*, 564:896–908, 2002.

[20] A.D. Edens, T. Ditmire, J. F. Hansen, M. J. Edwards, R.G. Adams, P. Rambo, I.C. Ruggles, I. Smith, and J. L. Porter. Study of high Mach number laser driven blast waves. *Phys. Plasmas*, 11:4968–4972., 2004.

[21] J.M. Foster, B.H. Wilde, P.A. Rosen, R.J. Williams, B.E. Blue, R.F. Coker, R.P. Drake, A. Frank, P.A. Keiter, A.M. Khokhlov, J.P. Knauer, and T.S. Perry. High-energy-density laboratory astrophysics studies of jets and bow shocks. *ApJL*, 634(1):L77–L80, 2005.

[22] B. Fryxell, E. Muller, and D. Arnett. Instabilities and Clumping in SN 1987A. I. Early Evolution in Two Dimensions. *Ap. J.*, 367:619–34, 1991.

[23] B. Fryxell, K. Olson, F. X. Timmes, M. Zingale, D. Q. Lamb, P. MacNeice, R. Rosner, J. W. Truran, and H. Tufo. Flash: An adaptive mesh hydrodynamics code for modeling astrophysical thermonuclear flashes. *ApJ Suppl. Ser*, 131(1):273–334, 2000.

[24] J. Grun, J. Stamper, C. Manka, J. Resnick, R. Burris, J. Crawford, and B.H. Ripin. Instability of Taylor-Sedov blast waves propagating through a uniform gas. *Phys. Rev. Lett.*, 66(21):2738–41, 1991.

[25] J. F. Hansen, H. F. Robey, R. I. Klein, and A. R. Miles. Experiment on the mass stripping of an interstellar cloud following shock passage. *ApJ*, 662:379–388, 2007.

[26] B.L. Henke, J.Y. Uejio, G.F. Stone, C.H. Dittmore, and F.G. Fujiwara. High-energy x-ray response of photographic films: models and measurement. *J. Opt. Soc. Am. B*, 3(11):1540–1550, 1986.

[27] M. J. Herbst, P.G. Burkhalter, J. Grun, R.R. Whitlock, and M. Fink. *Review of Scientific Instruments*, 53:1418, 1982.

[28] J. J. Hester, P. A. Scowen, R. Sankrit, C. J. Burrows, J. S. Gallagher III, J. A. Holtzman, A. Watson, J. T. Trauger, G. E. Ballester, S. Casertano, J. T. Clarke, D. Crisp, R. W. Evans, R. E. Griffiths, J. G. Hoessel, J. Krist, R. Lynds, J. Mould, E. J. O'Neil, K. R. Stapelfeldt, and J. A. Westphal. WFPC2 Studies of the Crab Nebula. III. Magnetic Rayleigh-Taylor Instabilities and the Origin of the Filaments. *Ap. J.*, 456:225–33, 1996.

[29] J. Kane, D. Arnett, B.A. Remington, S.G. Glendinning, G. Bazan, R.P. Drake, and B.A. Fryxell. Supernova experiments on the Nova laser. *Ap. J. Suppl.*, 127(2):365–369, 2000.

[30] J. Kane, D. Arnett, B.A. Remington, S.G. Glendinning, G. Bazan, R.P. Drake, B.A. Fryxell, R. Teyssier, and K. Moore. Scaling supernova hydrodynamics to the laboratory. *Physics of Plasmas*, 6(5):2065–2072, 1999.

[31] J. Kane, D. Arnett, B.A. Remington, S.G. Glendinning, J. Castor, R. Wallace, A. Rubenchik, and B.A. Fryxell. Supernova-relevant hydrodynamic instability experiments on the Nova laser. *Ap. J.*, 478(April 1):L75–L78, 1997.

[32] P.A. Keiter, R.P. Drake, T.S. Perry, H.F. Robey, B.A. Remington, C.A. Iglesias, R.J. Wallace, and J. Knauer. Observation of a hydrodynamically-driven, radiative-precursor shock. *Phys. Rev. Lett.*, 89:165003/1–4, 2002.

[33] K. Kifonidis, T. Plewa, H.T. Janka, and E. Muller. Non-spherical core collapse supernovae - I. Neutrino-driven convection, Rayleigh-Taylor instabilities, and the formation and propagation of metal clumps. *Astron. Astophys.*, 408(2):621, 2003.

[34] K. Kifonidis, T. Plewa, Scheck L., H.T. Janka, and E. Muller. Non-spherical core collapse supernovae - II. The late-time evolution of globaly anisotropic neutrino-driven explosions and their implications for SN1987A. *Astron. Astophys.*, 453(2):661, 2006.

[35] R.I. Klein, K.S. Budil, T.S. Perry, and D.R. Bach. Interaction of supernova remnants with interstellar clouds: from the Nova laser to the Galaxy. *Astrophys. J. Suppl. Series*, 127(2):379–383, 2000.

[36] R.I. Klein, C.F. McKee, and P. Colella. ON THE HYDRODYNAMIC INTERACTION OF SHOCK WAVES WITH INTERSTELLAR CLOUDS .1. NONRADIATIVE SHOCKS IN SMALL CLOUDS. *ApJ*, 420(1):213–236, 1994.

[37] C. C. Kuranz, B. E. Blue, R. P. Drake, H. F. Robey, J. F. Hansen, J. P. Knauer, M. J. Grosskopf, C. Krauland, and D. C. Marion. Dual, orthogonal backlit pinhole radiography in OMEGA experiments. *RSI*, (77):10E327, 2006.

[38] C. C. Kuranz, R. P. Drake, T.L. Donajowski, K.K. Dannenberg, M. J. Grosskopf, D. J. Kremer, C. Krauland, D. C. Marion, H. F. Robey, B. A. Remington, J. F. Hansen, B. E. Blue, J. Knauer, T. Plewa, and N. Hearn. Assessing mix-layer amplitude in 3D decelerating interface experiments. *Astrophys. and Space Sci.*, 307:115–119, 2007.

[39] C. C. Kuranz, R. P. Drake, M. J. Grosskopf, A. Budde, C. Krauland, D. C. Marion, A.J. Visco, J.R. Ditmar, H. F. Robey, B. A. Remington, A. R. Miles, A.B.R. Cooper, C. Sorce, T. Plewa, N. C. Hearn, K.L. Killibrew, J. P. Knauer, and D. Arnett. 3D blast-wave-driven Rayleigh-Taylor instability and effects of long-wavelength modes. *Phys. Plasmas*, 16(056310), 2009.

[40] C. C. Kuranz, R. P. Drake, M. J. Grosskopf, B. Fryxell, A. Budde, A. R. Miles, J. Knauer, T. Plewa, and N. Hearn. Spike morphology in Rayleigh-Taylor, decelerating interface experiments. *Phys. Plasmas*, submitted.

[41] C. C. Kuranz, R. P. Drake, M. J. Grosskopf, H. F. Robey, B. A. Remington, J. F. Hansen, B. E. Blue, and J. Knauer. Image Processing of Radiographs in 3D Rayleigh-Taylor Decelerating Interface Experiments. *Astrophys. and Space Sci.*, accepted for publication.

[42] C. C. Kuranz, R. P. Drake, E. C. Harding, M. J. Grosskopf, H. F. Robey, B. A. Remington, M. J. Edwards, A. R. Miles, T. S. Perry, T. Plewa, N. C. Hearn, J. P. Knauer, D. Arnett, and D. R. Leibrandt. 2D Blast-wave-driven Rayleigh-Taylor instability: experiment and simulation. *ApJ*, 696(1):749–759, 2009.

[43] G.A. Kyrala, K. Klare, and J. Workman. Optimizing area-backlighter performance indifficult geometry. *Review of Scientific Instruments*, 74(3):2182–2185, 2003.

[44] N.E. Lanier, J.S. Cowan, and J. Workman. Characterization and cross calibration of Agfa D4, D7, and D8 and Kodak SR45 x-ray films against direct exposre film at 4.0 - 5.5 keV. *Rev. Sci. Instrum.*, 77(043504), 2006.

[45] J.T. Larsen and S.M. Lane. HYADES: a plasma hydrodynamics code for dense plasma studies. *J. Quant. Spectrosc. Radiat. Transfer*, 51(1):179–186, 1994.

[46] McGLinchey J. Lewis, C.L.S. QUASI-MONOCHROMATIC, PROJECTION RADIOGRAPHY OF DENSE LASER DRIVEN SPHERICAL TARGETS. *Optics Communications*, 53(3):179–186, 1985.

[47] C.K. Li, F.H. Segiun, J.A. Frenje, J.R. Rygg, R.D. Petrasso, R.P.J. Town, P.A. Amendt, S.P. Hatchett, O.L. Landen, A.J. Mackinnon, P.K. Patel, V.A. Smalyuk, T.C. Sangster, and J.P. Knauer. Measuring E and B Fields in Laser-Produced Plasmas with Monoenergetic Proton Radiography. *Phys. Rev. Lett.*, 97(135003), 2006.

[48] J.D. Lindl. *Inertial Confinement Fusion*. Springer Verlag, New York, 1998.

[49] P.J. McGregor, P.D. Nichloson, and M.G. Allen. *Icarus*, 121(361), 1996.

[50] E.E. Meshkov. *Soviet Fluid Dyn.*, 4:101, 1969.

[51] A.R. Miles. The blast-wave-driven instability as a vehicle for understanding supernova explosion structure. *Ap. J*, 696(1):498–514, 2009.

[52] A.R. Miles, D.G. Braun, M.J. Edwards, H.F. Robey, R.P. Drake, and D.R. Leibrandt. Numerical simulation of supernova-relevant laser-driven hydrodynamics experiments on Omega. *Phys. Plasmas*, 11(7):3631–3645, 2004.

[53] A.R. Miles, M.J. Edwards, and H.F. Robey. The effect of a short-wavelength mode on the nonlinear evolution of a long-wavelength perturbation driven by a strong blast wave. In *Inertial Fusion and Science Applications*, page submitted, Monterey, CA, 2003.

[54] E. Muller, B. Fryxell, and D. Arnett. Instabilities and Clumping in SN 1987A. *Astron. Astophys.*, 251:505–514, 1991.

[55] K. Olson and P. MacNeice. The overview of the PARAMESH AMR software package and some of its applications. *Lecture Notes in Computational Science and Engineering*, 41(315-330), 2005.

[56] D. Oneill, C.L.S. Lewis, D. Neely, S.J. Davidson, S.J. Rose, and R.W. Lee. Characterization of a laser-produced plasma using the technique of point-projection absorption-spectroscopy. *Phys. Rev. A.*, 44(4):2641–2648, 1991.

[57] D. Oron, L. Arazi, D. Kartoon, A. Rikanati, U. Alon, and D. Shvarts. Dimensionality dependence of the Rayleigh-Taylor and Richtmyer-Meshkov instability late-time scaling laws. *Phys. Plasmas*, 8(6):2883–2890, 2001.

[58] Shih-i Pai. *Radiation Gas Dynamics*. Springer-Verlag, 1966.

[59] P.K. Rambo, I.C. Smith, J. L. Porter, M.J. Hurst, C.S. Speas, R.G. Adams, A.J. Garcia, E. Dawson, B.D. Thurston, Wakefield C., J.W. Kellogg, M.J. Slattery, H.C. Ives, R.S. Broyles, J. A. Caird, A.C. Erlandson, J.E. Murray, W.C. Behrendt, N.D. Neilsen, and J.M. Narduzzi. Z-beamlet: a multikilojoule, terawatt-class laser system. *Appl. Optics*, (2421-2430), 44.

[60] Lord Rayleigh. *Scientific Papers II*. Cambridge, Cambridge, England, 1900.

[61] A.B. Reighard, R. P. Drake, K.K. Danneberg, D. J. Kremer, T.S. Perry, B.A. Remington, R.J. Wallace, D.D. Ryutov, J. Greenough, J. Knauer, T. Boehly, S. Bouquet, A. Calder, R. Rosner, B. Fryxell, D. Arnett, M. Koenig, and N. Grandjouan. Collapsing Radiative Shocks in Xenon Gas on the Omega Laser. In *Inertial Fusion and Science Applications*, page in press, Monterey CA, 2003.

[62] A.B. Reighard, R.P. Drake, K.K. Dannenberg, J.Knauer, and L. Boireau S. Bouquet. Observation of Collapsing Radiative Shock in Laboratory Experiments. *Phys. Plasmas*, in submission, 2006.

[63] B. A. Remington, R. P. Drake, and D. D. Ryutov. Experimental astrophysics with high power lasers and Z pinches. *Rev. Mod. Phys.*, 78(3):755–807, 2006.

[64] B.A. Remington, J. Kane, R.P. Drake, S.G. Glendinning, K. Estabrook, R. London, J. Castor, R.J. Wallace, L.J. Suter, D.H. Muntro, D. Arnett, E. Liang, R. McCray, A. Rubenchik, and B. Fryxell. Supernova hydrodynamics experiments on the Nova laser. *Phys. Plasmas*, 4(5):1994–2003, 1997.

[65] D.H. Richtmyer. *Commun. Pure. Appl. Math*, 13:297, 1960.

[66] H.F. Robey, J.O. Kane, B.A. Remington, R.P. Drake, O.A. Hurricane, H. Louis, R.J. Wallace, J. Knauer, P. Keiter, D. Arnett, and D.D. Ryutov. An experimental testbed for the study of hydrodynamic issues in supernovae. *Phys. Plasmas*, 8(May):2446–2453, 2001.

[67] H.F. Robey, Ye Zhou, A.C. Buckingham, P. Keiter, B.A. Remington, and R.P. Drake. The onset of turbulence in high Reynolds number, accelerated flows. Part II. Experiment. *Phys. Plasmas*, 10:614, 2003.

[68] J.R. Rygg, F.H. Segiun, C.K. Li, A. Frenje, M.J.-E. Manuel, R.D. Petrasso, R. Betti, J.A. Delettrez, O.V. Gotcheck, J.P. Knauer, D.D. Meyerhofer, F.J. Marshall, C. Stoeckl, and W. Theobald. Proton Radiography of Inertial Fusion Implosions. *Science*, 319, 2008.

[69] D.D. Ryutov, R.P. Drake, J. Kane, E. Liang, B.A. Remington, and M. Wood-Vasey. Similarity Criteria for the Laboratory Simulation of Supernova Hydrodynamics. *Ap. J.*, 518(2):821, 1999.

[70] Sir Geoffrey Taylor. Hydrodynamic Instabilities. *Proc. R. Soc.*, A201:192, 1950.

[71] E.T. Vishniac. The dynamic and gravitational instabilities of spherical shocks. *Ap. J.*, 274(1 Nov.):152–67, 1983.

[72] S.E. Woosley. Supernova 1987A: after the peak. *ApJ*, 330(1):218–253, 1988.

[73] S.E. Woosley, P.A. Pinto, and L. Ensman. Supernova 1987A: six weeks later. *ApJ*, 324(1):466–89, 1988.

[74] J. Workman, J.R. Fincke, P. Keiter, G.A. Kyrala, T. Pierce, S. Sublett, J.P. Knauer, H. Robey, B. Blue, S.G. Glendinning, and O.L. Landen. Development of intense point x-ray sources of backlighting high energy density experiments. *Review of Scientific Instruments*, 75(10):3915–3920, 2004.

[75] J.R. Kyrala G.A. Pierce T. Workman, J. Fincke. Uniform large-area x-ray imaging at 9 keV using a backlit pinhole. *Applied Optics*, 44(6):859–865, 2005.

[76] Y.B. Zeldovich and Y.P. Raizer. *Physics of Shock Waves and High-Temperature Phenomena*. Academic Press, 1966.

[77] Ye Zhou, B.A. Remington, H. F. Robey, A.W. Cook, S.G. Glendinning, A. Dimits, A.C. Buckingham, G.B. Zimmerman, E. W. Burke, T.A. Peyser, W.H. Cabot, and D. Eliason. Progress in understanding turbulent mixing induced by Rayleigh-Taylor and Ricktmyer-Meshkov instablities. *Phys. Plasmas*, 10(5):1883, 2003.